MnDOT Contract, No. 1003325, Work Order No. 56

NRRA Long-term Research Project

Performance Benefits of Fiber-reinforced Thin Concrete Pavement and Overlays

Task-2: Second Year Annual Cell Performance Report (2018-2019)

Prepared by:
Manik Barman, Corey Crick, Amarjeet Tiwari, Souvik Roy, UMD
and
Tom Burnham, Minnesota Department of Transportation

UMD
UNIVERSITY OF MINNESOTA DULUTH
Driven to Discover

DEPARTMENT OF TRANSPORTATION

2020

DISCLAIMER

This report represents the results of research conducted by the authors and does not necessarily represent the views or policies of the National Road Research Alliance, Local Road Research Board, Transportation Research and Innovation Group of the Minnesota Department of Transportation, or the University of Minnesota Duluth. This report does not contain a standard or specified technique.

The authors, The National Road Research Alliance, the Local Road Research Board, the Minnesota Department of Transportation, Transportation Research and Innovation Group and the University of Minnesota Duluth do not endorse products or manufacturers. Any trade or manufacturers' names that may appear herein do so solely because they are considered essential to this report.

LIST OF CONTENTS

LIST OF TABLES

LIST OF FIGURES

1 INTRODUCTION

The Minnesota Department of Transportation (MnDOT) constructed several fiber reinforced concrete (FRC) test cells at MnROAD in 2017. These cells were constructed as a part of a National Road Research Alliance (NRRA) funded research study on fiber reinforced concrete. The main research objective of these cells is to identify and quantify the contribution of structural fibers in mitigating different distresses that typically occur in thin concrete pavements and overlays. The location of the 2017 FRC research cells at the MnROAD test facility is shown in Figure 1-1. Table 1 presents a summary of the designs and materials used in these test cells. A total of eight cells were constructed, among which seven cells were constructed with FRC, and one control cell was constructed with plain concrete (Cell 506). Cells 139 and 239 were constructed as ultra-thin (3-inch) and thin (4-inch) concrete pavement on unstabilized gravel base (matching with typical city street design). An enhanced fiber dosage (@30% RSR; see Table 1 for the dosage information) was used in these two cells. Cells 705 and 805 were constructed as thin unbonded concrete overlays on an existing concrete pavement varying the panel size; a standard fiber dosage (@20% RSR) was used in these two cells. Cells 506 through 806 were constructed as thin concrete pavement on unstabilized gravel base mainly varying with fiber content (0% to 0.75% volume fraction).

Table 2 presents the paving dates of the different cells. Figure 1-2 shows a photograph of the fiber used in all the seven FRC cells during the 2017 construction. Table 3 presents the mix design for the FRC research cells. All the eight cells were equipped with different types of sensors for measuring responses such as (i) dynamic strain due to wheel load, (ii) static strain induced by the environmental forces, (iii) pavement temperature and gradient, and (iv) joint movement. Periodical distress (cracks, spalling, and faulting) surveys were conducted to keep track of the distresses. Falling weight deflectometer (FWD) tests are periodically conducted to determine joint performance in different seasons. This report provides a summary of the distresses observed in the abovementioned 2017 FRC research cells and an analysis and discussion of the responses measured by different sensors up through the second year of service.

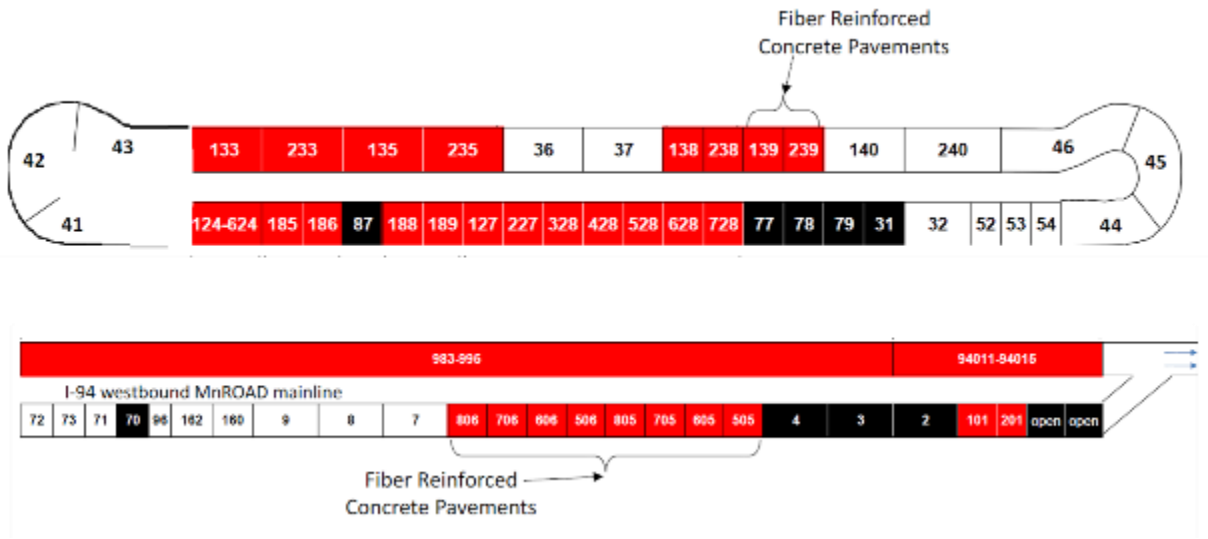

Figure 1-1: Location of the 2017 FRC Research cells at the MnROAD test facility (MnDOT, 2018).

Table 1. Summary of the 2017 NRRA MnROAD test Cells constructed under FRC study.

Cell number	Length (ft)	Pavement/ overlay Type	Underlying layer (constr. year)	Type of concrete/ fiber dosage*	Panel size W ft x L ft	Panel thickness (inch)
506	144	Thin pavement on gravel base	11 in. class 5Q aggregate base (2017)	*Plain concrete*	6 x 6	5
606**	138			*FRC/ standard*		
706				*FRC/ enhanced*		
806				*FRC/ high*		
139	270	Ultra-thin Pavement on gravel base	6 in. class 5 aggregate base (2017)	FRC/ enhanced	6 x 6	*3*
239	273	Thin Pavement on gravel base			6 x 6	*4*
705	144	Thin unbonded overlay on concrete pavement (w/fabric interlayer)	Concrete (1993)	FRC/ standard	*Driving: 14 x 12 Passing: 12 x 12*	5
805	124				*Driving: 6 x 12 and 8 x 12 Passing: 6 x 12 and 6 x 12*	5

** Fiber dosages: standard - corresponding to 20% residual strength ratio (ASTM C1609); enhanced - corresponding to 30% residual strength ratio (ASTM C1609); high – corresponding to 0.75 fibers volume fraction.*

*** Even though the design thickness was 5 inches, the actual measured thickness was found to be 6 inches*

Table 2. Paving dates and times of MnROAD 2017 FRC research cells.

CELL	Date	Approximate Time
139	7/17/2017	9:15:00 AM
239	7/17/2017	9:15:00 AM
506	6/26/2017	9:20:00 AM
606	6/27/2017	9:15:00 AM
706	6/29/2017	8:45:00 AM
806	6/30/2017	8:00:00 AM
705	9/5/2017	2:00:00 PM
805	9/5/2017	3:00:00 PM

Figure 1-2: Photograph of the Forta Ferro fibers used in MnROAD 2017 FRC research cells.

Table 3. Mix designs for FRC Cells (includes control mix with no fibers) (MnDOT, 2018).

MIX/CELL	AIR (%)	WATER (lbs)	CEMENT (lbs)	FLY ASH (lbs)	FLY ASH (%)	W/C RATIO	FA #1 (lbs)	CA #1 (lbs)	FIBERS (lbs/CY)	SLUMP RANGE (in.)
MR-3A21FC 506	7.0	239	400	170	30	0.42	1222	1798	-	0.5 - 3
MR-3A21F1 705, 805, 606		248	413	177			1204	1773	5	
MR-3A21F2 139, 239, 706		252	420	180			1196	1761	8	
MR-3A21F3 806		258	430	185			1184	1743	11.66	

2 PAVEMENT DISTRESSES

2.1 Cracks and Spalling

The distresses such as cracks, spalling and faulting were documented through periodical distress surveys. Table 4 provides the dates of the crack and spalling surveys and the corresponding equivalent standard axle load (ESAL). Distress surveys were conducted by visually observing and documenting the distresses on MnDOT's distress survey sheets. A summary of the distresses (cracking and spalling) documented in the second year of service (until December 2019) is provided in Figure 2-1. This figure, however, does not include the unique distresses that developed in Cell 139. The following section elaborates on the distresses observed in each cell. The distress map for all the cells, collected from MnDOT, can be found in APPENDIX A. *It shall be noted that all the data and pictures presented in this report for the distresses and different sensors are collected by MnDOT and provided to the research team*.

Table 4. List of distress survey dates.

Cell	Construction Dates in 2017	Distress Survey Dates in 2018/ ESALs	Distress Survey Dates in 2019 / ESALs
139	Jul 17	May 1/ 49K	Mar 18/ 82K; Dec 4/ 114K
239	Jul 17	May 1/ 38K	Mar 18/ 62K; Dec 4/ 85K
705	Sep 5	Mar 13/ 750K Apr 25/ 825K	Mar 18/ 1,800K; Oct 23/ 2,400K
805	Sep 5	Mar 13/ 750K; Apr 25/ 825K	Mar 18/ 1,800K; Oct 23/ 2,400K
506	Jun 26	Mar 14/ 750K	Mar 19/ 1,800K; Oct 25/ 2,400K
606	Jun 27	Mar 14/ 750K	Mar 19/ 1,800K; Oct 25/ 2,400K
706	Jun 29	Mar 14/ 750K	Mar 19/ 1,800K; Oct 25/ 2,400K
806	Jun 30	Mar 14/ 750K	Mar 19/ 1,800K; Oct 25/ 2,400K

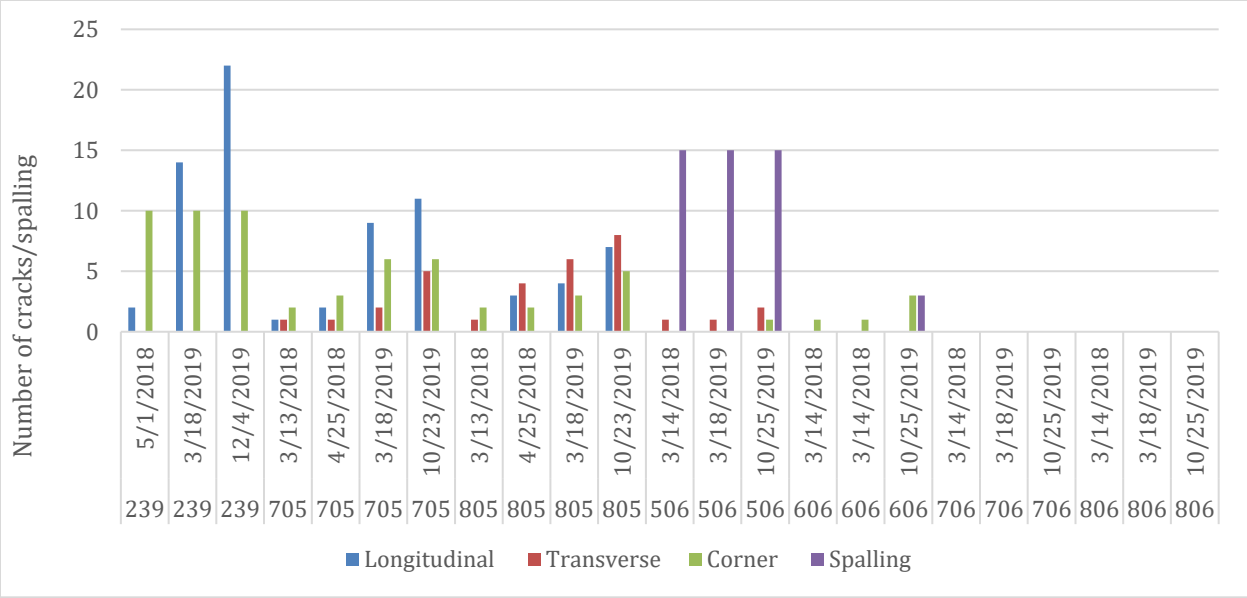

Figure 2-1. Summary of distresses observed at the MnROAD FRC research cells until the second year of service period (Cell 139 not shown).

2.1.1 Cells 139 and 239

Cell 139 was constructed with a three-inch-thick (ultra-thin) concrete pavement on an unstabilized gravel base at the MnROAD low-volume test track. The size of the slabs of this cell was 6ft x 6ft and the number of the total slabs is 180. Cell 139 was inadvertently exposed to early loads from construction trucks that were using the crossover segment to access other cells under construction, which resulted in many early-age cracks. Figure 2-2 shows a picture of a couple of such early-age cracks in this cell. These types of cracks continued to develop, propagate throughout the first year of service, and eventually, many slabs of this cell were shattered by the end of the summer of 2018. Besides that, there was a considerable amount of depression along the outer wheel path at some locations; this distress looked similar to rutting that occurs in asphalt pavement. Figure 2-3 and Figure 2-4 show photographs of the abovementioned distresses. While the slab thickness limitation (only 3-inch thick) of this cell and early-age loading were the main reasons for the initiation of the distresses of Cell 139, a relatively weak base layer and some drainage issues were believed to have aggravated the distresses of this cell.

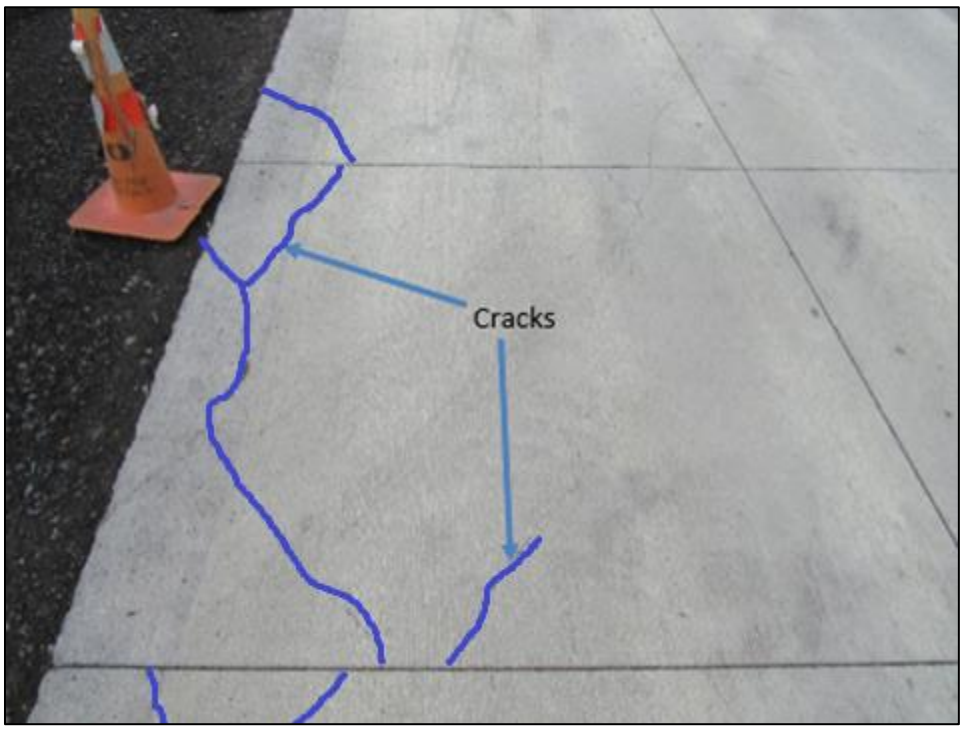

Figure 2-2. Cell 139 after exposure to construction trucks.

Figure 2-3. Shattered slabs in Cell 139 .

Figure 2-4. Depression along the wheel path in Cell 139 .

As many as 14 of the 44 slabs in the inside lane were replaced on September 27, 2018. Figure 2-5 shows a few ph collected during the removal of broken slabs and the construction of the replacement slabs. The replacement slabs are now 4-inch thick, with eight of them containing fiber reinforced concrete and the other six constructed with plain concrete. The fibers used in the replacement slabs are different and laterally stiffer than that used in 2017, as shown in Figure 2-6a. The dosage of the fiber was 5.5 lb/cy, which corresponds to a 30% residual strength ratio. Figure 2-6b shows the ASTM C1609 test results for the two numbers of beam samples prepared at the site during the construction of replacement slabs in Cell 139. The replaced slabs are performing well; no cracks have been found visible in a recent photographic survey conducted in October 2019.

(2.5 a) Removal of broken slabs for Cell 139

(2.5b) Close shot of the broken concrete pieces

(2.5c) Fibers on the fractured face of a concrete piece.

(2.5d) Preparation of the base layer for reconstruction of the broken slabs.

Figure 2-5. Photographs of the replacement and reconstruction on Cell 139 (outer slabs, inside lane).

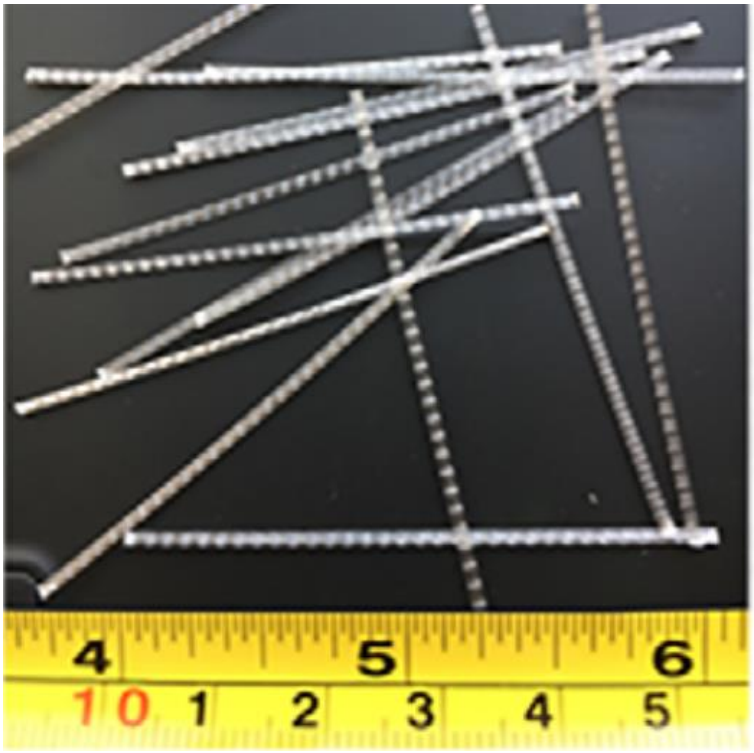

(2.6a) Fibers used in new slabs of Cell 139.

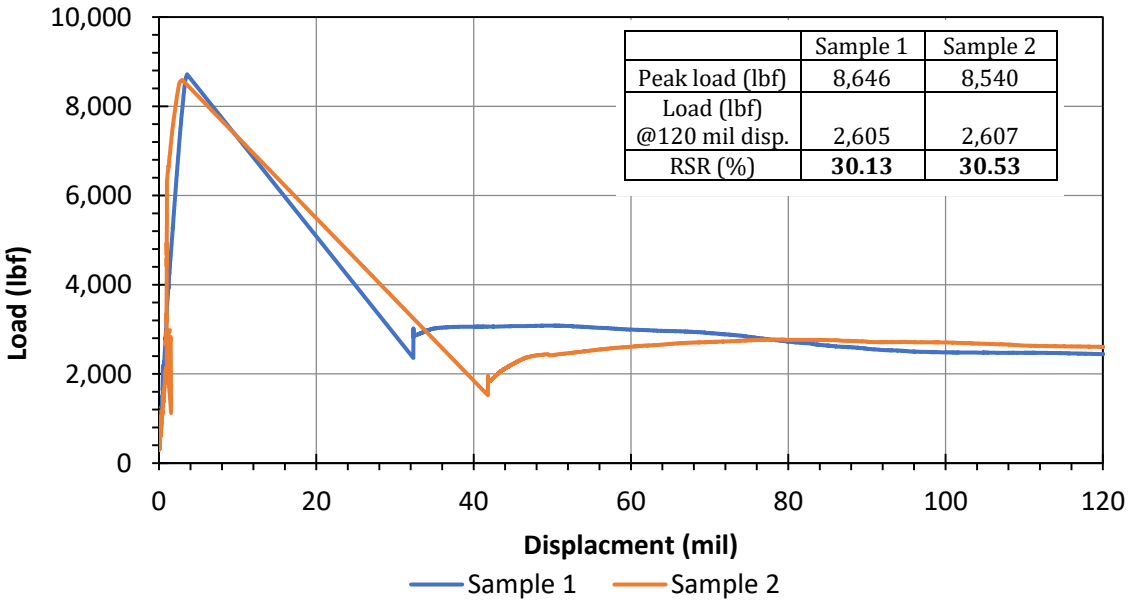

	Sample 1	Sample 2
Peak load (lbf)	8,646	8,540
Load (lbf) @120 mil disp.	2,605	2,607
RSR (%)	**30.13**	**30.53**

(2.6b) ASTM C1609 test results of the FRC concrete samples prepared during the construction of replacement slabs for Cell 139.

Figure 2-6. Photograph of fibers used in the reconstruction of Cell 139 and ASTM 1609 test results for the FRC samples.

A large number of the unrepaired slabs of this cell, however, have cracked with longitudinal cracks (primary) that resulted in many secondary cracks in transverse and diagonal directions. Based on the December 2019 distress survey data, it was found that as much as 75% of the slabs have cracked in Cell 139 after 114,000 ESALs applied to them. Figure 2-7 shows four photographs of Cell 139 taken in October 2019. The distresses are continuously progressing in the older slabs, as shown in Figure 2-7; additional shattered slabs with multiple cracks can be noticed at some locations.

Figure 2-7. A few photographs of Cell 139 during October 2019.

Cell 239 on the low-volume test track, which is a 4-inch thick concrete pavement on an unstabilized gravel base with 6ft x 6ft slabs, experienced longitudinal cracks and corner cracks. The total number of slabs in the cell is 176. Figure 2-8 shows a photograph of

typical corner cracks that formed in Cell 239 in 2018. Figure 2-9 shows a photograph of longitudinal cracks that occurred in Cell 239.

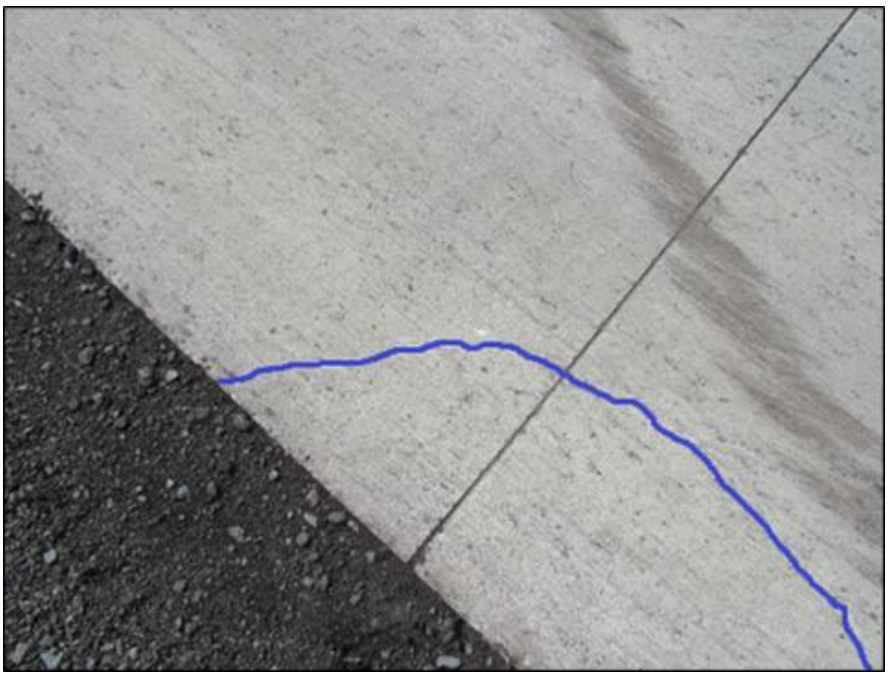

Figure 2-8. Corner cracks in Cell 239 (2018)

Nevertheless, it was found that Cell 239 performed better than Cell 139 throughout the last two years. Based on the distress survey data of December 2019, a total of 22 longitudinal cracks and 10 corner cracks have resulted in this cell, in other words, a total of 18% slabs have cracked after 85,000 ESALs.

Figure 2-9. Longitudinal cracks in Cell 239 (April 2019)

2.1.2 Cells 705 and 805

Cell 705 was constructed as a 5-inch thick unbonded concrete overlay placed over a nonwoven geotextile fabric secured to an existing 7.5-inch-thick concrete pavement constructed in 1993. Cell 705 was constructed with large slabs, 12 ft x 12 ft (passing lane) and 14 ft W x12 ft L (driving lane). This cell has a total of 22 slabs. Figure 2-10 to Figure 2-12 show photographs of typical longitudinal, transverse and corner cracks that occurred in Cell 705 in 2018. Cell 805, which was also constructed as a 5-inch thick unbonded concrete overlay, has narrower slabs compared to Cell 705, as shown in Table 1. Cell 805 has a total of 40 slabs. This cell also experienced longitudinal cracks, transverse cracks, and corner cracks. Figure 2-13 to Figure 2-15 show photographs of typical cracks in Cell 805 in 2018. Figures 2-16 and 2-17 show additional cracking that was observed in April 2019.

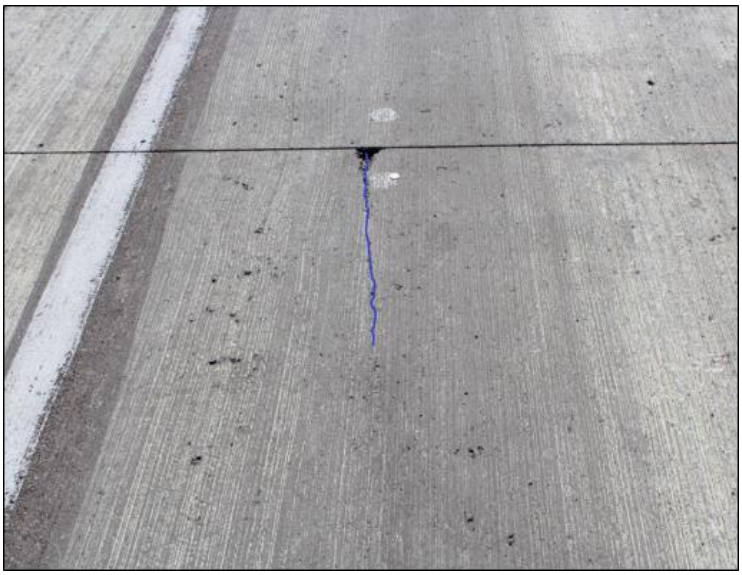

Figure 2-10. Longitudinal crack in Cell 705 (2018)

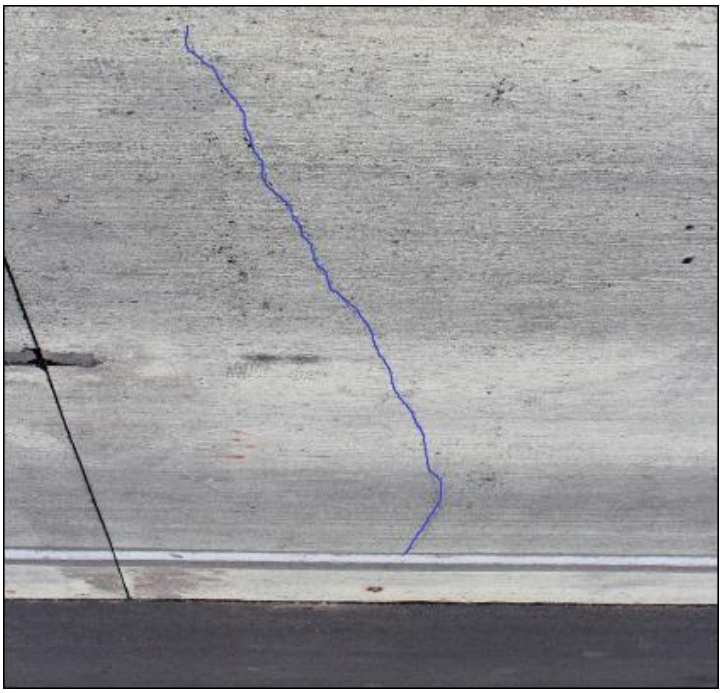

Figure 2-11. Transverse crack in Cell 705 (2018)

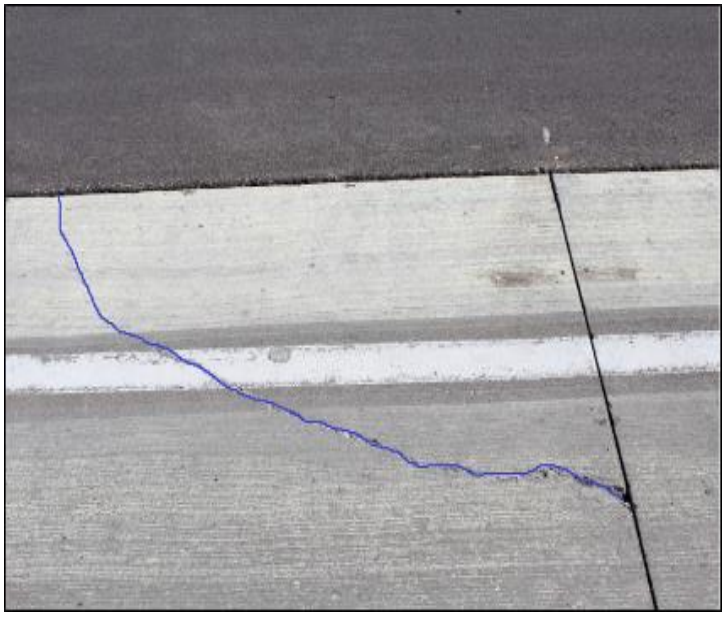

Figure 2-12. Corner crack in Cell 705 (2018)

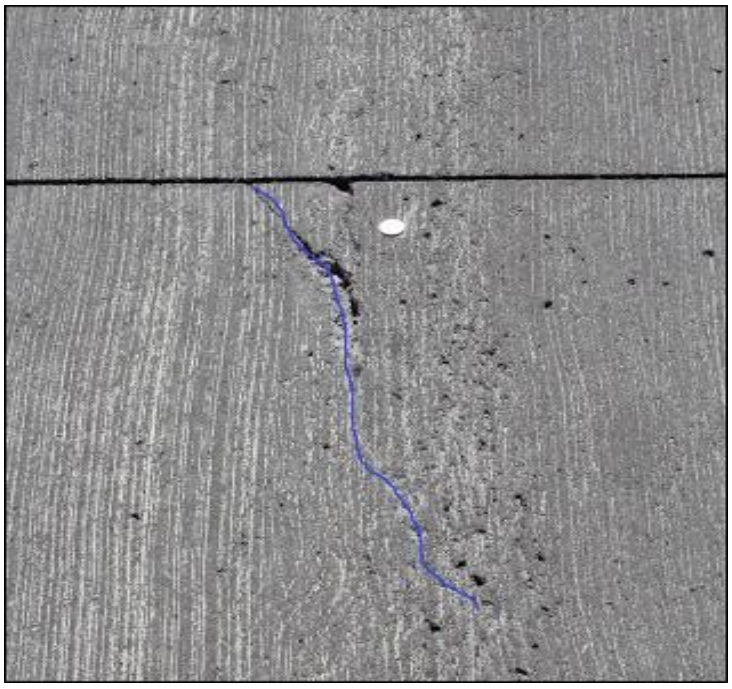

Figure 2-13. Longitudinal crack in Cell 805 (2018)

Figure 2-14. Transverse crack in Cell 805 (2018)

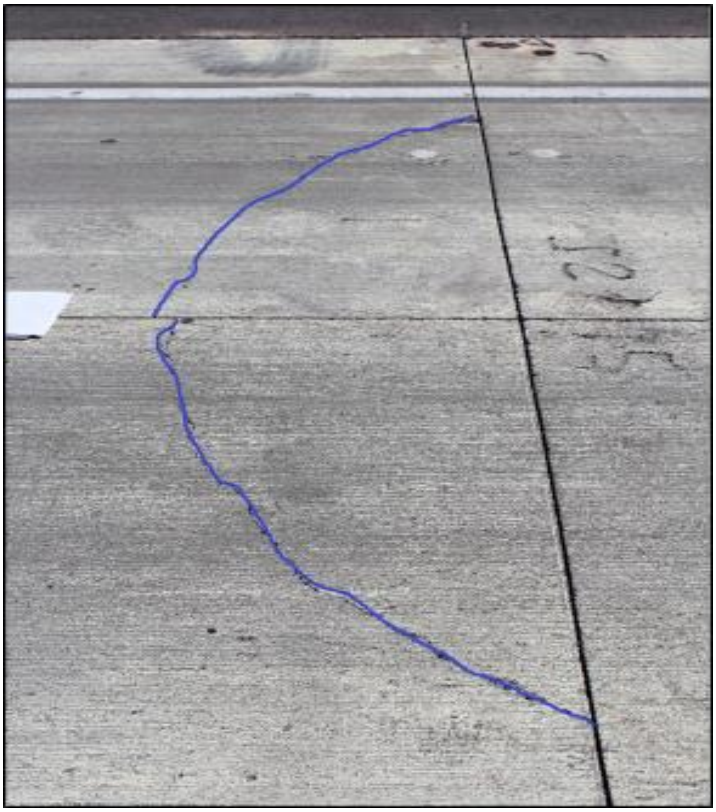

Figure 2-15. Corner crack in Cell 805 (2018)

Figure 2-16. Photographs of transverse and corner cracks in Cell 705 as observed during April 2019

Figure 2-17. Photographs of observed cracks in Cell 805 during April 2019.

Based on the distress survey conducted in October 2019, Cell 705 has 11 longitudinal, five transverse and six corner cracks. Cell 805 has experienced a total of seven longitudinal, eight transverse and five corner cracks. It was found that as many as 55% slabs of Cell 705 and 28% slabs of Cell 805 have cracked after 2.4 million ESALs of traffic load on them.

2.1.3 Cells 506 through 806

Cells 506, 706 and 806 were constructed with 5-inch thick 6ft x 6ft size slabs on an unstabilized gravel base. Cell 606 was constructed with 6-inch thick 6ft x 6ft size slabs. All of these cells were constructed on the mainline test track. Cells 506, 606, 706 and 806 have 96, 92, 76 and 88 numbers of slabs, respectively. Cell 506, which is the control cell constructed without any fibers, experienced one transverse crack and spalling on 15 numbers of transverse joints before April 2018. The October 2019 distress survey reveals that Cell 506 did experience one diagonal crack and two more transverse crack in addition to the cracks observed in 2018. Surprisingly, all three cracks developed in three adjacent slabs. Figure 2-18 and Figure 2-19 show photographs of the transverse crack and joint spalling documented in April 2018. Figure 2-20 shows the photograph of the cracks in 2019. Only 3% of slabs of this cell have cracked after 2.4 million ESALs.

Cell 606, which was constructed with 5 lbs/cy (20% residual strength) of structural fibers, experienced one corner crack prior to April 2018. This corner crack was the only crack as observed during the 2019 distress survey as well. Figure 2-21 shows photographs of the crack in April 2018 and October 2019. It can be seen that the severity of this crack did not change much as compared to what has happened for the cracks in Cell 506 (Figure 2-18 vs. Figure 2-20). As this crack is located in the last panel next to a cell transition joint, it can be assumed that this crack is not a typical fatigue-related crack, it occurred because of a construction issue.

Cells 706 and 806, which were constructed with fiber dosages of 8 and 11.7 lbs/cy, respectively, did not experience any cracks or spalling prior to October 2019 except for a couple of narrow cracks in Cell 806 originated at the location of a joint opening sensor (Figure 2-22).

Figure 2-18. Transverse crack in Cell 506 (control, non-FRC) observed in the year 2018.

Figure 2-19. Spalling in Cell 506 (control, non-FRC) observed in the year 2018.

Figure 2-20. Photographs of transverse and diagonal cracks in Cell 506 (October 2019)

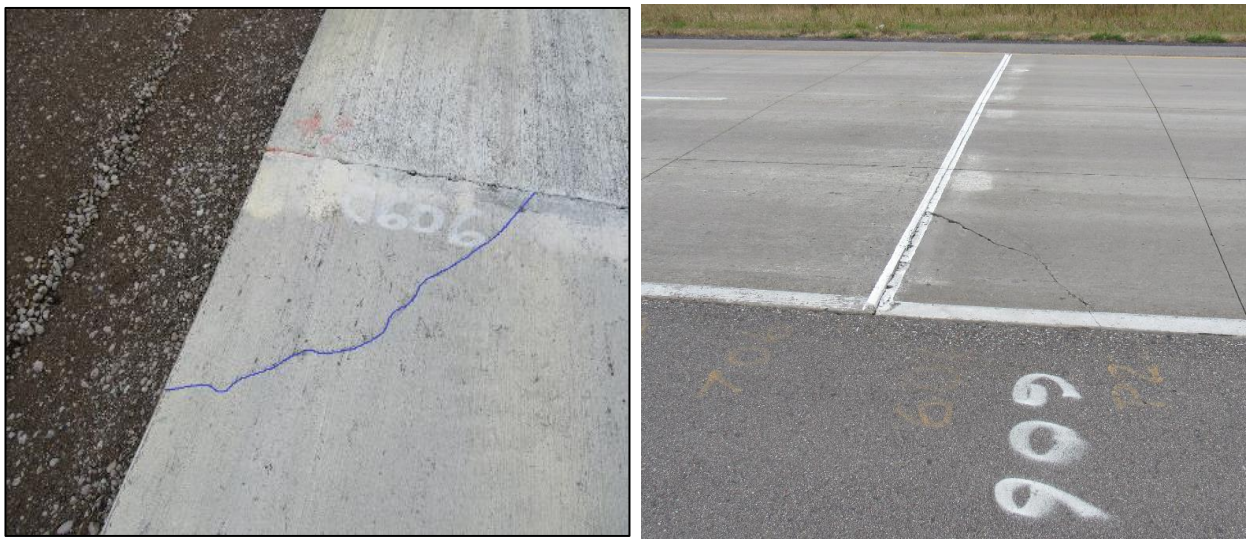

(a) (b)

Figure 2-21. Corner crack (construction issue) in the last panel of Cell 606 observed (a)in the year 2018 and (b) 2019

Figure 2-22. Narrow cracks in Cell 806, originated at the location of the joint opening sensor

2.2 Joint Faulting

In 2018, joint faulting was measured on May 3 for Cells 139 and 239, and on April 28 and October 3 for the remaining cells. During 2019, joint faulting was measured on April 24 and October 18 for the cells 139 and 239 and on April 15 and October 16 for the remaining cells. Joint faulting was measured at 10 different transverse joints in each cell, marked as Joint 1 through 10. It shall be noted that the joint number in these plots is just the serial number of joints where faulting was measured and different from the MnDOT's assigned joint numbers. Joint faulting was measured using a modified Georgia DOT style faultmeter.

2.2.1 Cells 139 and 239

Figure 2-23 shows the faulting measured at various transverse joints of Cells 139 and 239. It should be noted that the surface texture depth is usually around 1 mm on average; therefore, any faulting readings below 1 mm may not be indicating any notable faulting. As previously mentioned, Cell 139 had experienced depression along the wheel path, so, it may not also be appropriate to compare the faulting results between Cells 139 and 239.

Interestingly, faulting results for Cell 239 showed mostly negative values. In general, a negative faulting value indicates that the leave side of the joint is at a higher elevation than the approach side. Negative faulting is usually not typical (Selezneva et. al., 2000), but since the magnitude of the faulting in Cell 239 is below -1 mm, it can be stated that there was not any notable faulting until the second year of service (2.4 million ESALs), at least at the joints where the faulting values were recorded.

2.2.2 Cells 705 and 805

Figure 2-24 shows the faulting for Cells 705 and 805 until October 2019. Both Cells 705 and 805 had shown mostly positive faulting. One noticeable observation was that the faulting at Joint number-2 and- 4 of Cell 705 was higher in April 2019 than what was measured in October 2019. Even though the faulting values in these cells were around 1 to 2 mm, Cell 805 experienced a slightly higher amount of faulting. It may happen that the narrower and lighter slabs in Cell 805 compared to Cell 705 move relatively more under the wheel load.

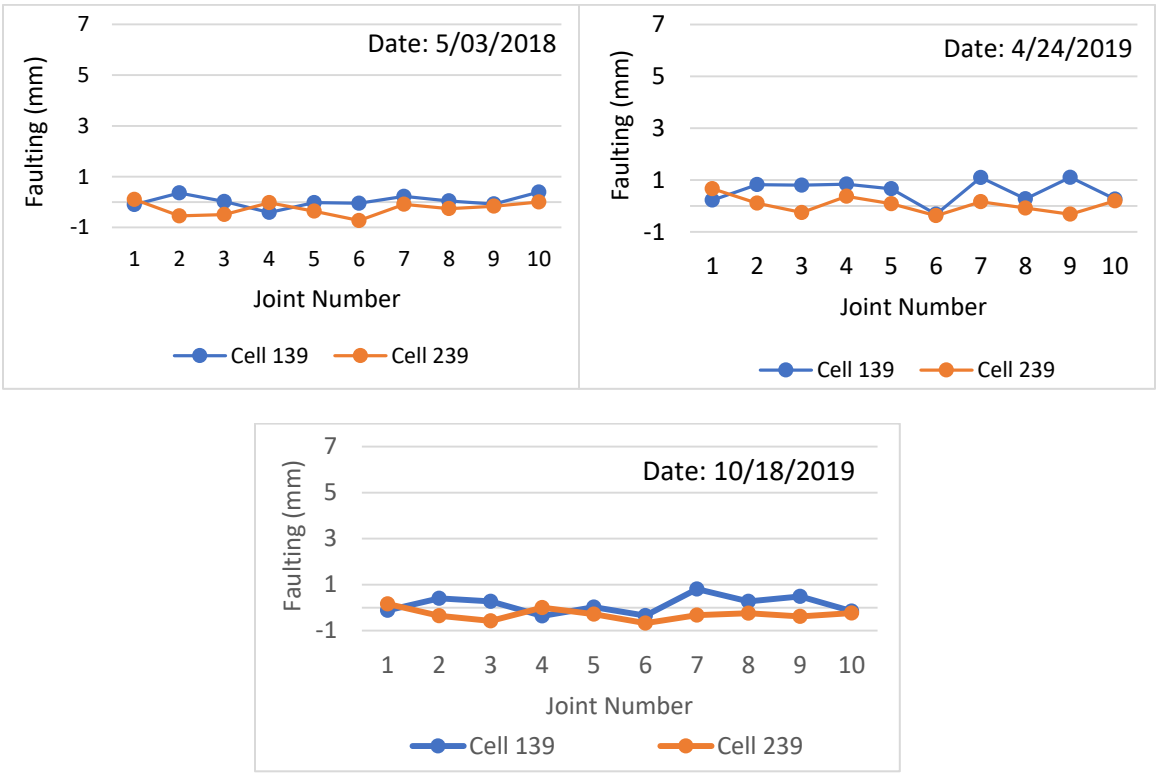

Figure 2-23. Faulting summary of Cells 139 and 239 at three different dates until October 18, 2019.

2.2.3 Cells 506 through 806

Figure 2-24 also shows the faulting measured in Cells 506, 606, 706 and 806 until October 2019. Cell 506, which was constructed with plain concrete, experienced the highest faulting (up to 4.2 mm) among the four cells. Figure 2-25 shows a photograph of noticeable faulting in Cell 506 (note that there is a sunken corner crack in the leave slab which exaggerates the faulting in the photo). Figure 2-26 shows the trend of average faulting versus fiber dosage. It can be seen that Cell 606, which was 6-inch thick (higher aggregate interlock) and constructed with a fiber dosage of 5 lbs/cy experienced approximately 86% less faulting than Cell 506 until October 2019. Cell 706, with a fiber dosage of 8 lb/cy, also experienced less faulting than Cell 506. Cell 806 which had the highest fiber dosage at 11.7 lbs/cy, experienced significantly lower faulting compared to any other FRC cell.

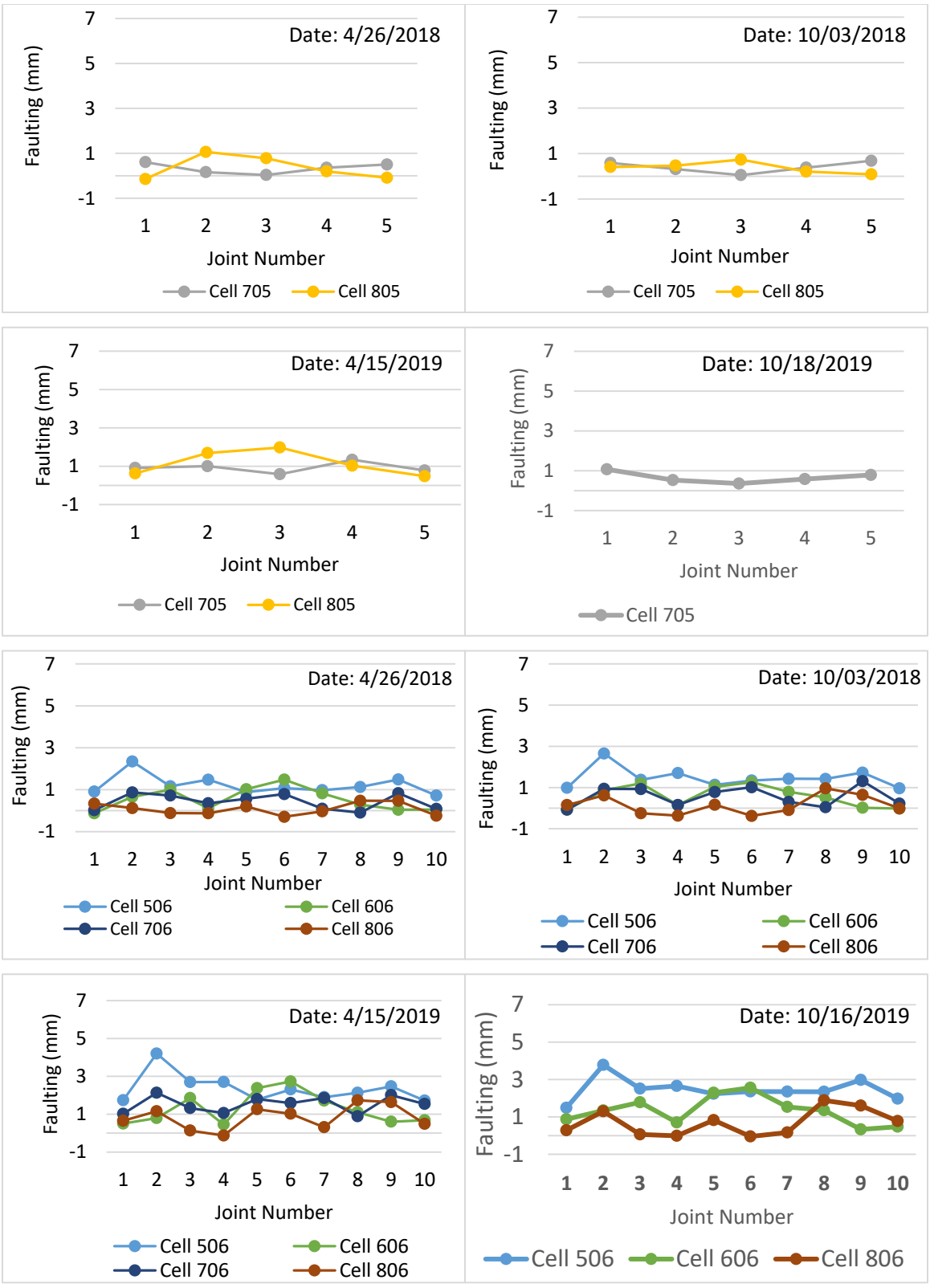

Figure 2-24. Faulting summary of Cells 705, 805 and 506 through 806 until October 18, 2019.

Figure 2-25. Photograph of faulting of Cell 506 (non-FRC). Note that faulting is exaggerated due to the broken corner in slab on leave slab.

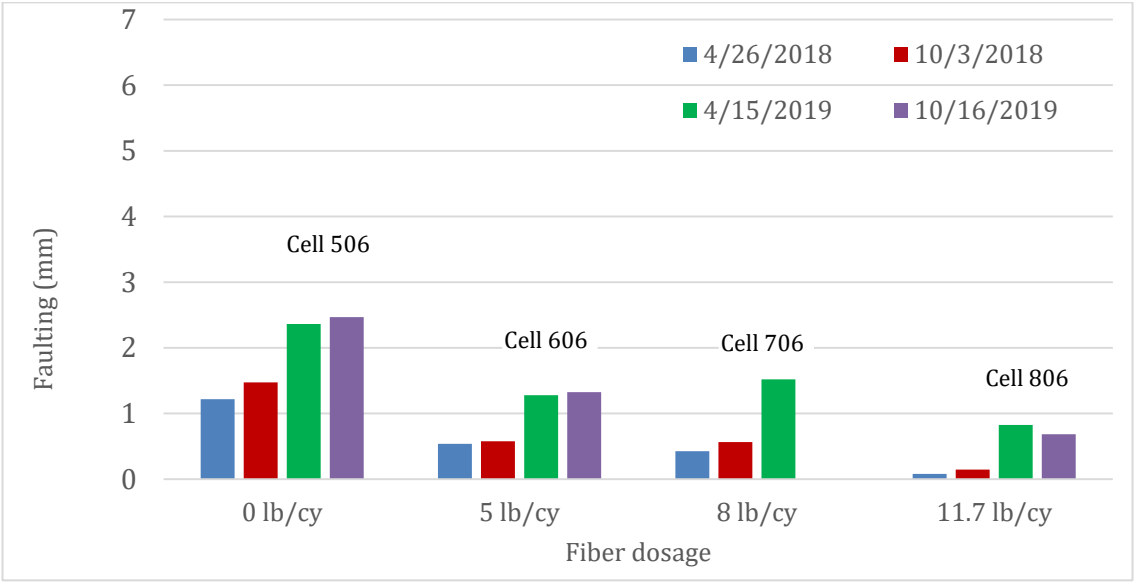

Note: Faulting for each cell is the average of all the faulting readings taken in a cell. Faulting data of Cell 706 for the April 2019 was erroneous, so discarded.

Figure 2-26. Faulting for Cells 506 through 806 with respect to fiber dosage.

3 ANALYSIS OF SENSOR DATA

MnROAD 2017 FRC research cells were instrumented with four types of sensors: joint opening, dynamic strain gauge, vibrating wire strain gauge, and temperature sensors (thermocouples). Figure 3-1 through Figure 3-8 shows the sensor plans for all eight cells. This section provides an analysis of the data collected from these sensors so far.

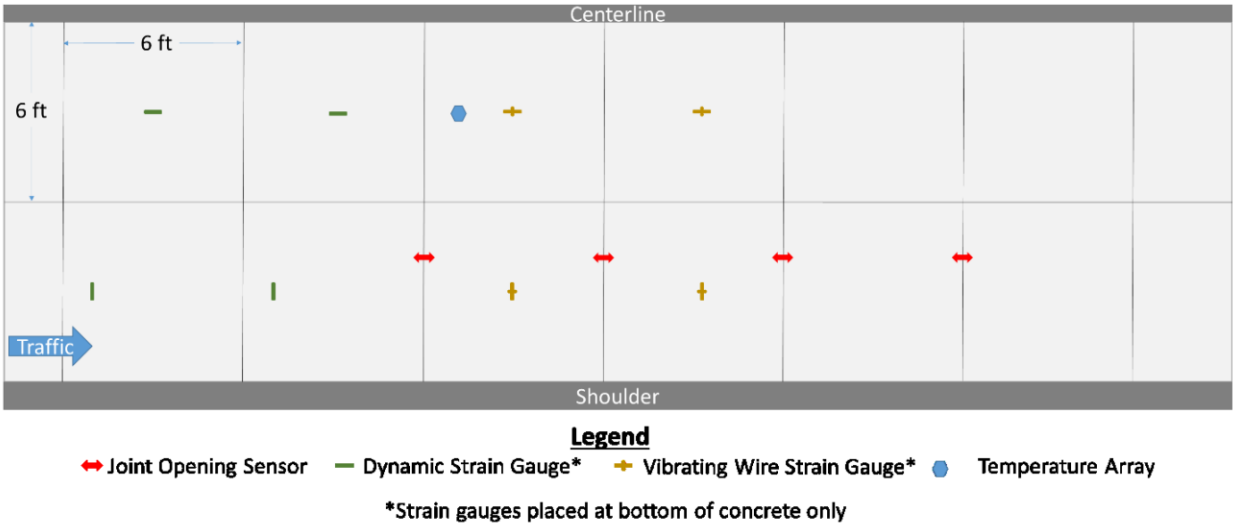

Figure 3-1. Sensor plan for Cell 139, inner lane (MnDOT, 2018).

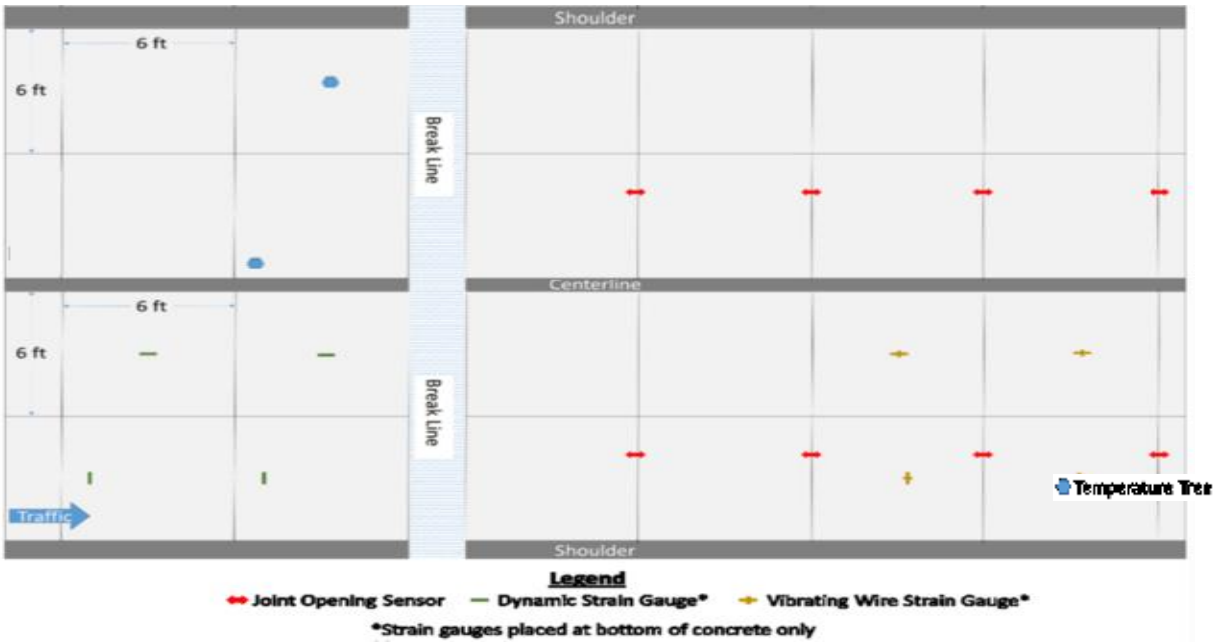

Note: Temperature trees are installed in the outer lane.

Figure 3-2. Sensor plan for Cell 239, inner lane (MnDOT, 2018).

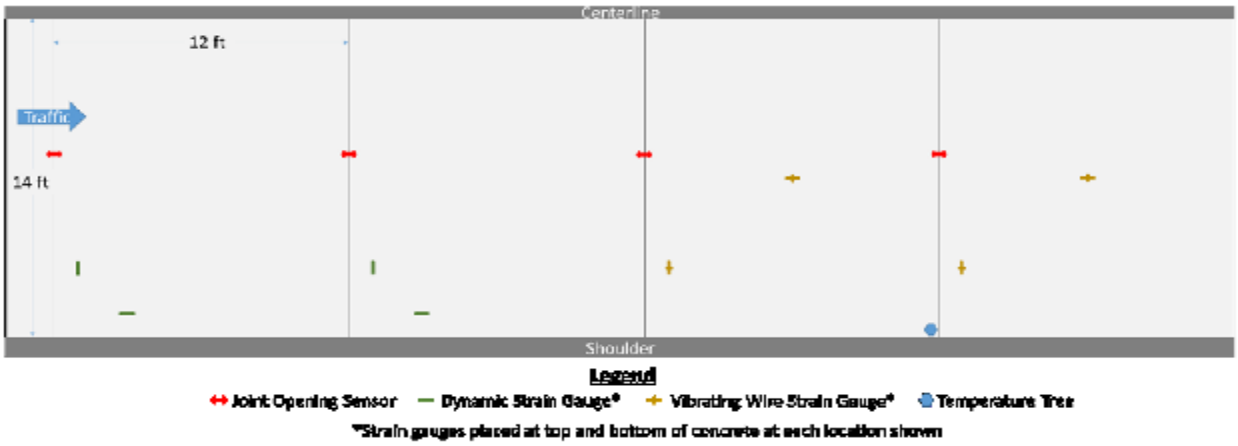

Figure 3-3. Sensor plan for Cell 705, driving lane (MnDOT, 2018).

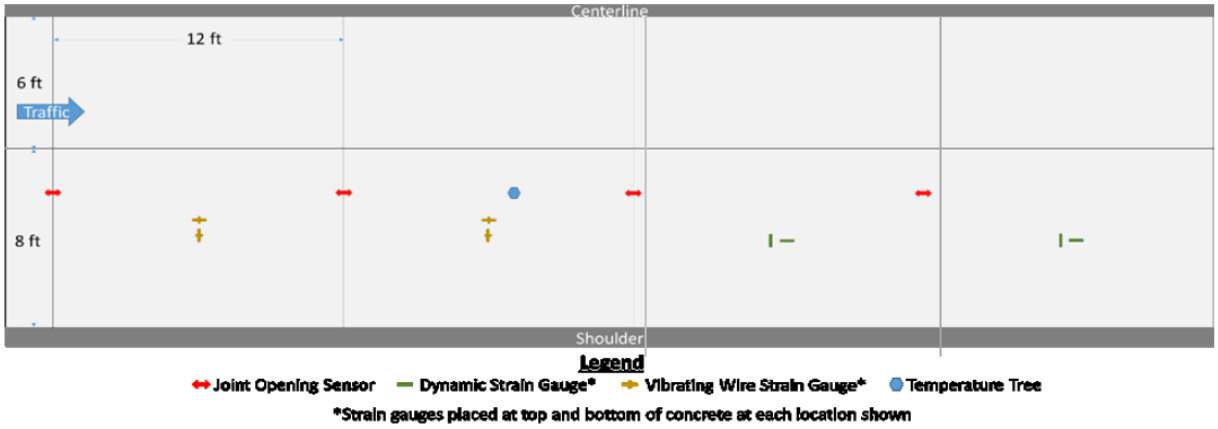

Figure 3-4. Sensor plan for Cell 805, driving lane (MnDOT, 2018)

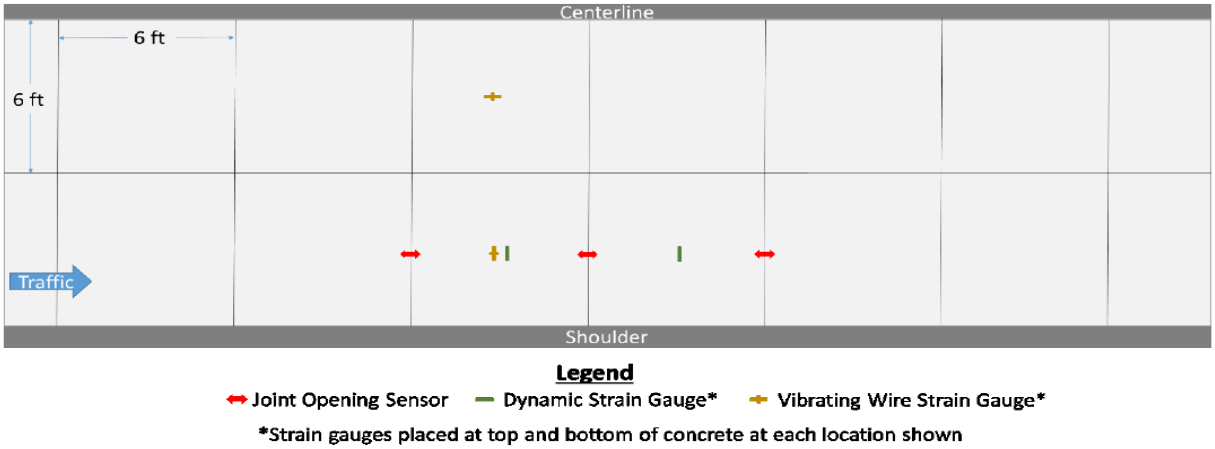

Figure 3-5. Sensor plan for Cell 506, driving lane (MnDOT, 2018).

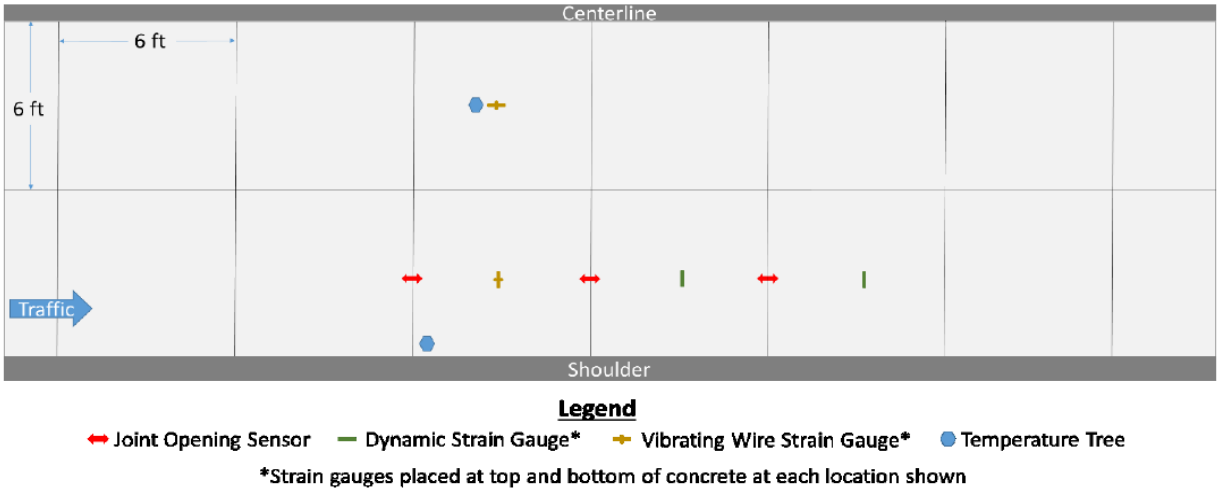

Figure 3-6. Sensor plan for Cell 606, driving lane.

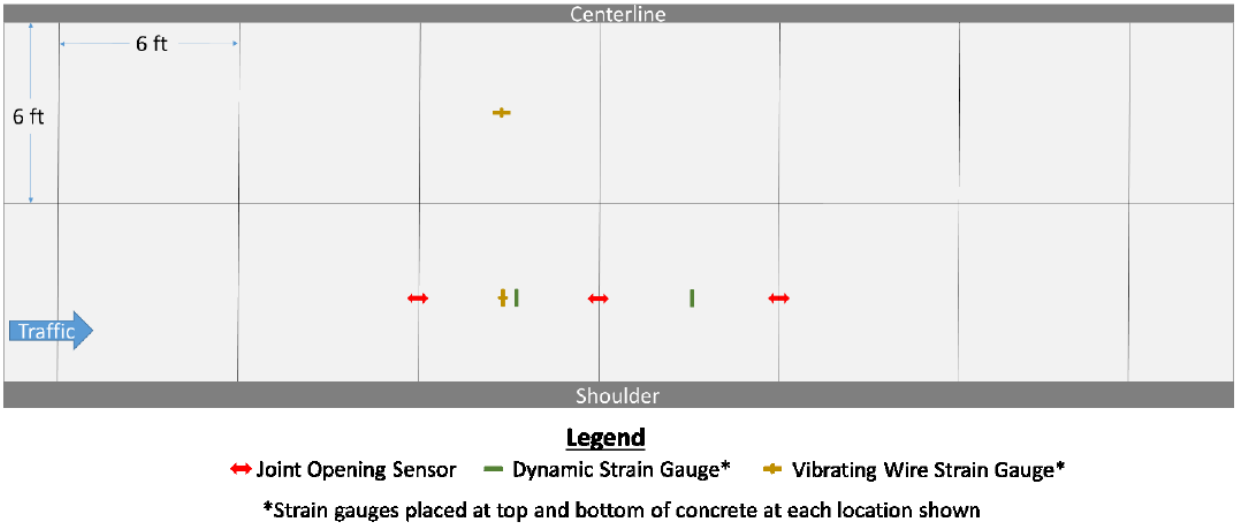

Figure 3-7. Sensor plan for Cell 706, driving lane.

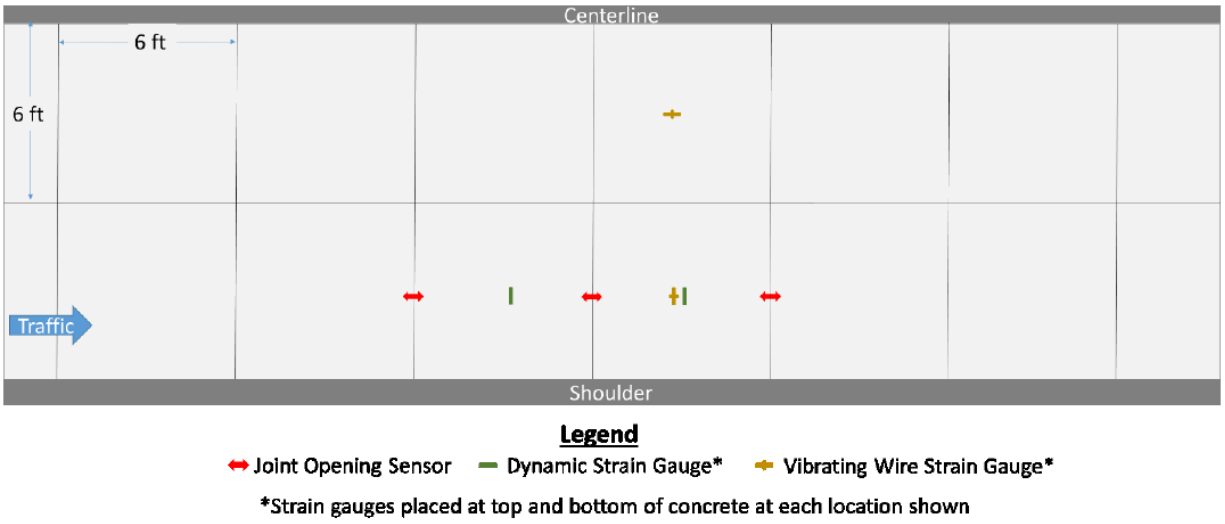

Figure 3-8. Sensor plan for Cell 806, driving lane.

3.1 Temperature

Daily and seasonal variations of temperature have a significant influence on the performance of the concrete pavement. A large number of thermocouple sensors were installed at MnROAD 2017 FRC research cells to capture the variations of temperature as well as temperature-gradient in the concrete slab. Thermocouples were installed at different depths within and beneath the slabs. Figure 3-9 shows an example of a thermocouple sensor tree installed in Cells 139, 239, 705, 805, and 606. One sensor tree was installed in each of the Cells 139, 705, and 805; two trees were installed in Cells 239 and 606, located at different offsets from the centerline. For this report, to distinguish between the two sensor trees in Cells 239 and 606, the farthest sensor tree from the centerline was designated as the outer sensor and the sensor tree closest to the centerline as the inner sensor. All of the thermocouple sensors were programmed to record temperature data every 15 minutes. In addition to collecting pavement temperature data, ambient temperature data is also collected at MnROAD using an external weather station, which is capable of collecting other ambient parameters like, precipitation, relative humidity, wind speed, wind direction, etc. Figure 3-10 shows the variation of the ambient temperatures collected from mid-June 2017 to November 2019. As shown in this figure, it can be seen that January 29, 2019, was the coldest day with a temperature of -34.2^{o}C and December 31, 2017, was the second coldest day at MnROAD with -29.5^{o}C temperature. On

the other side, May 28, 2018, was the warmest day with a temperature of 37°C. The variation of the relative humidity at the MnROAD Project site from 2017 summer to 2019 winter is provided in Figure 3-11. As anticipated, the relative humidity during the winter months was less than the rest of the year.

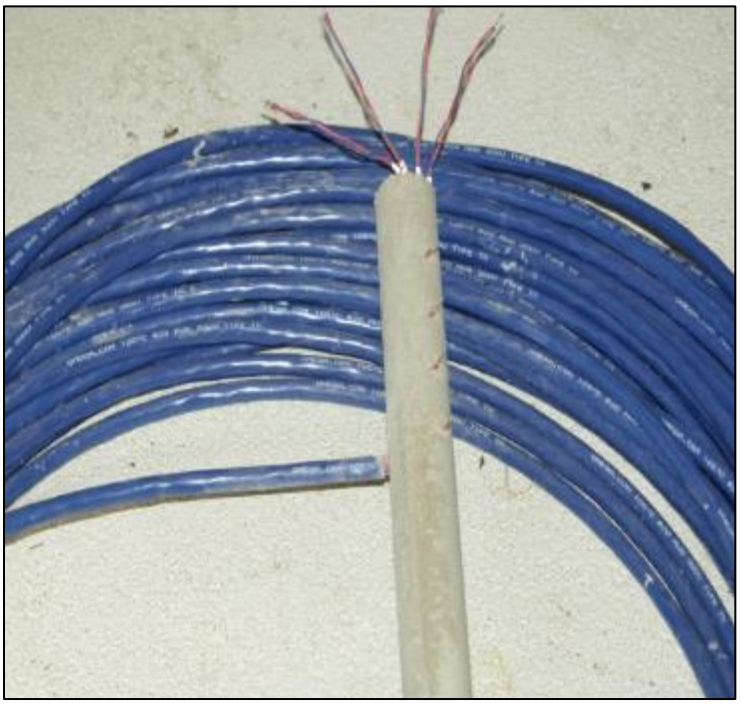

Figure 3-9. Example of a thermocouple sensor tree.

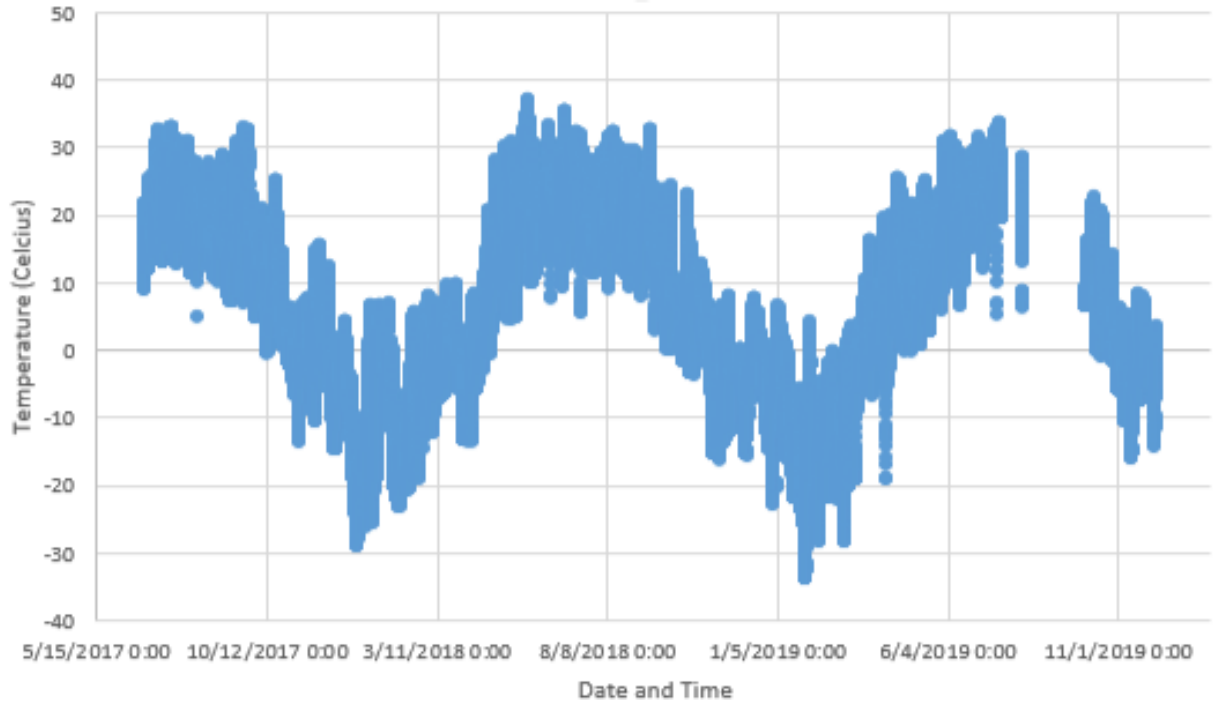

Figure 3-10. The ambient temperature at the MnROAD Project site.

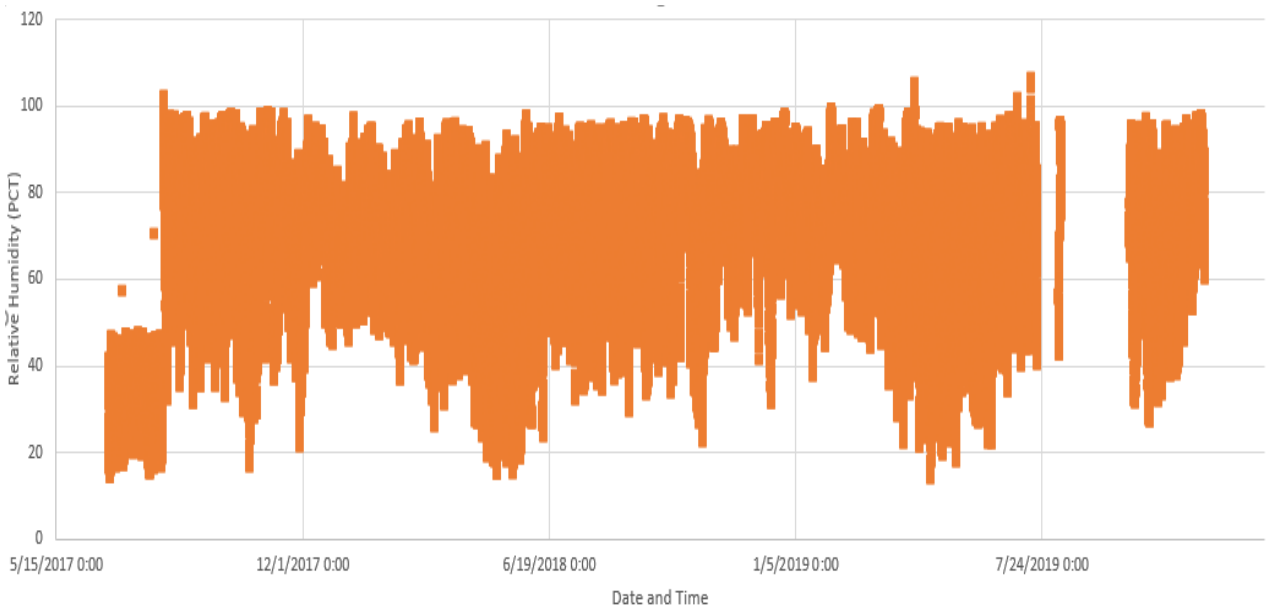

Figure 3-11. Relative humidity variation at the MnROAD Project site.

3.1.1 Pavement Temperature

The pavement slab temperature data for the cells equipped with thermocouples are shown in Figure 3-12 through Figure 3-18. These figures contain several plots, each with temperatures recorded at different depths of the slab. As expected, the general trends of

the seasonal temperature variations are similar for all the cells and align well with the ambient temperature trend, shown in Figure 3-10. The maximum and minimum temperatures recorded for each cell and their respective dates of occurrence and times are summarized in Table 5. The dates of the coldest temperatures for all the cells were recorded on January 30, 2019, while the majority of the cells had experienced their warmest day on May 28, 2018. Cell 139 experienced the warmest day on the date of its paving, i. e. July 17, 2017. The inner thermocouple tree of the Cell 239 also experienced the warmest temperature on July 17, 2017, on its paving date. These observations indicate that the Cells 139 and 239 were constructed on a relatively warmer day, and the recorded highest temperatures probably were influenced by the heat of hydration of the cement.

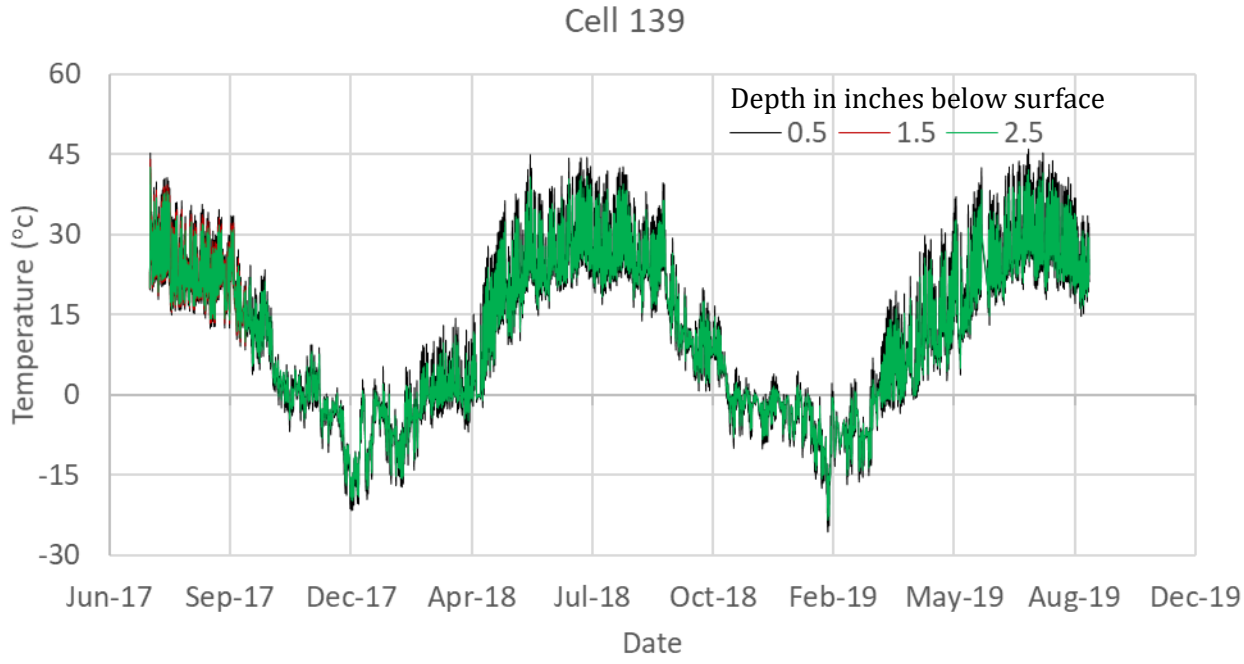

Figure 3-12. Temperature profile of Cell 139.

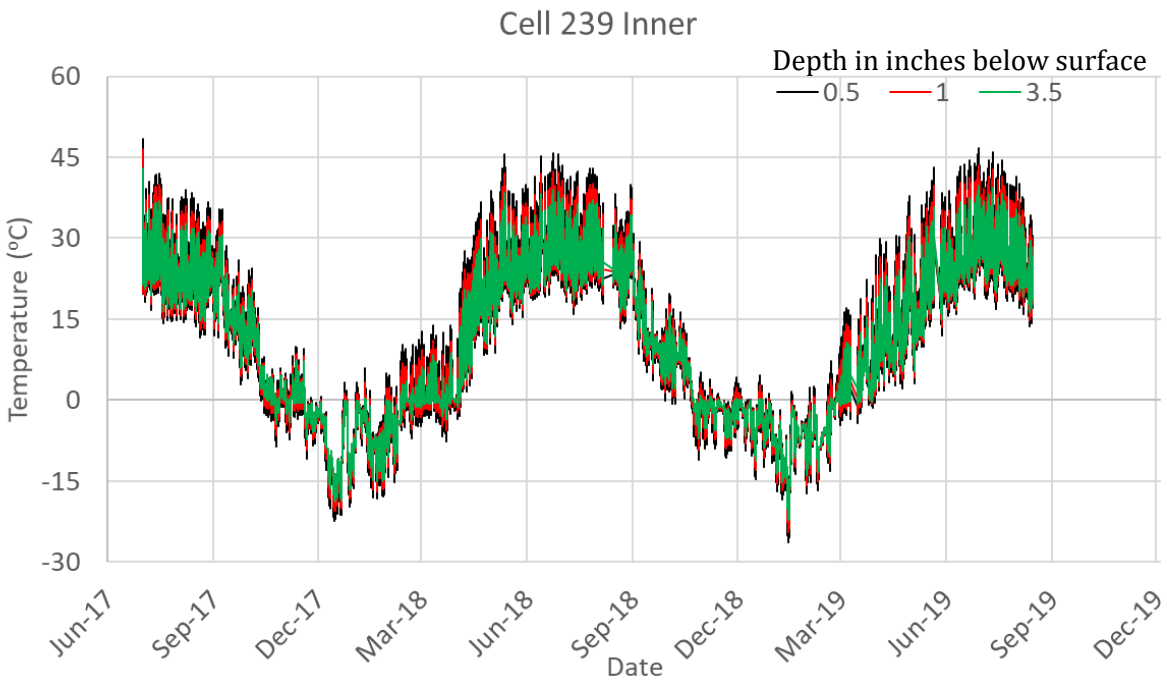

Figure 3-13. Temperature profile of Cell 239 inner lane.

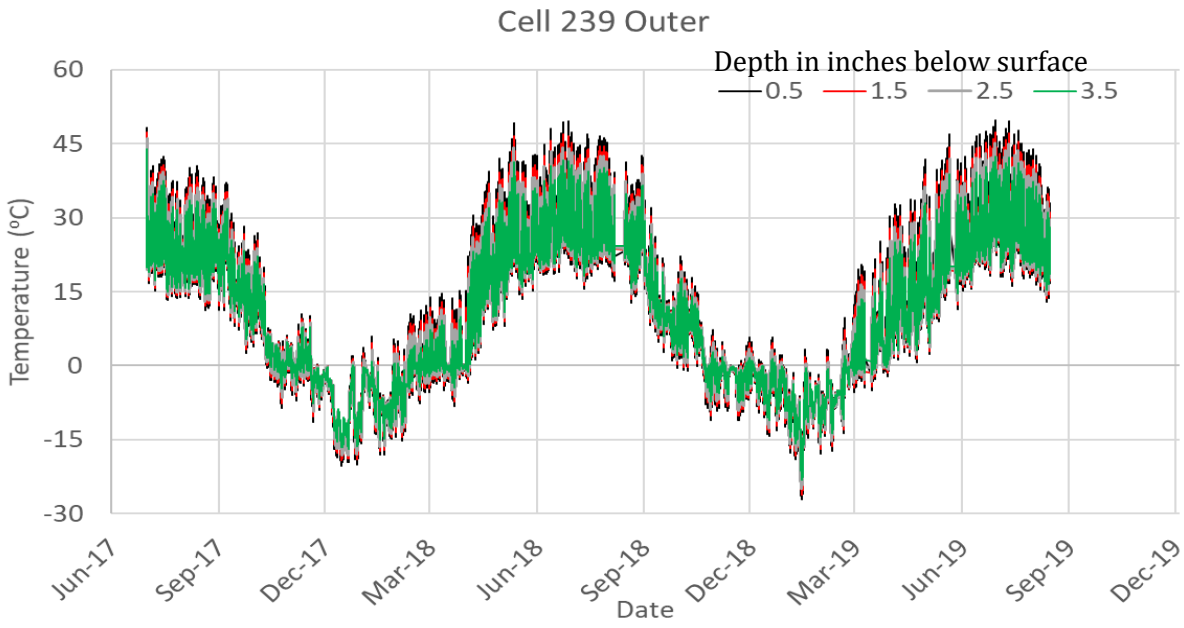

Figure 3-14. Temperature profile of Cell 239 outer lane.

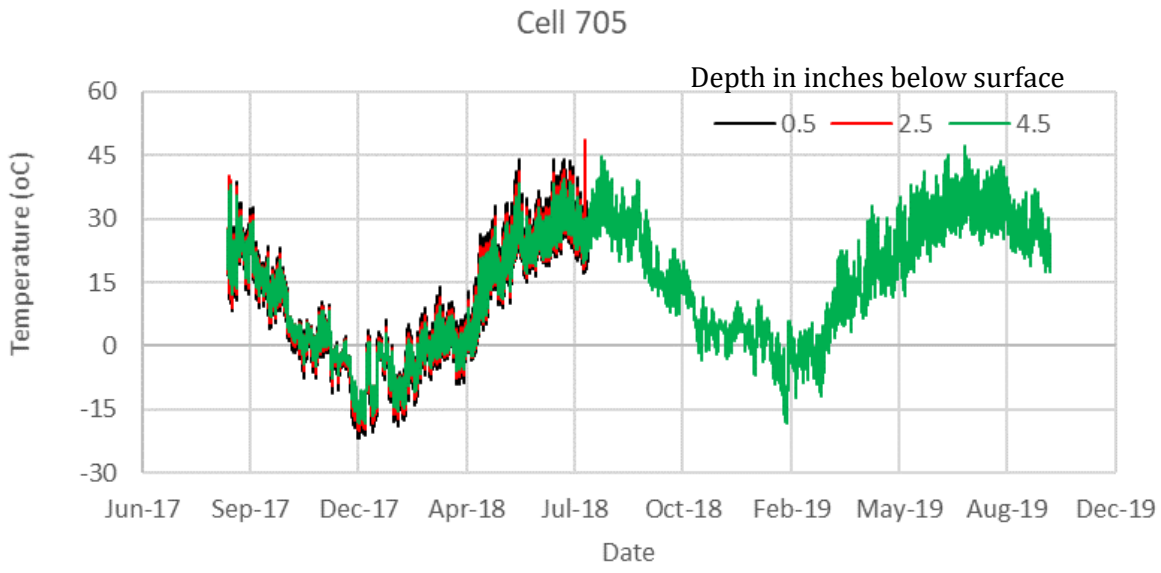

Figure 3-15. Temperature profile of Cell 705.

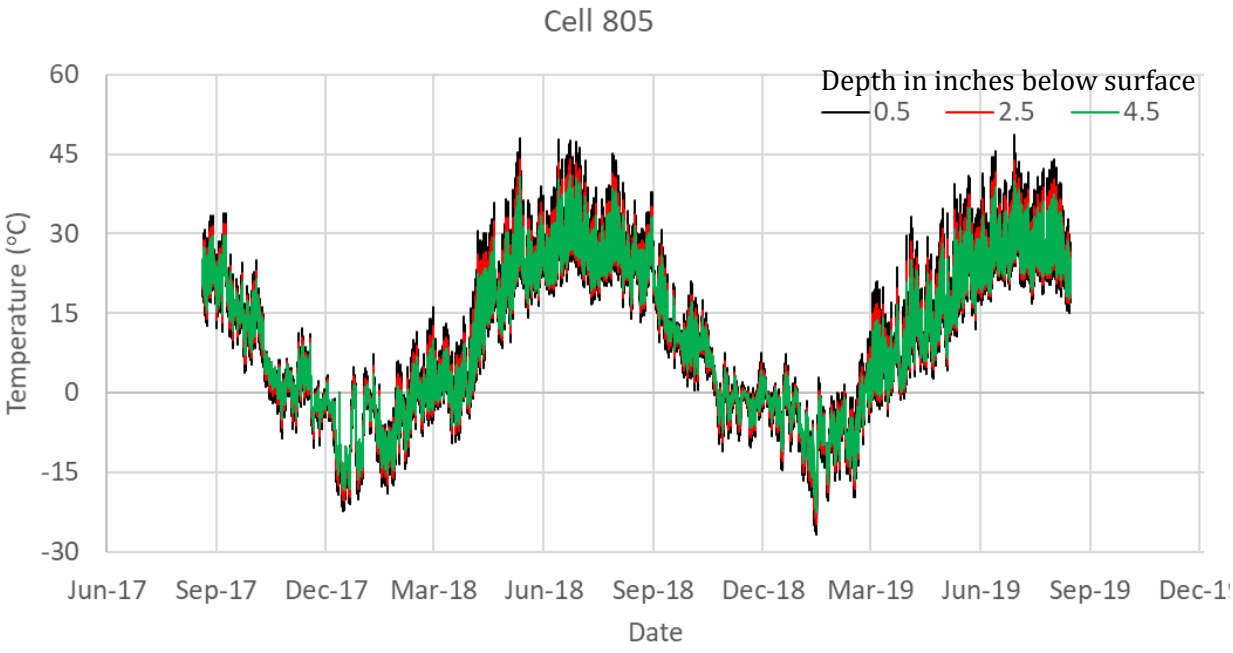

Figure 3-16. Temperature profile of Cell 805.

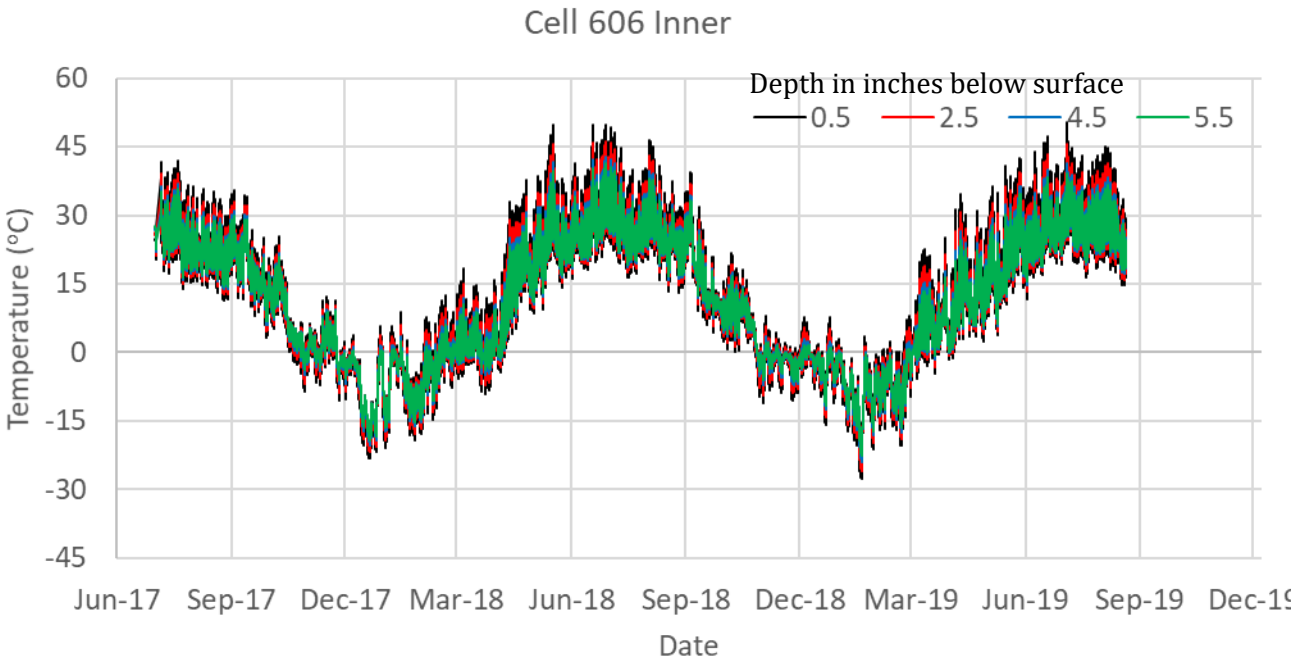

Figure 3-17. Temperature profile of Cell 606 inner lane.

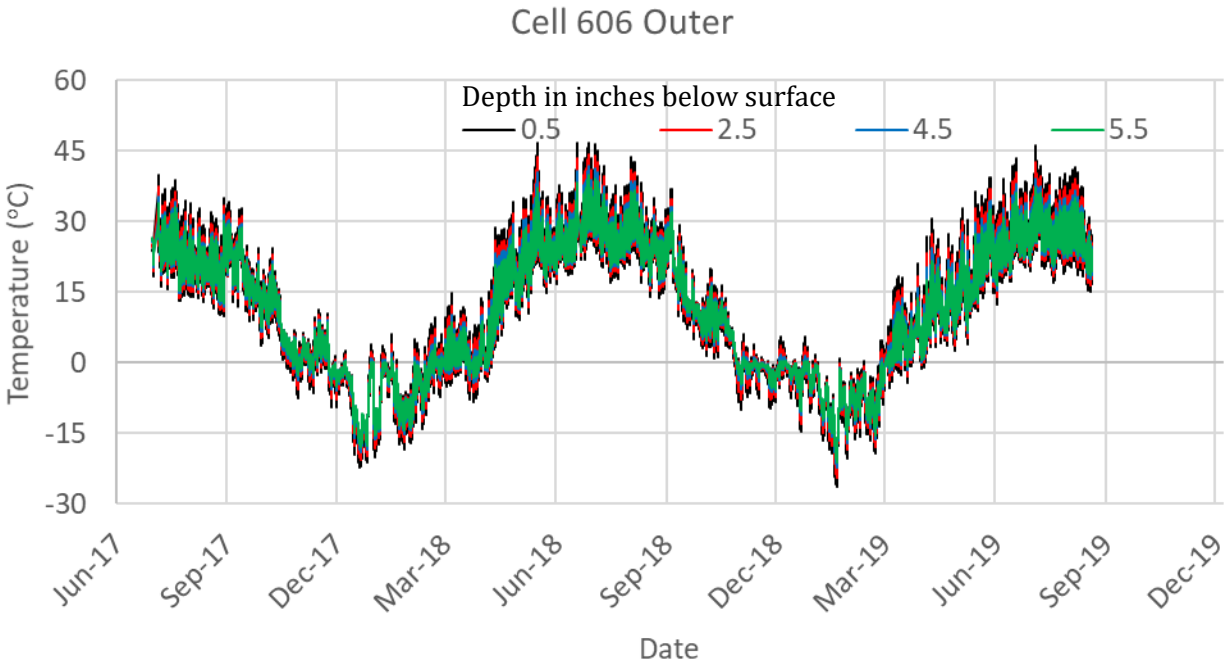

Figure 3-18. Temperature profile of Cell 606 outer lane.

Table 5. Cell extreme temperatures and respective dates and times.

Cell		Temperature °C	Date	Time
129	Max	46.01	7/15/19	3:30 PM
	Min	-25.68	1/30/19	7:45 AM
239	Max Outer	49.77	5/28/18	2:15 PM
	Min Outer	-27.21	1/30/19	7:30 AM
	Max Inner	48.33	7/17/17	2:45 PM
	Min Inner	-26.43	1/30/19	7:00 AM
705	Max	47.2	7/15/19	3:45 PM
	Min	-21.82	12/31/17	8:45 AM
805	Max	47.92	5/28/18	2:45 PM
	Min	-22.42	12/31/17	8:45 AM
606	Max Outer	46.71	7/9/2018	3:45 PM
	Min Outer	-26.41	1/31/2019	7:30 AM
	Max Inner	50.25	7/15/2019	3:15 PM
	Min Inner	-27.7	1/31/2019	7:30 AM

Note: Temperature reading collected at different depths of slabs are considered.

The relationship between the temperature and depth of the slab was studied to determine the nature of the temperature variation (either linear or non-linear). Figure 3-19 and Figure 3-20 show the temperature profiles of various cells resulted in during their coldest and warmest temperature events, respectively. Temperature profiles for various cells at an intermediate temperature, observed on April 24th, 2019, are studied as well, as shown in Figure 3-21. The general nature of the temperature variation with respect to the depth of the slab was linear, except for Cell 239, which showed a slightly non-linear nature; the reason for a distinct trend of the temperature variation in Cell 239 is not known. One possible reason could be that the thermocouple attached to the tree at one-inch depth moved downwards, because of the construction related issue. The relatively lower thickness of the slabs in this study compared to the conventional concrete pavements may be the reason for the linear temperature gradients in all other cells. As the cells (except Cell 239) experienced linear temperature gradients, the analysis has been restricted to the linear temperature gradient only.

3.2 Linear Temperature Gradient (LTG)

The linear temperature gradient (LTG) was determined by subtracting the temperature of the bottommost sensor from the temperature of the topmost sensor of a slab and then divided by the vertical distance between these sensor locations in question. A negative temperature gradient indicates that the pavement is colder at the top and warmer at the bottom, and a positive temperature gradient indicates the opposite scenario. At negative and positive temperature gradients, slabs experience upward and downward curling, respectively. In this work, temperature gradients were calculated every 15 minutes, then the monthly extreme positive and negative LTGs were determined as shown in Table 6 to Table 8.

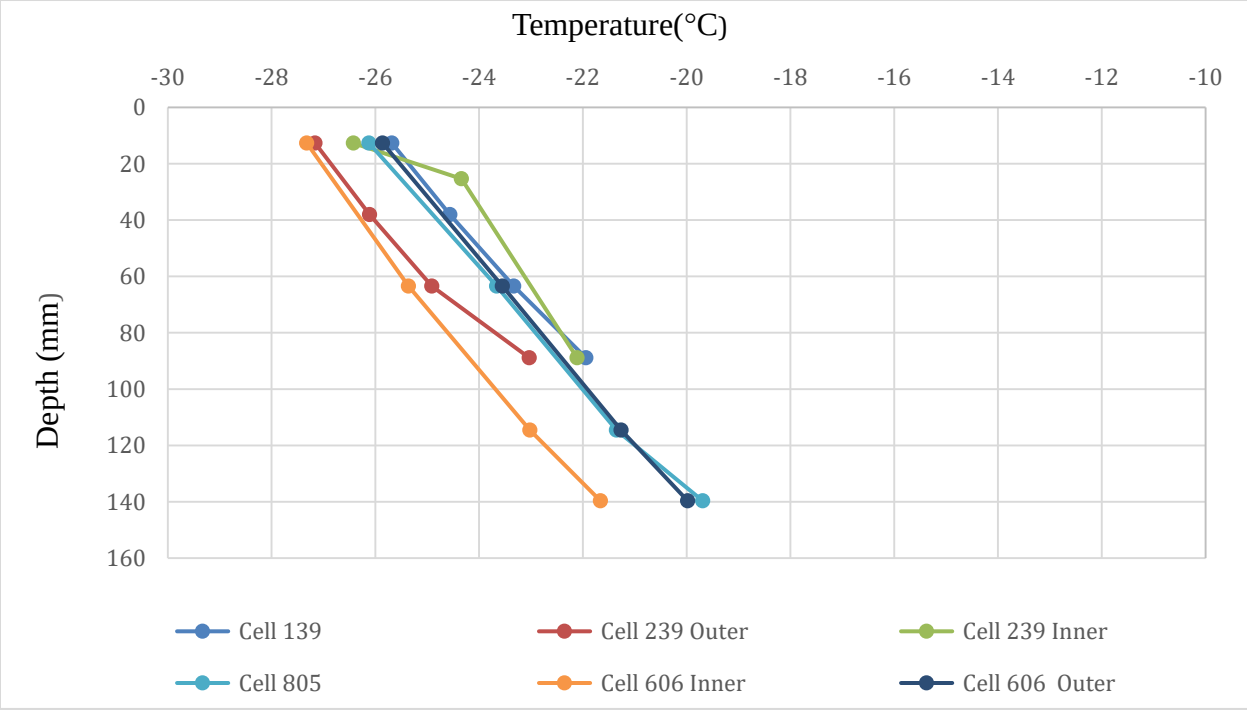

Figure 3-19. Temperature vs. slab depth on the coldest day, January 30, 2019, 7:45 AM.

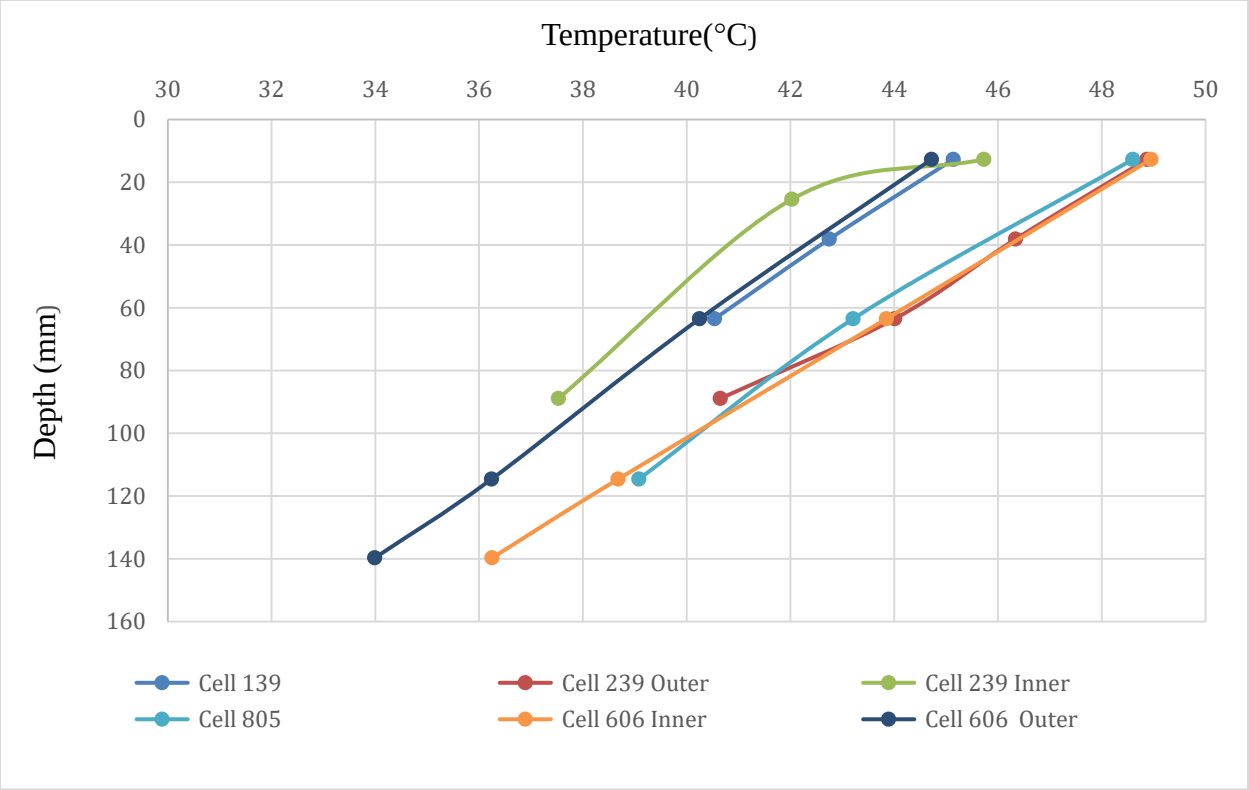

Figure 3-20. Temperature vs. slab depth on the warmest day, July 15, 2019, 2:30 PM.

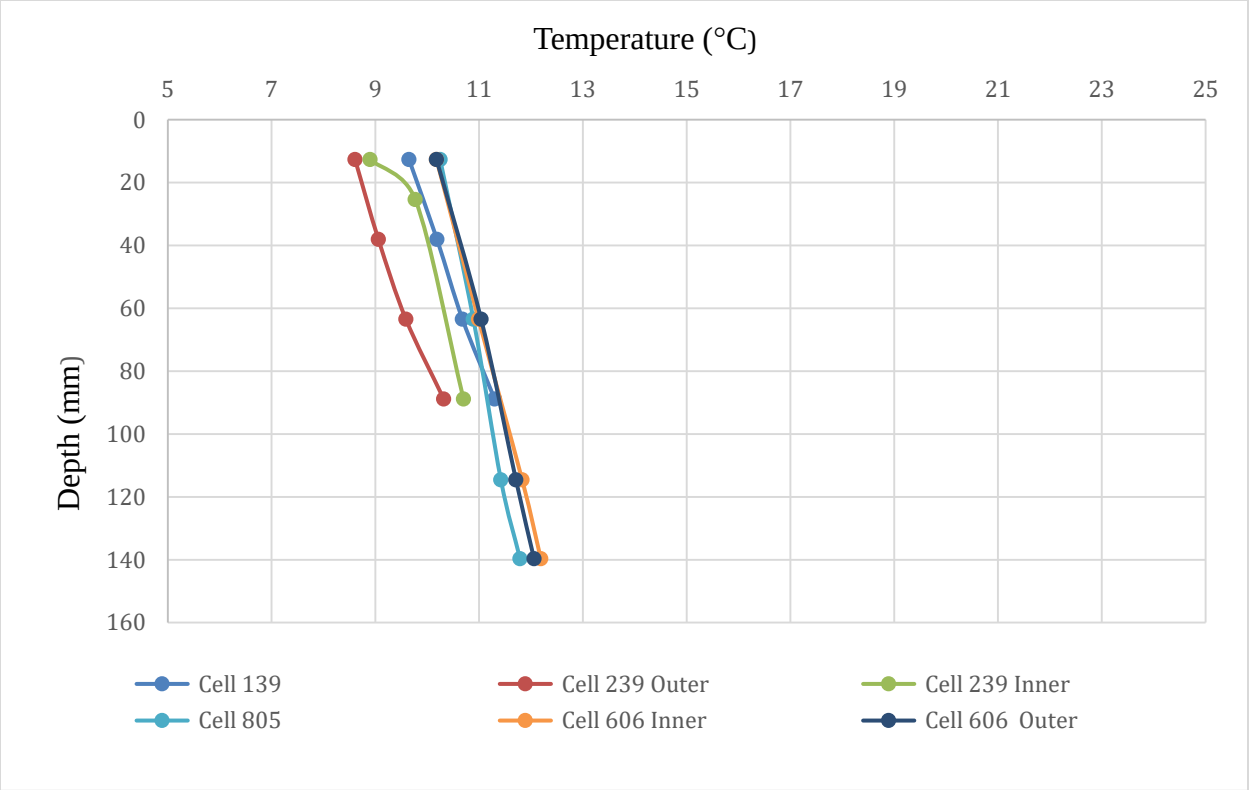

Figure 3-21. Temperature vs. slab depth at an intermediate temperature on April 24, 2019, 4:15 AM.

Table 6 shows the monthly maximum and minimum LTGs for Cells 139 and 239. Cell 139 had the highest positive LTG of 1.19°C/cm in July and September 2018 and April 2019. The highest negative LTG for cell 139 was -0.99 °C/cm in July 2019. The outer sensor tree of Cell 239 had the highest LTG of 1.61 °C/cm in April 2018 and the highest negative LTG of -1.63°C/cm in July 2019, while the inner sensor tree had the highest positive LTG of 3.37°C/cm in July 2019 and the lowest LTG of -0.99 °C/cm in July 2019.

Comparing the inner sensor tree to the outer sensor tree in Cell 239, it can be seen that the outer sensor tree showed larger temperature gradients. Also, the linear temperature gradients of the inner sensor trees of Cells 139 and 239 were found to be similar.

Table 6. Max. and Min. linear temperature gradient results for Cells 139 and 239.

Temperature Gradient (°C/cm)						
	Cell 139 (3-inch)		Cell 239 (4-inch)			
	Inner		Outer		Inner	
Month	Negative	Positive	Negative	Positive	Negative	Positive
Jul-17	-0.65	0.81	-0.91	0.95	-0.59	0.92
Aug-17	-0.58	0.87	-0.68	1.25	**-0.61**	0.98
Sep-17	-0.52	0.79	-0.85	1.08	-0.49	0.84
Oct-17	-0.38	0.72	-0.45	0.94	-0.41	0.75
Nov-17	-0.49	0.60	-0.59	0.80	-0.51	0.64
Dec-17	-0.48	0.41	-0.58	0.40	-0.52	0.51
Jan-18	-0.51	0.68	-0.67	0.72	-0.47	0.70
Feb-18	-0.51	0.98	-0.64	1.06	-0.51	1.00
Mar-18	-0.43	1.04	-0.52	1.15	-0.47	1.11
Apr-18	-0.52	1.09	-0.66	**1.61**	-0.56	1.15
May-18	-0.62	1.09	**-1.07**	1.41	-0.53	**1.16**
Jun-18	-0.76	1.16	-0.63	1.56	-0.49	1.19
Jul-18	-0.92	**1.19**	-0.91	1.41	-0.63	1.10
Aug-18	-0.86	1.18	-0.91	1.54	-0.62	1.18
Sep-18	-0.95	1.19	-0.81	1.24	-0.50	0.89
Oct-18	-0.95	0.89	-0.54	0.90	-0.68	0.99
Nov-18	-0.81	0.95	-1.08	0.74	-0.91	0.67
Dec-18	-0.82	1.04	-0.57	0.63	-0.62	0.54
Jan-19	-0.61	0.92	-0.88	0.65	-0.62	0.47
Feb-19	-0.51	0.70	-0.71	0.84	-0.61	0.62
Mar-19	-0.44	1.04	-0.47	1.24	-0.45	1.12
Apr-19	-0.91	**1.19**	-0.71	1.45	-0.38	1.18
May-19	-0.62	1.16	-0.63	1.45	-0.57	1.16
Jun-19	-0.55	1.11	-0.83	2.22	-0.49	1.15
Jul-19	**-0.99**	1.12	-1.63	1.43	**-0.99**	**1.15**
Aug-19	-0.72	1.06	-1.06	1.41	-0.63	1.06
Sep-19	-0.51	0.76				

* Data collection for Cells 139 and 239 started on July 17th, 2017

Cells 705 and 805 are thin unbonded fiber reinforced concrete overlays on concrete pavement. Table 7 shows the monthly maximum and minimum LTGs for both Cells 705 and 805. Cell 705 had a maximum positive LTG of 1.00 °C/cm and a maximum negative of -0.74

°C/cm, while Cell 805 had a maximum positive LTG of 1.11 °C/cm and a maximum negative LTG of -0.90 °C/cm. For Cell 705, the maximum positive LTGs occurred in July 2018 and for Cell 239 the same occurred in April 2019. The maximum negative LTG for Cell 705 occurred in September 2017, and for Cell 805, it occurred in September 2018. Overall the maximums LTGs for Cell 805, which were constructed with 6 ft wide slabs, were slightly higher than Cell 705 that had 12 ft wide slabs.

Table 7. Linear temperature gradient results for Cells 705 and 805.

Temperature Gradient (°C/cm)				
	Cell 705 (5-inch)		Cell 805 (5-inch)	
Month	**Negative**	**Positive**	**Negative**	**Positive**
Sep-17	**-0.74**	0.53	-0.39	0.57
Oct-17	-0.35	0.41	-0.38	0.57
Nov-17	-0.40	0.35	-0.41	0.48
Dec-17	-0.45	0.19	-0.47	0.30
Jan-18	-0.48	0.44	-0.50	0.56
Feb-18	-0.44	0.53	-0.46	0.66
Mar-18	-0.37	0.64	-0.43	0.83
Apr-18	-0.39	0.74	-0.43	1.01
May-18	-0.35	0.81	-0.48	1.04
Jun-18	-0.38	0.77	-0.25	-0.24
Jul-18	-0.62	**1.00**	-0.70	1.08
Aug-18	-0.22	0.37	-0.67	1.05
Sep-18	-0.25	0.26	**-0.90**	1.02
Oct-18	-0.23	0.25	-0.82	0.64
Nov-18	-0.27	0.20	-0.88	0.58
Dec-18	-0.22	0.20	-0.88	0.61
Jan-19	-0.30	0.20	-0.57	0.40
Feb-19	-0.26	0.22	-0.53	0.80
Mar-19	-0.26	0.46	-0.46	0.93
Apr-19	-0.02	0.57	-0.76	**1.11**
May-19	-0.11	0.53	-0.45	1.10
Jun-19	-0.11	0.47	-0.39	0.97
Jul-19	-0.15	0.46	-0.60	0.98
Aug-19	-0.16	0.43	-0.44	0.92
Sep-19	-0.07	0.43	N/A	N/A
Oct-19	0.00	0.11	N/A	N/A

* Data collection for cell 805 started on September 5th 2017

Table 8. Linear temperature gradient results for Cell 606.

Temperature Gradient (°C/cm)				
	Cell 606 Inner (5-inch)		Cell 606 Outer (5-inch)	
Month	**Negative**	**Positive**	**Negative**	**Positive**
Jul-17	-0.38	0.74	-0.28	0.62
Aug-17	-0.50	0.74	-0.33	0.62
Sep-17	-0.37	0.64	-0.33	0.61
Oct-17	-0.34	0.55	-0.34	0.42
Nov-17	-0.43	0.52	-0.41	0.39
Dec-17	-0.47	0.33	-0.43	0.22
Jan-18	-0.49	0.61	-0.47	0.49
Feb-18	-0.47	0.72	-0.43	0.56
Mar-18	-0.47	0.91	-0.39	0.72
Apr-18	-0.47	1.06	-0.44	0.84
May-18	-0.53	1.12	-0.34	0.92
Jun-18	-0.40	1.04	-0.36	0.85
Jul-18	-0.40	0.99	-0.38	0.77
Aug-18	-0.35	0.93	-0.35	0.73
Sep-18	-0.48	0.71	-0.38	0.56
Oct-18	-0.39	0.68	-0.37	0.54
Nov-18	-0.47	0.55	-0.48	0.45
Dec-18	-0.43	0.54	-0.41	0.43
Jan-19	-0.56	0.56	**-0.55**	0.43
Feb-19	-0.47	0.61	-0.44	0.47
Mar-19	-0.46	0.98	-0.43	0.80
Apr-19	-0.33	**1.17**	-0.33	**0.97**
May-19	-0.45	**1.17**	-0.35	0.93
Jun-19	-0.41	1.04	-0.38	0.82
Jul-19	**-0.64**	1.03	-0.38	0.86
Aug-19	-0.45	0.99	-0.39	0.76

*Data collection started July 7th, 2017

Out of the four Cells 506 through 806 in the mainline test track, only Cell 606 has thermocouple trees. Two sensor trees were included in this cell. The LTGs for both sensor trees are provided in Table 8. For the inner sensor tree, the maximum positive LTG was 1.17 °C/cm, and the maximum negative TG was -0.64 °C/cm. The outer sensor tree has maximum positive and negative LTGs of 0.97 °C/cm and -0.55 °C/cm, respectively. For both outer and inner sensor trees, the positive maximum LTG occurred in May of 2018. The

maximum negative LTGs for the inner and outer sensor trees occurred in July 2019 and January 2019, respectively. Comparing the outer sensor tree, the inner sensor tree of Cell 606 shows slightly greater LTGs. Comparing all the cells, it was found that the maximum positive temperature gradients mostly occurred during the warmer temperatures.

3.2.1 Frequency Distribution of Linear Temperature Gradients

In order to determine the common LTG ranges, the frequency distributions of the LTGs were plotted for each cell, as shown in Figure 3-22. The LTG ranges and the corresponding frequencies were plotted in this figure. The frequency distributions of Cells 139 and 239 did not show a great difference. In Cell 239, the trends between the two sensor trees were similar with the exception that the outer sensor tree had a higher number of frequencies for an LTG range of -0.5 to -0.25 ^{o}C/cm than the inner one. The Cell 239 inner sensor tree and Cell 139 provided very similar LTGs. The maximum frequency for Cell 139 and the inner tree in Cell 239 occurred in the LTG range of -0.15 to 0 ^{o}C/cm. The maximum frequency for the outer sensor tree in Cell 239 occurred in the range of -0.5 and -0.25 ^{o}C/cm. Cell 705 and 805 have similar trends with the maximum for both cells occurring between -0.15 and 0 ^{o}C/cm. The trends of the LTGs measured at the inner and outer trees of Cell 606 were also the same with the maximum frequency occurring between -0.15 and 0 ^{o}C/cm.

Figure 3-23 shows the percent time that the LTG was positive and negative. Overall, the percent time that the LTG was positive or negative was consistent between the cells. It appeared that all the cells experienced negative temperature gradients for more than 60 percent time.

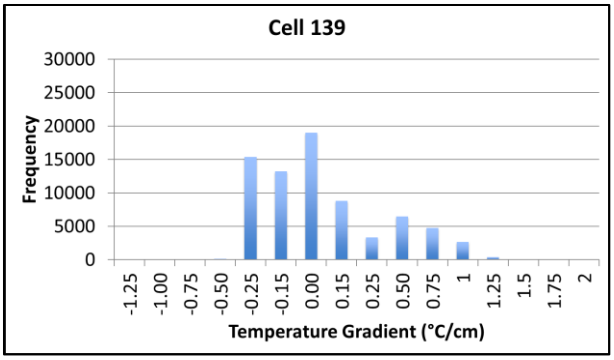

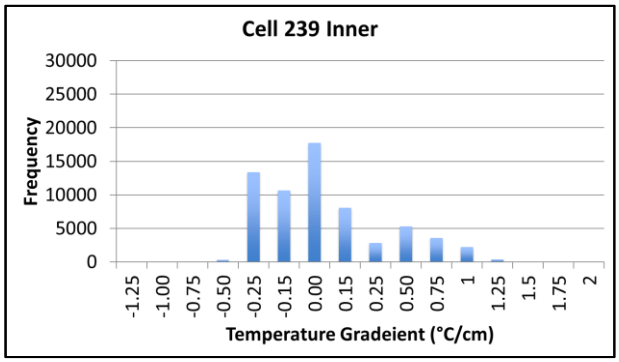

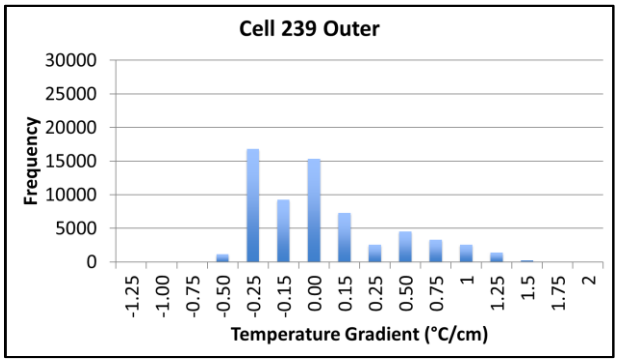

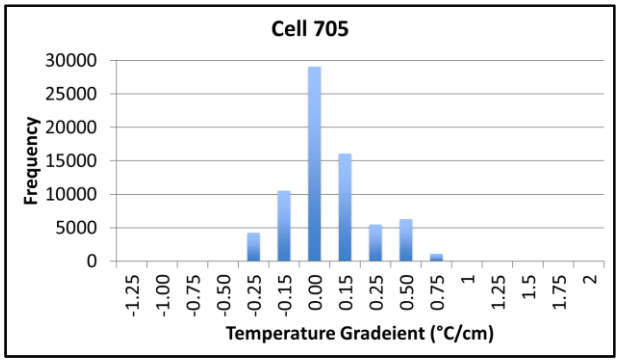

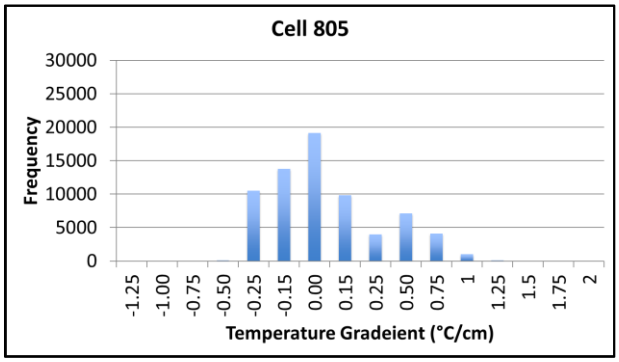

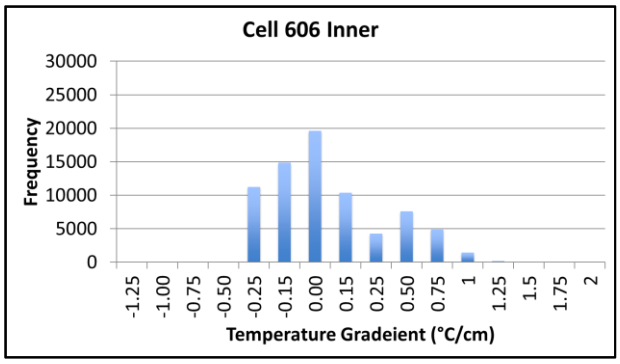

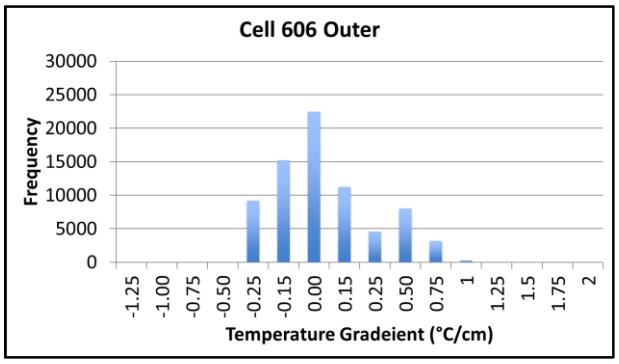

Figure 3-22. Frequency distributions of the linear temperature gradient for various cells.

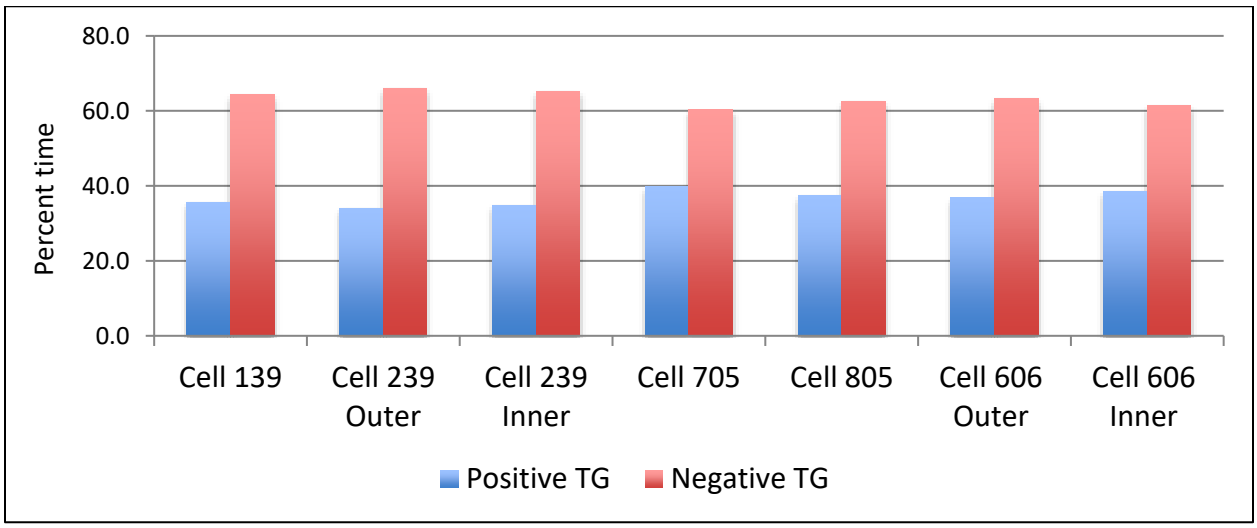

Figure 3-23. Percent times of positive and negative LTGs.

3.3 Environmental Strain

Vibrating wire sensors were installed in all of the MnDOT 2017 FRC research cells to measure the environmental strain that occurs in the slabs and to investigate the trends of this strain with respect to fiber dosage and pavement design features. A photograph of a vibrating sensor is shown in Figure 3-24. The raw data from this type of sensor are converted to estimate the environmental strain that is exerted on the concrete as a result of the change in the moisture state, temperature and temperature gradient, freezing of underlying layers, and joint locking. MnDOT has an established procedure for converting the raw vibrating wire data into a meaningful strain. One of the important steps in the vibrating wire data analysis procedure is to determine the initial strain value, which corresponds to the first reading when the concrete has hardened sufficiently to fully engage the sensor, and the temperature difference between the nearby top and bottom temperature sensors is approximately '0'. The initial strain value serves as the baseline value for subsequent readings. In order to determine the above-mentioned initial strain value, temperatures at the top and bottom of the slab and the raw frequency data are plotted together. An example of such plots is provided in Figure 3-25; these plots are related to one of the vibrating sensors of Cell 139 (Sensor 1, longitudinal direction). Using these plots, the time of the first 0-temperature gradient after the raw frequency data

started proper cycling is determined; the corresponding strain at this time is considered as the initial strain value. In Figure 3-25, it can be seen that the initial strain value was achieved around 8:30 AM of July 18, 2017 (approximately 11 hours after the paving) when the temperature gradient was nearly 0.

Figure 3-24. Photograph of a vibrating wire sensor.

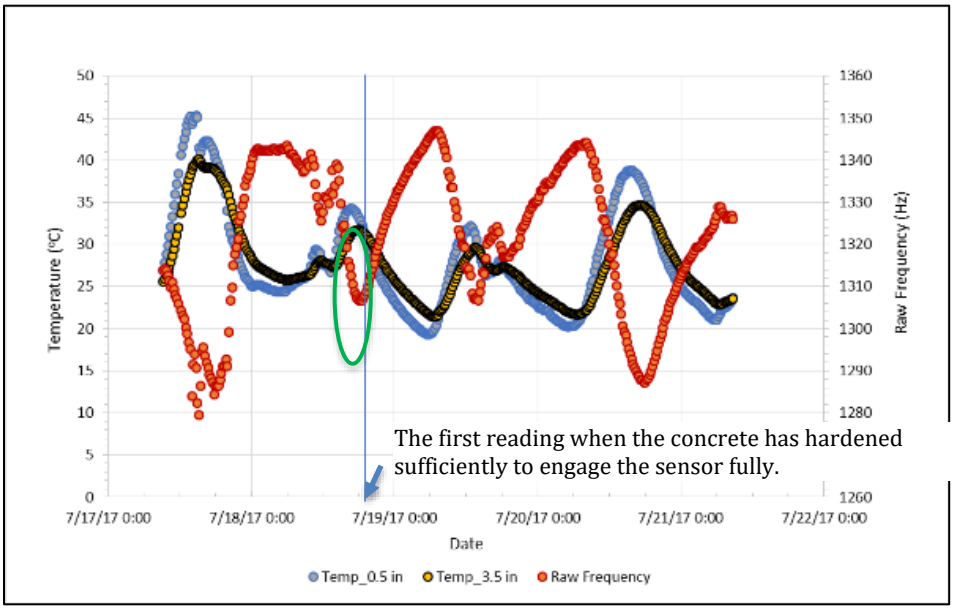

Figure 3-25. Temperature vs. raw frequency, Cell 139, Sensor 1.

3.3.1 Cells 139 and 239

In Cell 139, four vibrating wire sensors were installed, two in the longitudinal direction and two in transverse directions, all at the bottom of the slab, at a depth of 2.5 inches (a half-inch from the bottom of the concrete). Figure 3-26 shows the environmental strains measured by the four sensors. Three out of four sensors showed a similar trend while the fourth sensor, which was in the transverse direction, shown a completely different and higher negative (tensile) strain compared to the other three. The less variation between the two sensors in the transverse direction and one longitudinal direction may be attributed to the small panel size and somewhat similar boundary conditions along three sides of each slab.

Nevertheless, all the sensors have provided negative strains, indicating that slabs were in a state of contraction. A close look at all these plots indicates that the negative strains in all the sensors sharply increased from July 18, 2017, until the mid of August 2017. Although the temperature declined during this period, the drying shrinkage could have played an influencing role. After that, the strains in all the sensors followed the temperature variation, recording higher tensile strains during the winter, and lower tensile strains at warm temperatures.

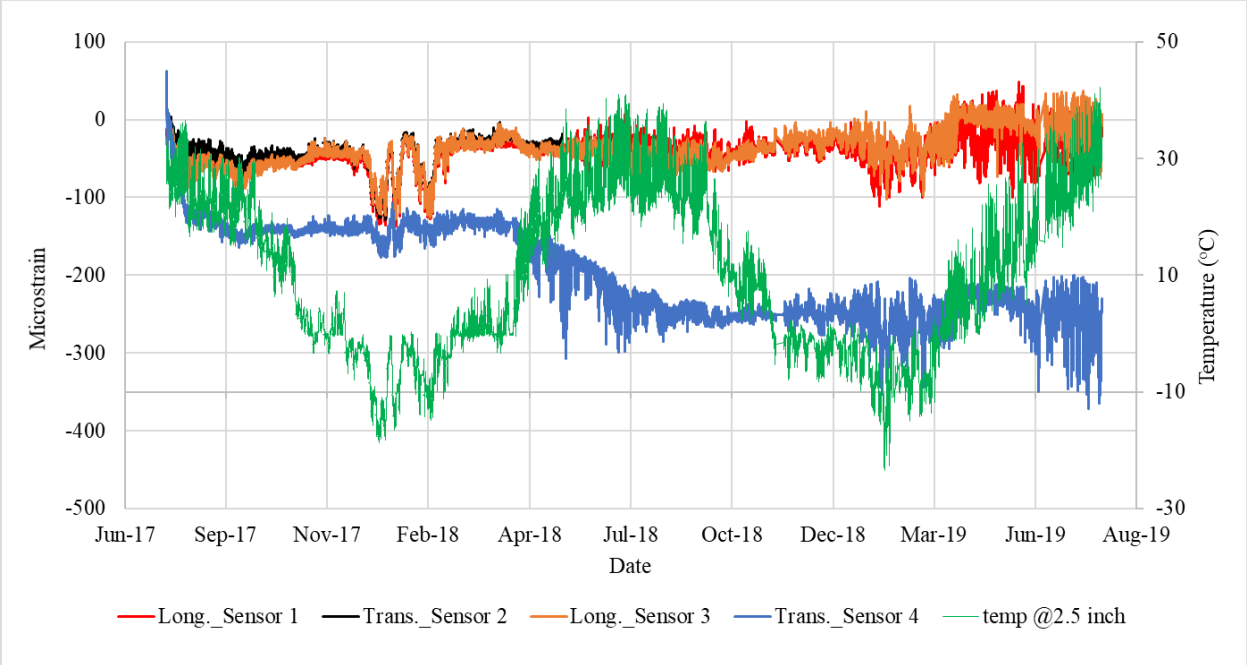

Figure 3-26. Environmental strains and slab temperature for Cell 139.

Figure 3-27 shows plots for the environmental strains and temperature at the 3.5-inch depth of the slab for Cell 239. Similar to Cell 139, vibrating wire sensors were installed only at the bottom of the slab because of the thickness limitation. As can be seen in Figure 3-27, the strains varied with the seasonal temperature and also experienced a sharp increase in negative strain until the mid of August 2017. The strain measured during the winter was relatively high, in general. Sensor 7, which was placed along the longitudinal direction shown a higher amount of strains than the other three sensors in the cell. The overall trend of the strains measured in Cell 239 was similar to what was observed in the Sensor 4 of Cell 139, indicating an increase in the strain values with the age of the pavement. Compared to the sensors in the transverse directions, the sensors in the longitudinal direction experienced greater strains. The difference in magnitude of the environmental strains in both Cells 139 and 239 was not large.

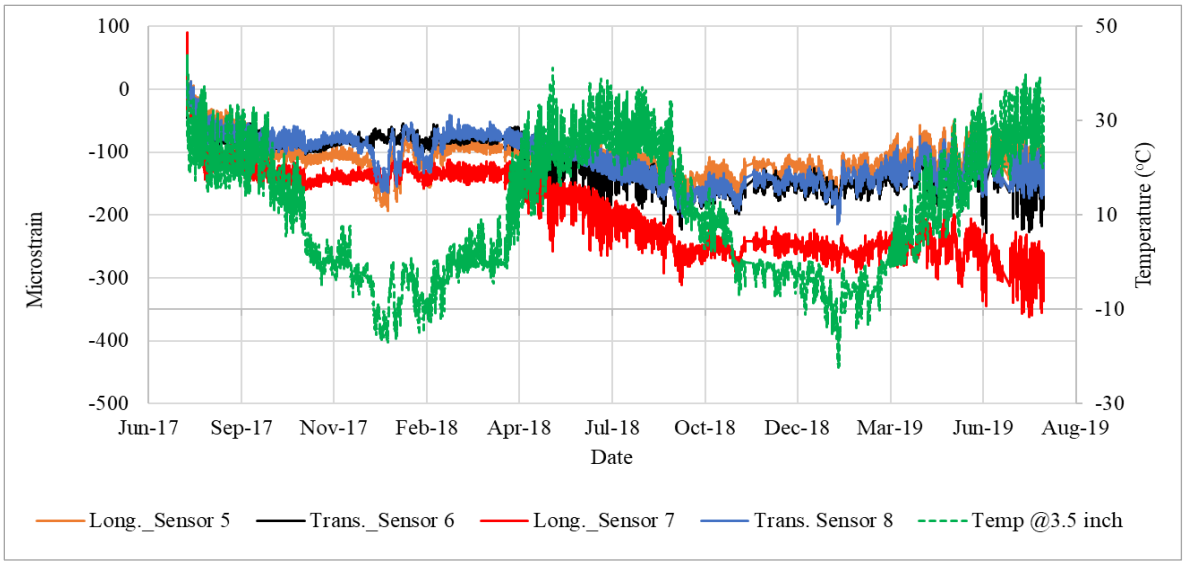

Figure 3-27. Environmental strains and slab temperature for Cell 239.

3.3.2 Cells 705 and 805

In Cell 705, eight vibrating wire sensors were installed in two slabs, four in each slab. In each slab, sensors were installed in the longitudinal and transverse directions. The longitudinal sensors were located at the center of the slab, and the transverse sensors were adjacent to the transverse joints, as shown in Figure 3-3. Two sensors were installed at each location, one at the top and other at the bottom of the slab, one-half-inch inside the concrete. Figure 3-28 and Figure 3-29 show the strains measured in the first slab and second slabs, respectively. Like the other two cells discussed above, the sensors in this cell also shown a correlation with the seasonal temperature. In the first slab, it appeared that the sensors placed at the top of the slabs experienced more strains irrespective of their location with all the sensors recording higher negative strain values in the cold temperatures. Two sensors (6 and 7) in the second slab recorded higher tensile strain compared to all other six sensors in this cell. Sensor 6, which was placed at the bottom of the slab along the longitudinal direction, recorded high tensile strain from the early age, whereas Sensor 7 picked up the high strain since summer 2018. The strain measured in the 2018 - 2019 winter ranges from 350 to 450 microstrain.

Similar to Cell 705, a total of eight vibrating wire sensors were installed in Cell 805. All the sensors were installed at the center of the slabs, both near the top and bottom of the slab, a half-inch inside the concrete. This report included the results of three sensors installed in the first slab. The results of the three sensors in Cell 805 also showed a great correlation with the seasonal temperature variation. Sensor 1, which was placed in the transverse direction, recorded the highest strain, around 300 to 375 microstrain during the winter.

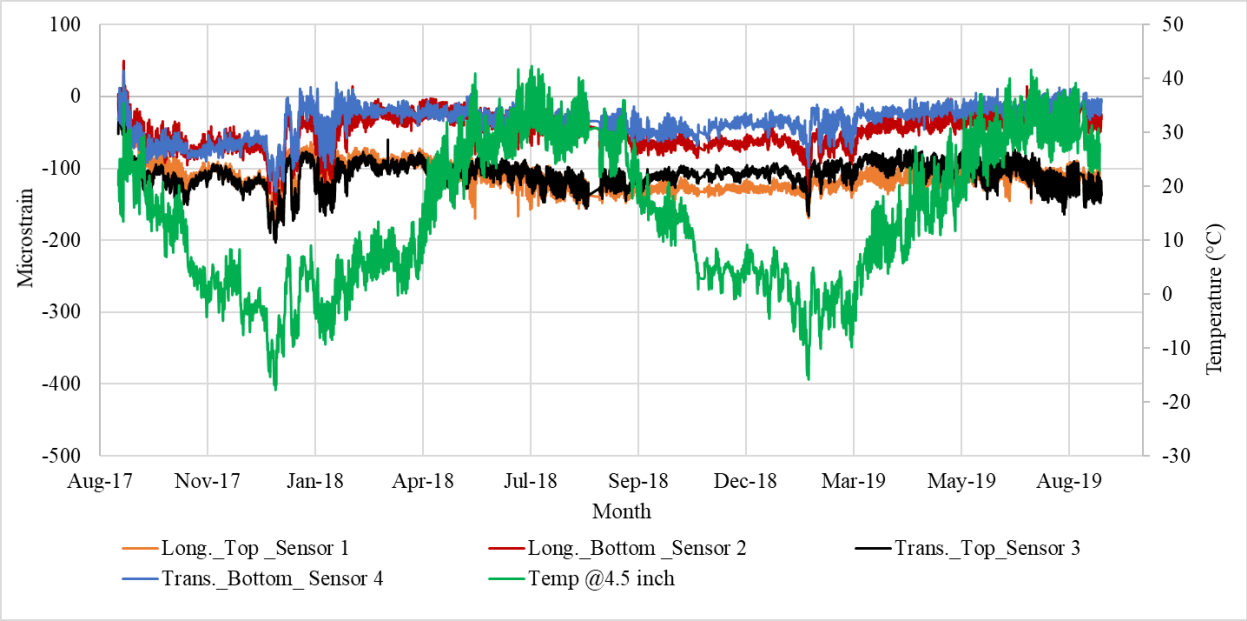

Figure 3-28. Environmental strains and slab temperature for Cell 705, first slab.

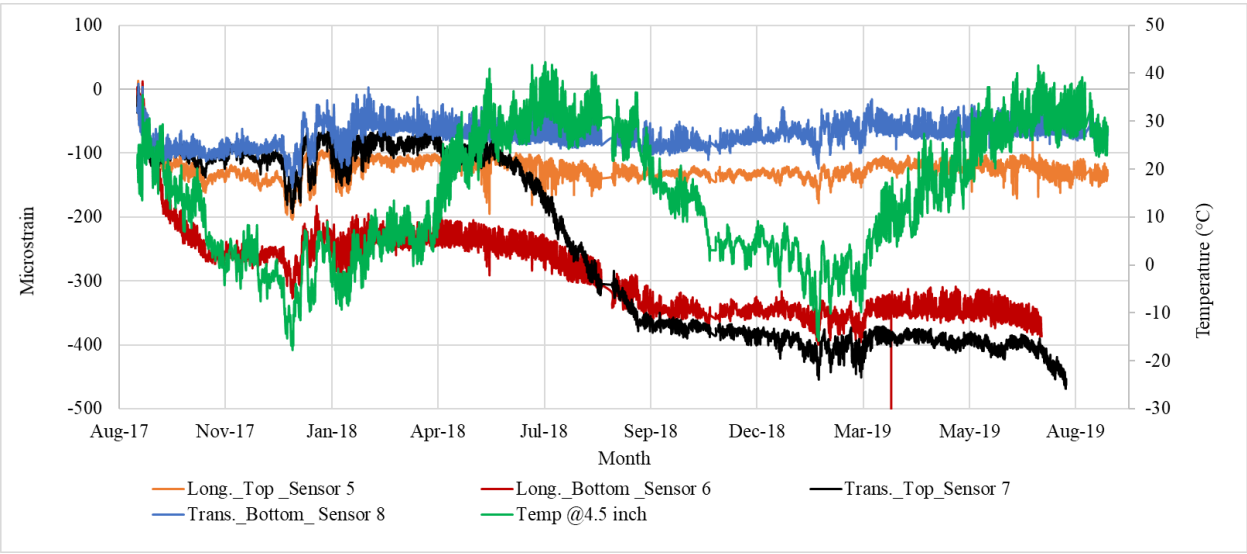

Figure 3-29. Environmental strains and slab temperature for Cell 705, second slab.

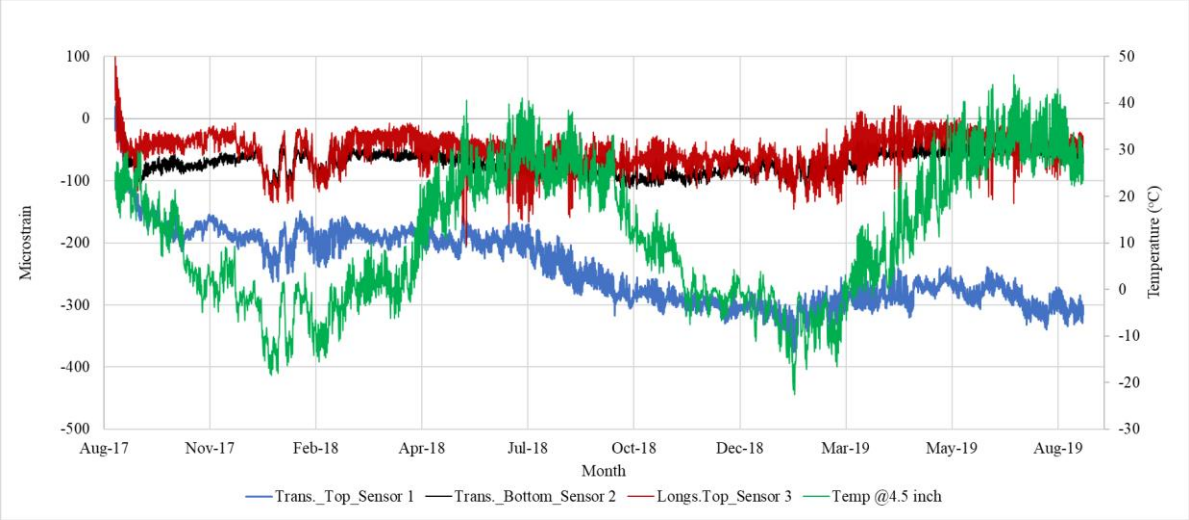

Figure 3-30. Environmental strains and slab temperature for Cell 805, first slab.

3.3.3 Cells 506 through 806

For these cells, some vibrating wire data for the first couple of weeks were not available. As previously mentioned, the vibrating wire and temperature data for the initial period are used to zero out the subsequent strain values. The vibration wire and temperature data for other cells were thereby studied, and their trends were used to populate the initial strain values for these cells. Figure 3-31through Figure 3-34 show the environmental strains calculated for these cells. Each of these cells has four sensors, two in the transverse direction in one slab and the other two in the longitudinal direction in another slab. The strains measured in all of these cells are relatively low compared to the other four cells discussed above. The strain values have shown a correlation with the slab temperature and values were high during the winter months as anticipated.

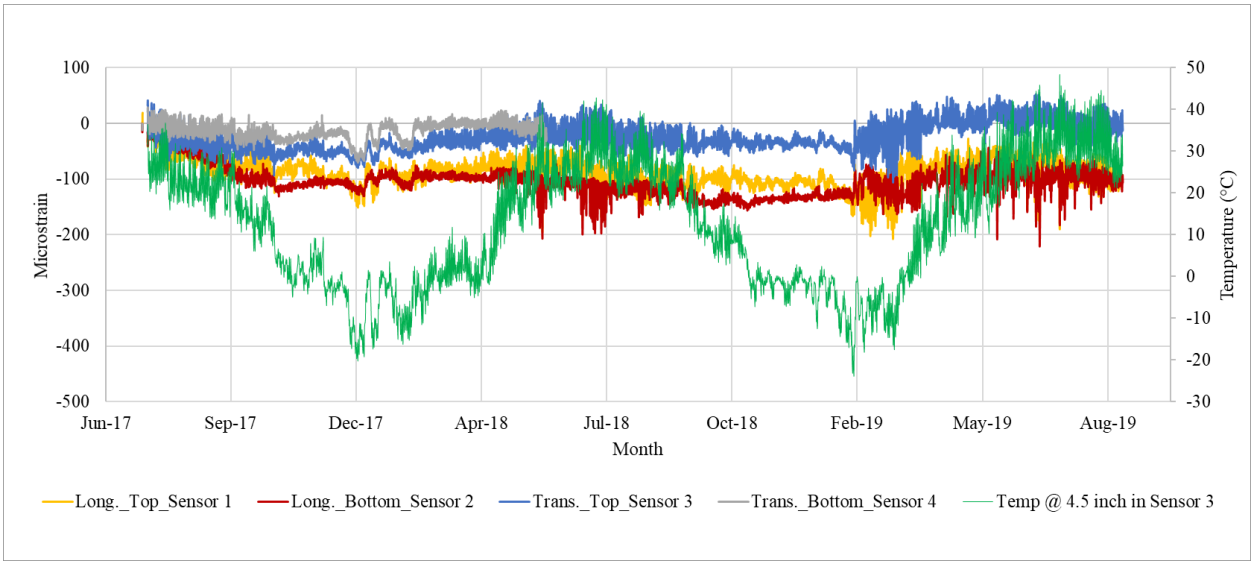

Figure 3-31. Environmental strains and slab temperature for Cell 506.

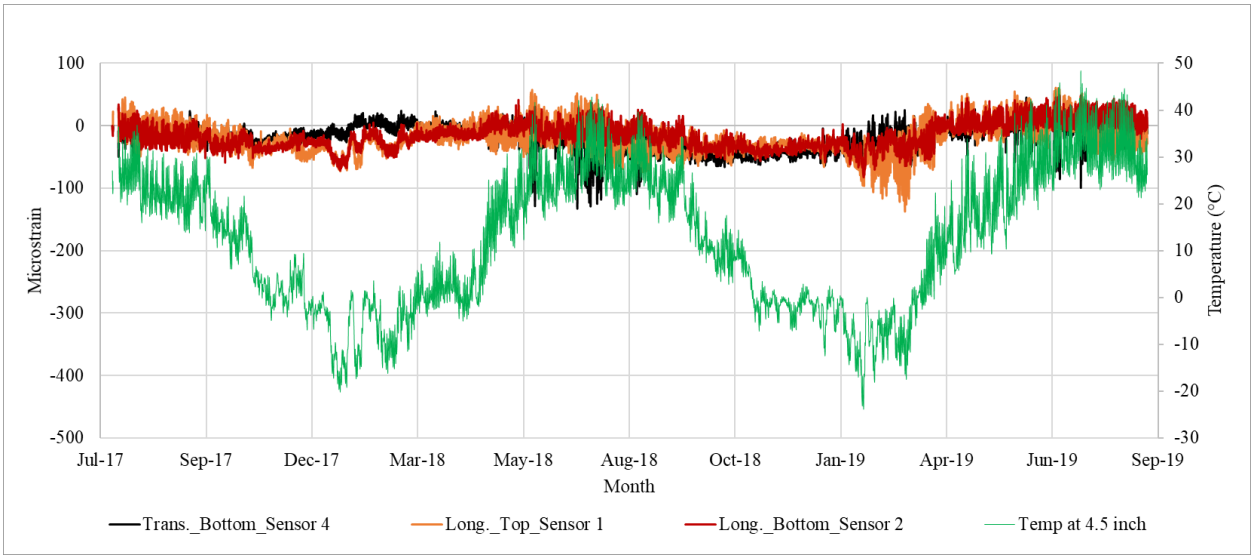

Figure 3-32. Environmental strains and slab temperature for Cell 606.

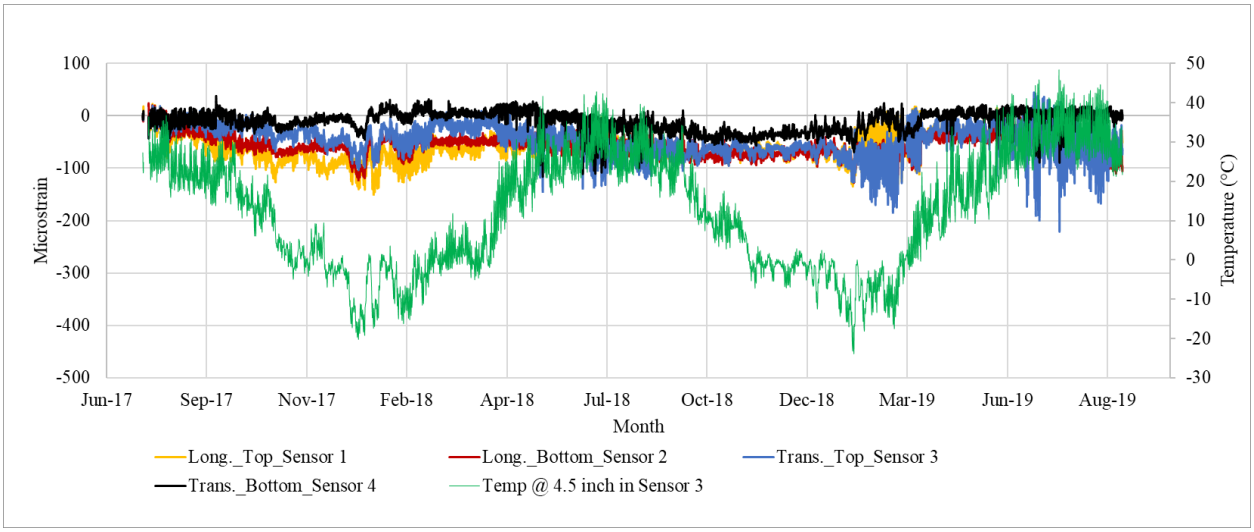

Figure 3-33. Environmental strains and slab temperature for Cell 706.

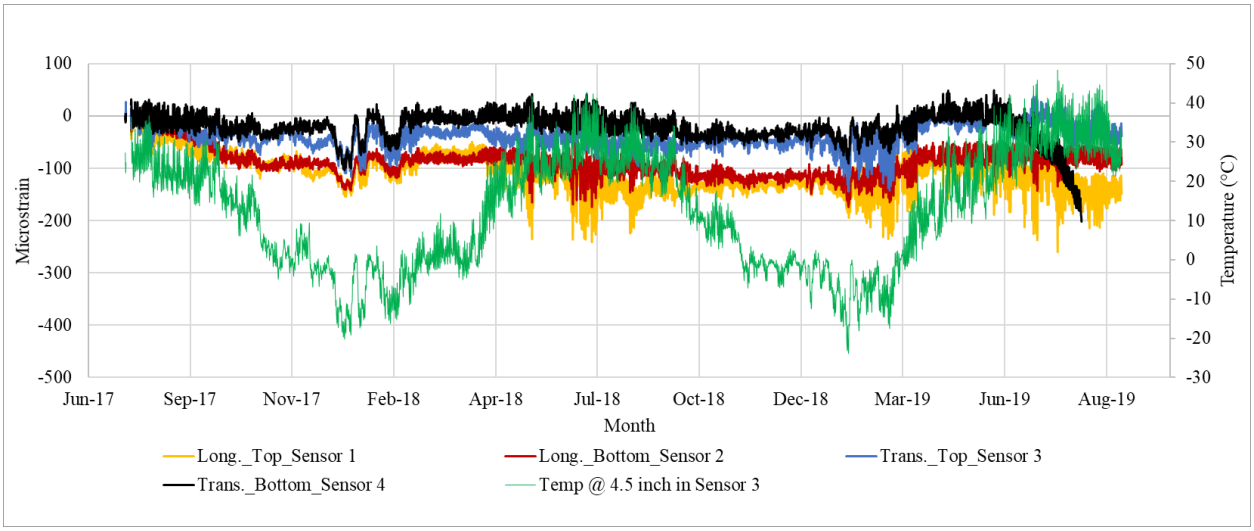

Figure 3-34. Environmental strains and slab temperature for Cell 806.

In summary, it can be stated that the strain recorded by almost all of the sensors were influenced by the seasonal temperature; strains were high during the winter and low in summer. Some sensors also have shown increasing strains with the age of the pavement, probably because of the fatiguing of the slabs and damage accumulation in the overall structure. Strains in ultra-thin (3-and 4-inch thick) concrete pavements were relatively higher than the thin concrete pavements (Cells 506-806), may be because of more curling

and warping effect. The difference in the strains between the sensors placed either in the transverse or longitudinal directions and the top and bottom of the slabs could not be clearly established from the data analyzed. A distinct influence of the fibers has not been observed from the data and the analysis presented in this report.

3.4 Dynamic Strain

Dynamic strain sensors record the dynamic strain in the slab when a vehicle, MnDOT's five-axle truck, in this case, passes over them. As the tire offset (distance of the wheel from the sensor) affect the readings, MnDOT's truck was run multiple times for each date of data collection. The raw data collected from the sensors are processed, and peaks, valleys, and baseline (Figure 3-35) are determined using the MnDOT's Peak-Pick Program (Burnham and Tewfik, 2007) for each run. Figure 3-35 is an example of the plots with the peaks and valleys noted. As the truck has five axles, each sensor documents five peaks and five valleys. MnDOT has provided such plots and excel spreadsheets with the values of peaks, baseline and valleys to the research team. These plots and excels spreadsheets were used to determine the strain experienced by each sensor under each of the five axles loads. The difference between the peaks and baseline is considered as the strain. The maximum of five strain values from all the runs are compared with each other and the greatest value of them is reported as the dynamic strain for the sensor in question for a specific test date.

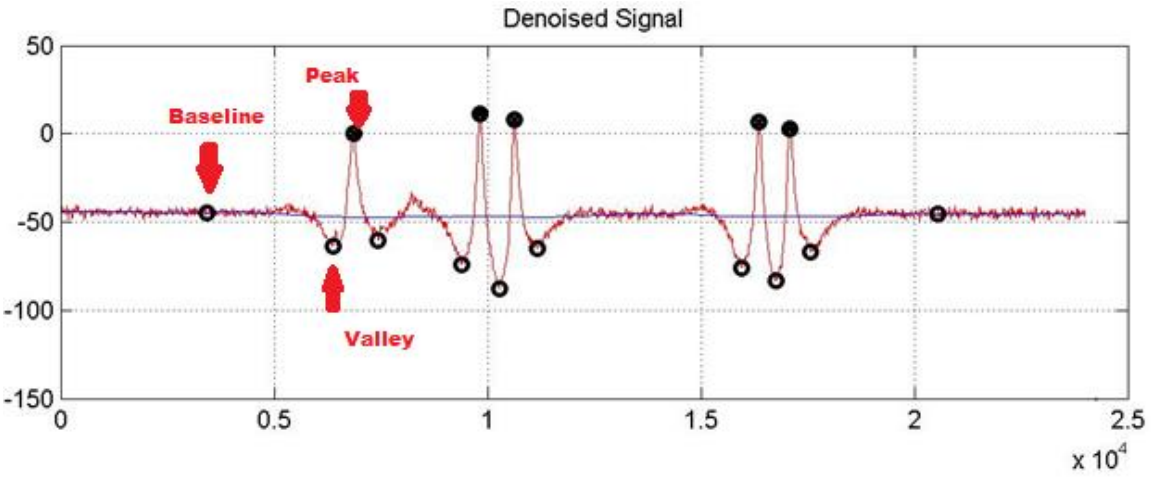

Figure 3-35. An example of a plot of strain due to the dynamic load exerted by the MnDOT truck.

Figure 3-36 shows the dynamic strains recorded by the sensors in longitudinal and transverse directions for Cells 139 and 239. Some strain values are missing at multiple dates because of the malfunction of some sensors. Overall, the magnitude of the strains in Cell 139 was higher than that was recorded in Cell 239. One sensor in Cell 139, placed in the longitudinal direction shown that the magnitude of the strain increased with time, other sensors did not show any trend. Figure 3-37 shows the comparison of dynamic strains between Cells 705 and 805. Compared to Cells 139 and 239, Cells 705 and 805 experienced far lower strains. The strains recorded in the Cell 705 and 805 did not show a significant difference, with slightly higher strain recorded for Cell 705 for some dates.

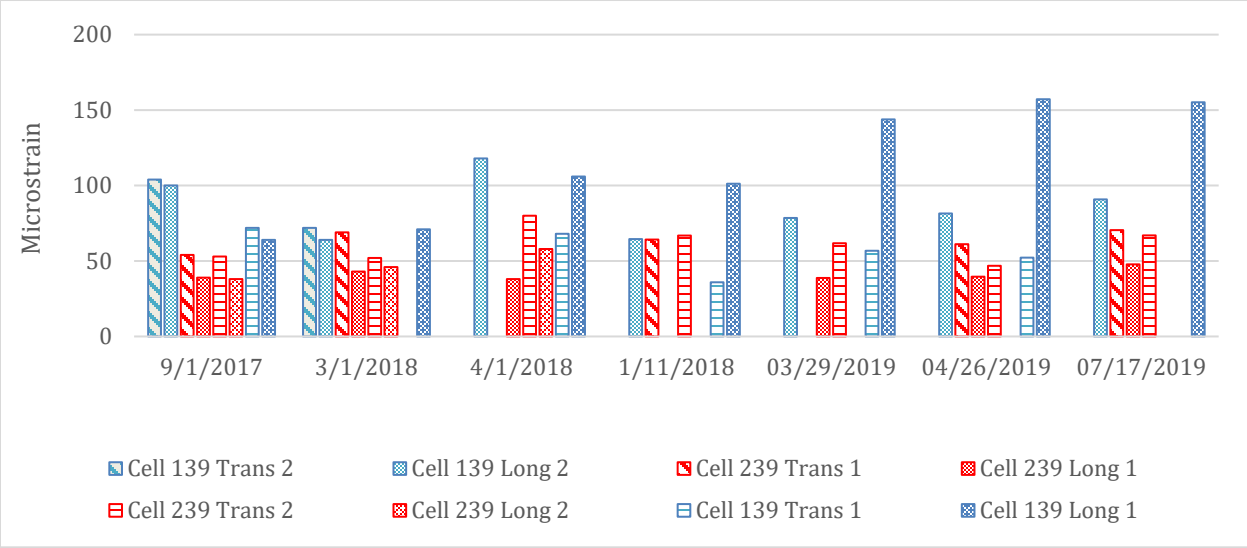

Figure 3-36. Dynamic strains recorded in Cells 139 and 239.

Cells 506, 606, 706, and 806 are the cells that compare the performance for different dosages of fibers. Dynamic sensors in these cells were laid along with the transverse directions only. The magnitudes of the dynamic strains in these cells are comparable. Some sensors in Cells 706 and 806 shown slightly higher strains in springs (April 2018, 2019), when the base and subgrade support were possibly the weakest.

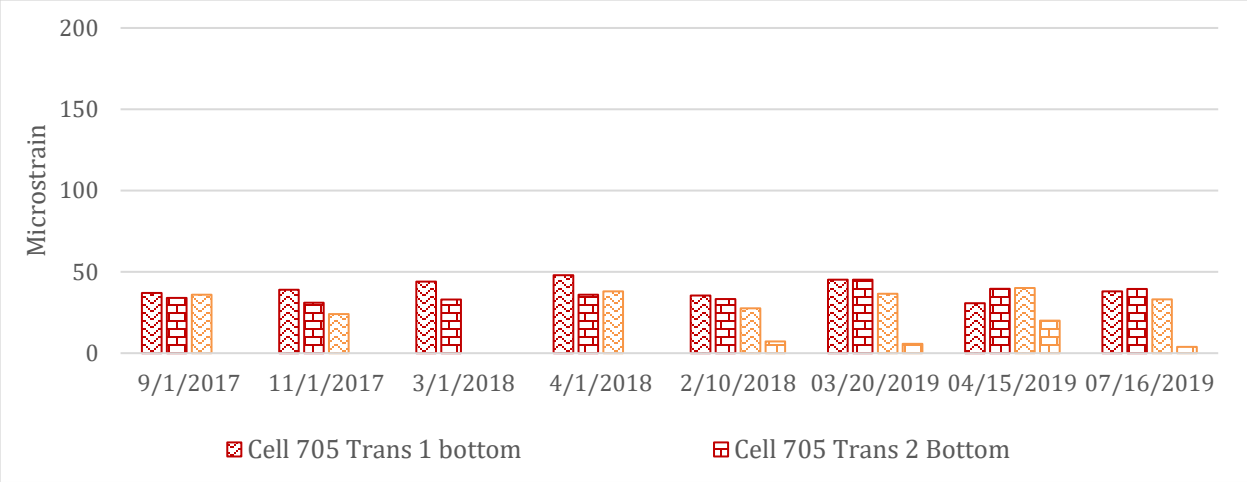

Figure 3-37. Dynamic strains recorded in Cells 705 and 805.

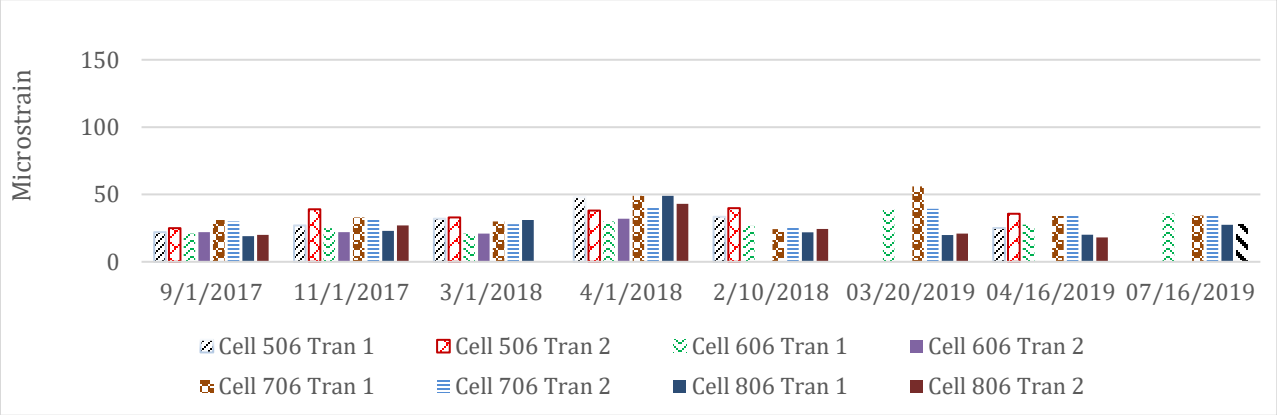

Figure 3-38. Dynamic strains recorded in Cells 506 through 806.

3.5 Joint Movement

A new type of joint opening sensor (spring-loaded potentiometer) was installed in MnROAD 2017 FRC research cells. A sketch and two photographs of such a joint opening sensor are provided in Figure 3-39. The goal of using this type of sensor is to track joint movement constantly throughout the year rather than manually measuring at certain time intervals. Figure 3-40 shows a plot of relative joint opening recorded by a joint opening sensor in Cell 506. The first joint opening reading was used to zero the subsequent joint opening readings. In this figure, it can be seen that there are two jumps in joint movement data, one in August of 2017 and the other one was in around October of 2017. The first

jump in Figure 3-41 is assumed to be related to the joint deployment. When the joints deploy, the sensor readings are supposed to show a jump. Some sensors didn't record any jump. The reason for this is either the deployment occurred before collecting the initial reading, the jump was not recognizable because of a minimal crack width change, or joint did not deploy at all. The second jump is related to the reinstallation of the sensor.

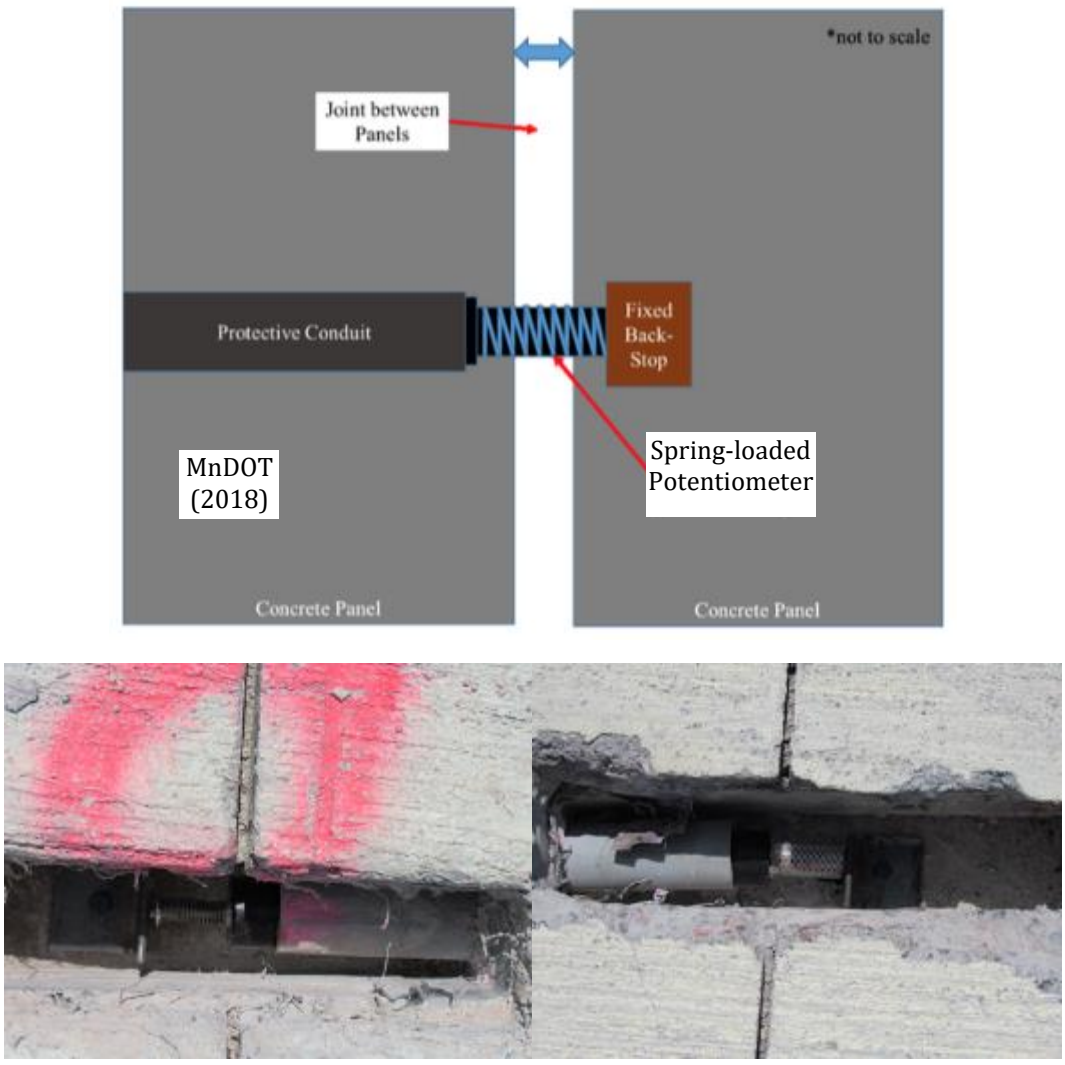

Figure 3-39. Sketch and photographs of joint opening sensors before installation of protective covering.

The majority of the joint opening sensors had to be re-installed after their first installation; protection for the sensor was applied during the reinstallation time. For the sensors that were reinstalled, data were adjusted to neutralize the re-installation related jump (Figure 3-41). For the sensor data presented in Figure 3-41, it can also be seen that some

erroneous data was recorded for some duration between September 2018 through January 2019. Figure 3-42 provides an example of joint movement readings collected by Sensor 3 of Cell 706; in this case, the joint in question probably did deploy before the collection of the first reading. This plot provides a good example of a relative joint opening with respect to the first reading. It can be seen that the joint opening was maximum during the winter months, after which the joint opening reduced with the temperature increase. Some sensor readings were discarded because of erroneous data, where the crack opening readings fluctuated significantly.

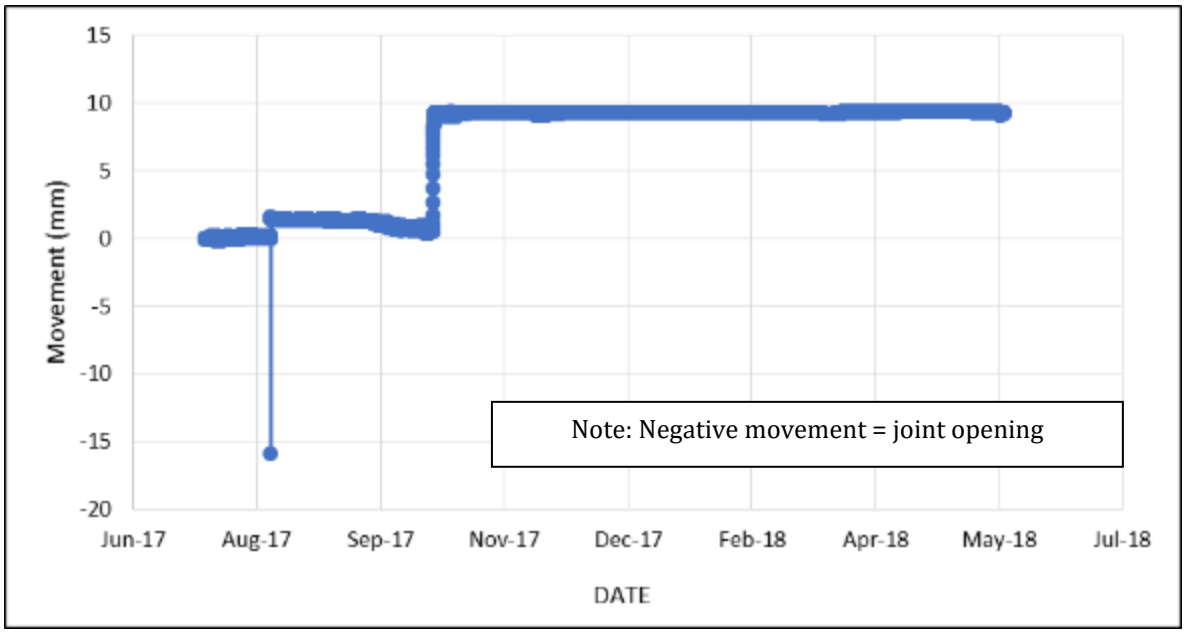

Figure 3-40. Joint movement recorded by Sensor 1 of Cell 506, before adjustment for re-installation was made.

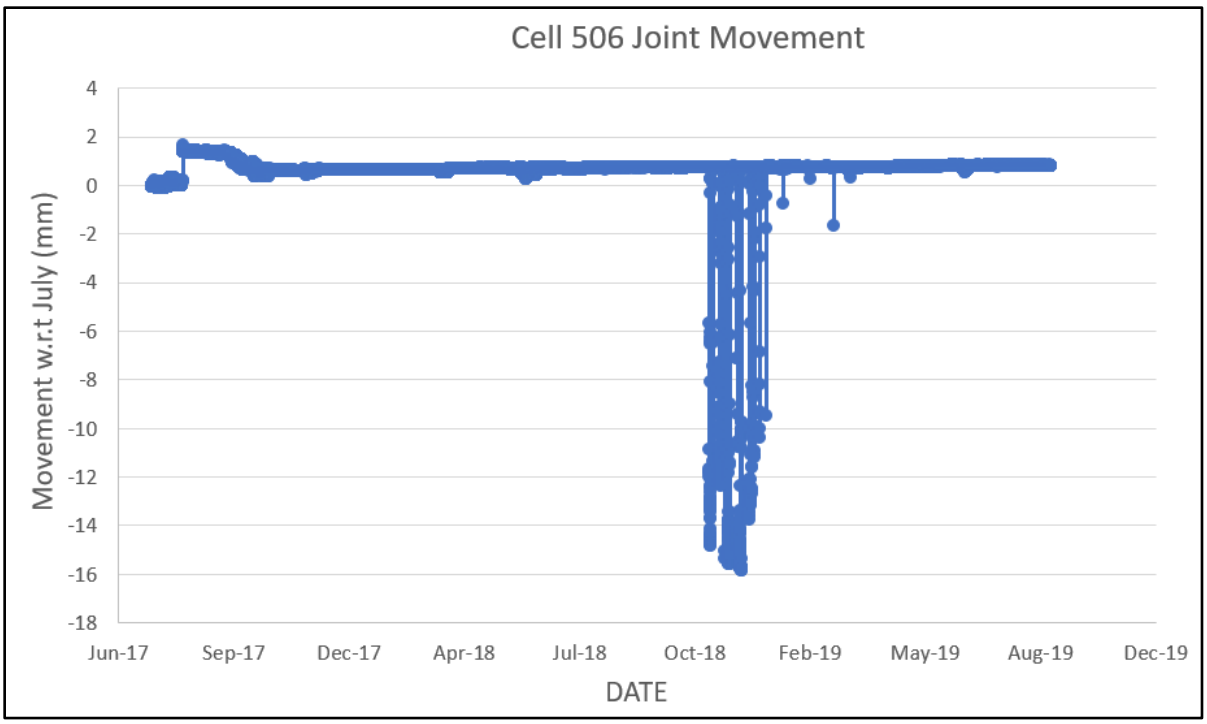

Figure 3-41. Joint movement recorded by Sensor 1 of Cell 506, after adjustment for re-installation was made. (Note- diff. scale in the y-axis)

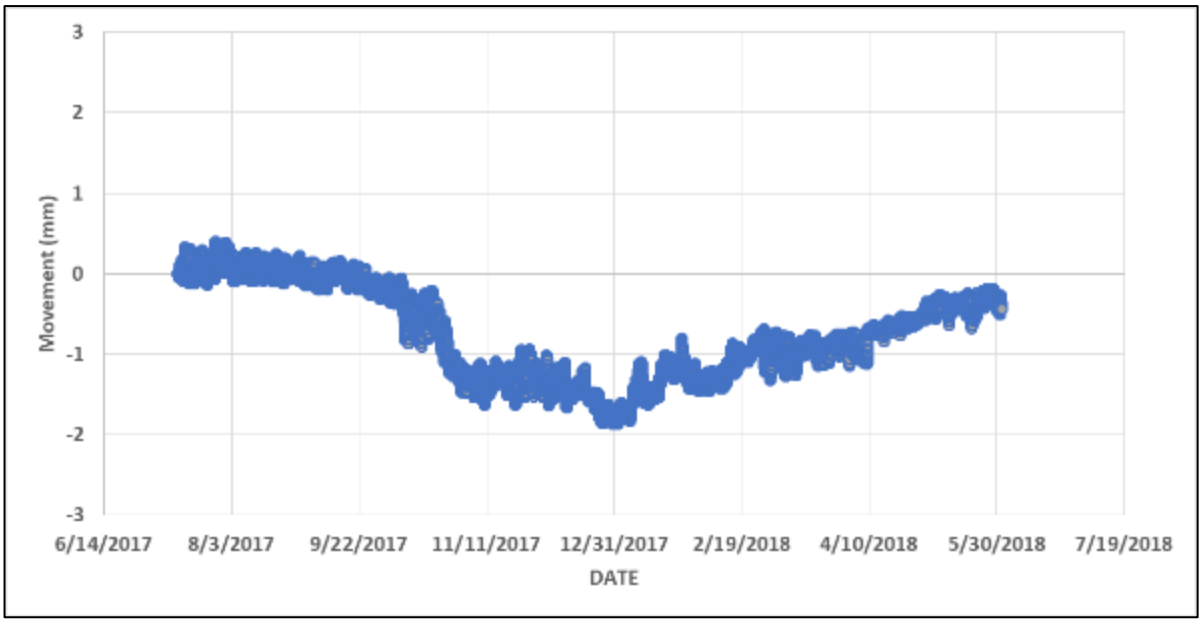

Figure 3-42. Movement recorded by Sensor 3 of Cell 706, no adjustment was required. (Note diff. scale in y-axis)

Table 9. Approximate maximum joint movement for different cells.

Max opening (approx.), mm	
Cell 139	12
Cell 239	NA
Cell 705	24
Cell 805	15
Cell 506	2
Cell 606	15
Cell 706	10
Cell 806	15

Appendix B includes joint movement plots for all the cells and Table 9 provides a summary of the approximate maximum joint movement observed for each of the cells. Because of the considerable variations in the data quality in some sensors, very convincing trends could not be achieved for all the cells, but the results of many sensors are reasonable. In order to investigate the seasonal variation of joint opening, the monthly average relative joint opening was calculated for each cell and plotted in Figure 3-43 and Figure 3-44. The averages for Cells 705 and 805 were zeroed with respect to September 2017, and all the other cells were zeroed with respect to July 2017. Cells 705 and 805 were zeroed using the later month because they were constructed later than the other cells. Note that the Y-axis scale of the plots for Cells 705 and 805 are different than the scale used for Cells 139 and 239 in Figure 3-43. In Cell 139, two sensors did not show a great variation in the joint opening, but the Sensor 1 showed that the joint opening increased during the winter months compared to the first reading taken in July 2017. Based on the data, the joints of the Cell 239 (at least where the sensors were installed) remained relatively dormant for most of the year with slight expansion recorded by Sensor 3 in the winter months. Cells 705 and 805 had experienced the largest joint opening movement among all the eight cells. While a few sensors installed in these two cells remained dormant, others showed significant movements and did not show a meaningful correlation with seasonal temperature change. The cells are unbonded concrete overlays and have unwoven geotextile at the interface which might have influenced the slab movements. It may happen that some slabs are being migrated with the traffic load.

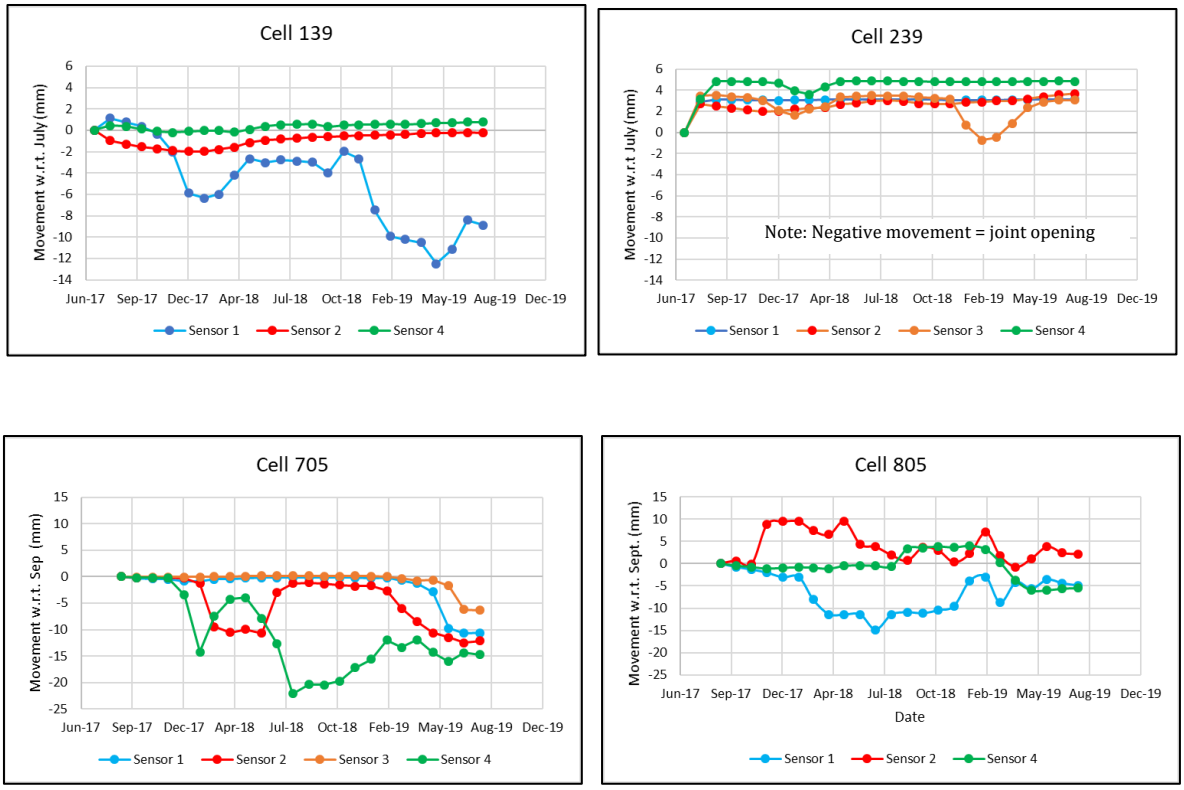

Figure 3-43. Monthly average relative joint movement for Cells 139, 239, 705 and 805.

For Cells 506 through 806, there is a concern in the accuracy of the sensors in Cell 506. This cell does not contain fibers, and it was anticipated that larger joint openings would be observed in this cell compared to its counterparts (Cells 606 to 806). Cell 606 which contained 5lb/ cy fibers, did experience much joint opening during the winter months. Two sensors in this cell indicate that the joints did not close in summer once they opened in the first winter. Comparing with Cells 506 and 706, Cell 806 showed less joint openings until October 2018, after which one of the two sensors recorded some joint movements.

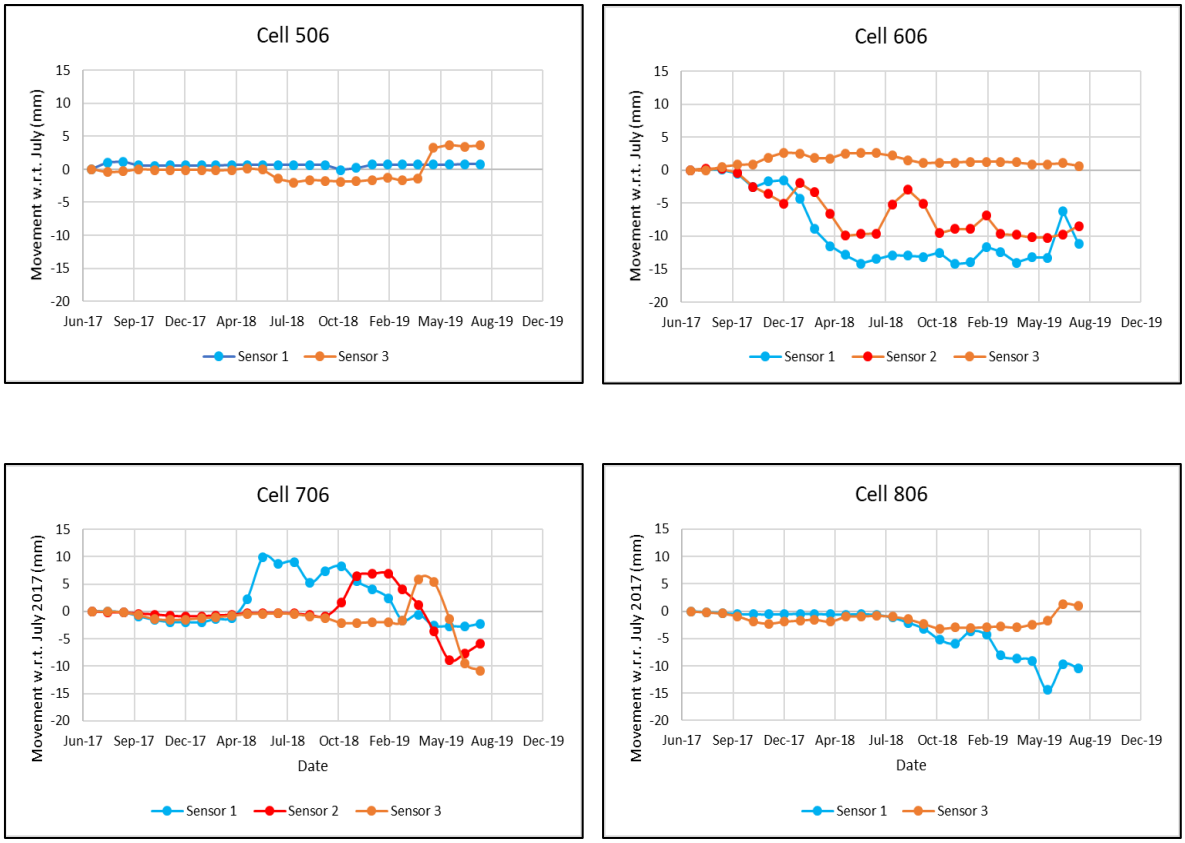

Figure 3-44. Monthly average relative joint movement for Cells 506 through 806.

4 JOINT PERFORMANCE

This section discusses the joint performance data. The results of the falling weight deflectometer (FWD) test conducted at selected transverse joints were used to determine the load transfer efficiency (LTE), differential displacement, and loaded-side displacement. The LTE is the ratio of the deflections at the unloaded side to the loaded side and expressed as a percentage. The differential displacement is the arithmetic difference between the loaded-side deflection and unloaded-side deflection.

4.1 LTE

Figure 4-1 shows the LTE of Cells 139, 239, 705 and 805. The LTE data of the Cells 139 and 239 were comparable when the first test was conducted on September 6, 2017and it ranged between 85 and 94%. The LTE of these two cells then continued to drop with the traffic load. The outside lane of both the cells, where traffic load is not applied, shown consistent higher LTE values than the inner lane, even though the Cell 139 experienced some LTE drops with age.

The wide joint opening of Cells 705 and 805, as discussed in Section 3.6, appeared to have influenced the LTE significantly. Contrary to the low faulting results, these two cells exhibited surprisingly very low LTE, at least in the joints considered in FWD testing.. Based on the joint opening sensor data, some of the cracks were wider than 10mm. The LTE of concrete pavement at such wide joint opening is usually very low. The FWD test conducted during the April 2019 however shown some increase in the LTE in the driving lane of these two cells. The exact reason for this increase is not known; however, upon investigating the joint movement data, it was found that one joint movement sensor (Sensor 3) of Cell 506 (Figure 3-44) detected significant joint contraction (~5mm) during April 2019. It might happen that the thawed water in the spring swollen slabs leading to joint contraction. The co-authors of this report, Mr. Tom Burnham, mentioned observing such joint contraction during spring at much lower at temperatures than the recommended FWD testing cutoff limit of 75^{o}F in the summer.

Figure 4-1. LTE of Cells 139, 239, 705 and 805.

The LTE results of Cells 506 through 806, shown in Figure 4-2, clearly reveals the contribution of structural fibers in keeping the LTE high. For Cell 506, even though the FWD test conducted on the driving lane in September 2017 showed a range of LTEs between 75 and 85%, the LTE afterwards significantly decreased overall. Surprisingly, the FWD tests conducted during the April 2019, shown relatively higher LTE at all the three joints considered. The reason for this may be similar to what happened in the Cells 705 and 805. The LTE in the passing lane of Cell 506 was always low, with a maximum of around 50%.

The LTE results of Cell 606, which is 6-inch thick, were at or above 90% when measured in September 2017, except one joint in the passing lane which always did show a low LTE (around 25 to 50%). The LTE for this cell had dropped significantly over the time.

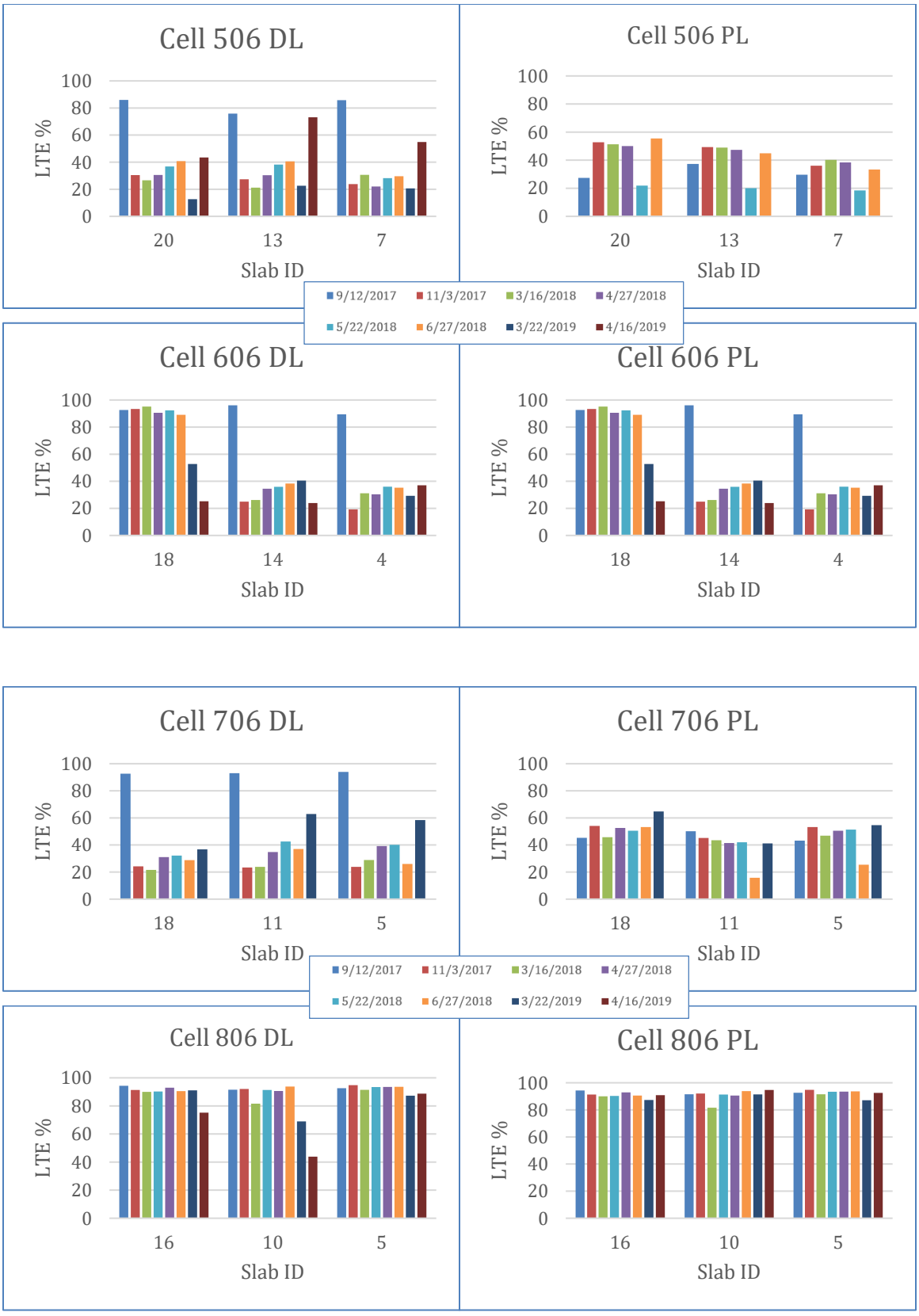

Figure 4-2. LTE of Cells 506, 606, 706 and 806.

The LTE of Cell 706, which is 5-inch thick and contains 8 lb/cy fibers, was initially high at three joints (at the driving lane) out of total of six joints measured. However, when measured at later dates, these joints exhibited 40 to 56% LTE.

Cell 806, which is 5-inch thick and contains 11.7 lb/cy of fibers, consistently exhibited the highest LTE among all the cells. Notably, all the joints were able to maintain a very good LTE between 88 to 94% throughout the first two years of service life. The higher LTE of this cell definitely helped in keeping the faulting to the lowest among all the eight cells.

4.2 Differential Displacement

Figure 4-3 and Figure 4-4 shows the plots for differential displacements for all the cells. The general trend of the differential displacement is similar to the trends observed for the LTE. The differential displacements for both Cells 139 and 239 continously increased with the traffic load. The FWD test result for the Joint 23 of cell 139 resulted in a very high value of differential displacement.

Cells 705 and 805 both have experienced high differential displacements at the transverse joints; the differential displacements of Cell 705 (~1000 micron) was almost twice of the Cell 805 (~460 microns). Even though the differential displacements was relatively high, the fabric interlayer provided in these cells is expected to limit the faulting. The contribution of fibers in joint performance can also be seen in the differential displacement plots for Cell 506 through 806. Cells 506, 606 and 706 exhibited significantly higher differential displacements than Cell 806.

Figure 4-3. Differential displacement of Cells 139, 239, 705 and 805.

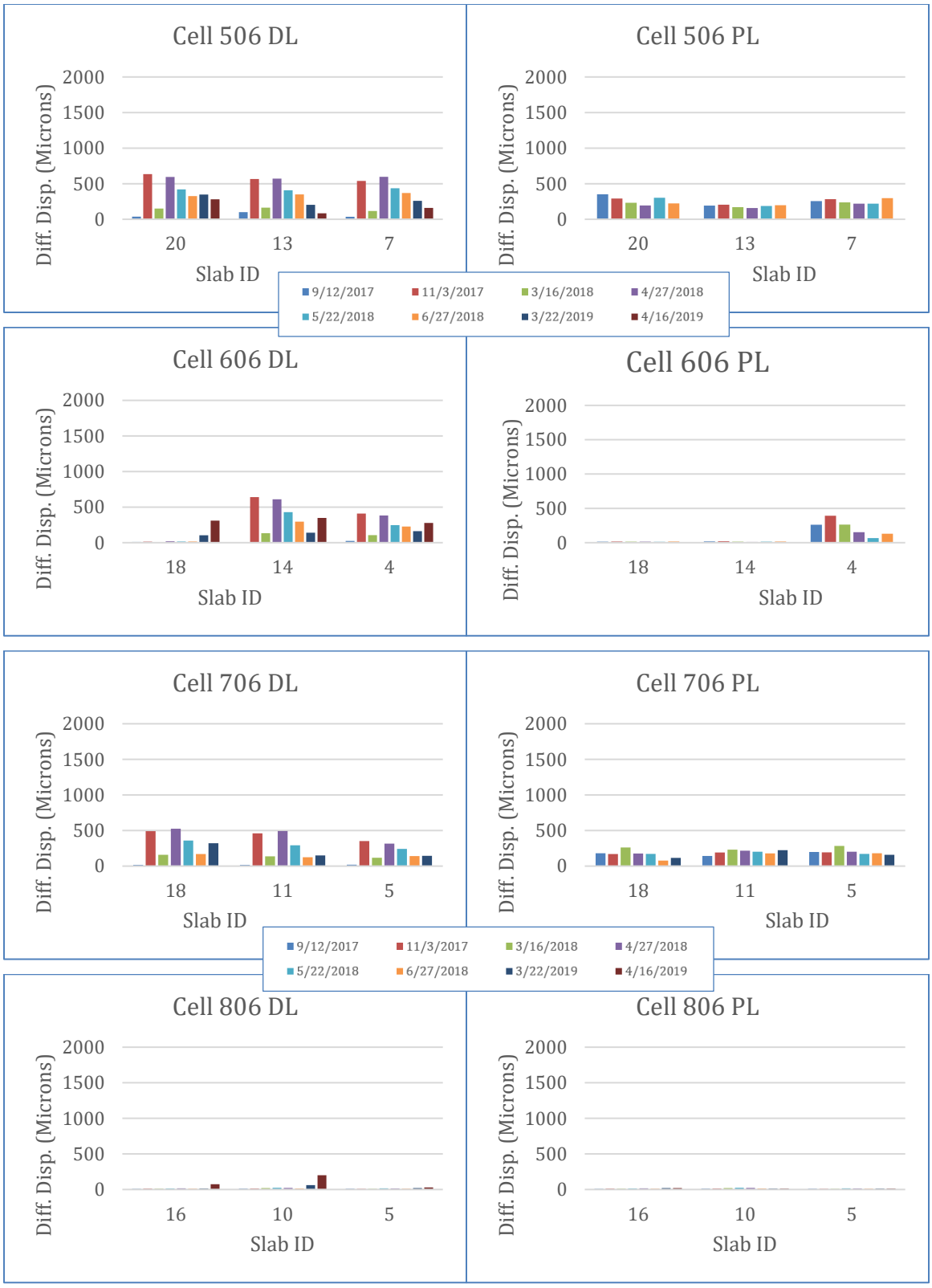

Figure 4-4. Differential displacement of Cells 506, 606, 706 and 806.

4.3 Loaded-side displacement

Loaded-side displacement is a good indicator of joint performance. Even though the LTEs and differential displacements for the Cells 139 and 239 were somewhat comparable, especially the outside lanes, the Cell 139 had significantly higher loaded-side displacement, as shown in Figure 4-5. This clearly indicates that cell 139 had poorer joint stiffness or weaker support compared to Cell 239.

Similar to LTEs and differential displacements, the loaded-side displacements for the Cells 705 and 805 are a concern. Between these two cells, the Cell 705 had experienced higher, and as much as twice, the loaded-side displacements compared to Cell 805.

The loaded-side displacement of Cells 506 through 806, as shown in Figure 4-6, also showed that the 806 is performing better than the other three cells.

Figure 4-5. Load-sided Displacement of Cells 139, 239, 705 and 805.

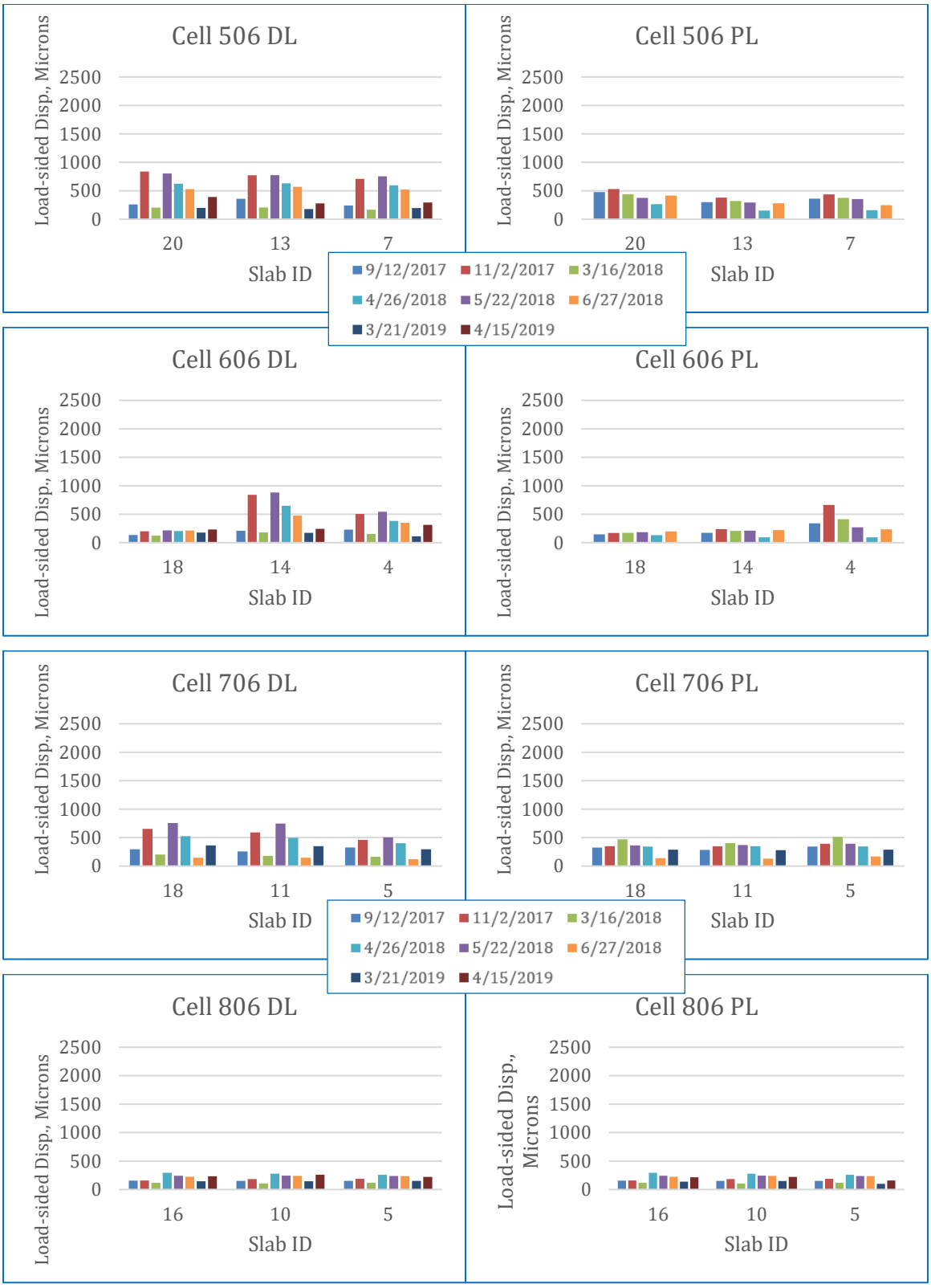

Figure 4-6. Load-sided Displacement of Cells 506, 606, 706 and 806.

5 CONCLUSIONS

While fiber reinforced concrete pavements or overlays had been constructed in the United States and many other countries, a comparison between the performance of fiber reinforced concrete pavements or overlays and their plain concrete counterparts could not be found because of lack of companion sections. The National Road Research Alliance funded and MnDOT constructed 2017 FRC research cells definitely provide a great opportunity for drawing such a comparison and quantifying the contribution of structural fibers in mitigating cracks, faulting and other distresses.

This report first presented a summary of the distresses observed in different cells during the first two years of service. The report then provided a discussion on the different sensor data collected during this period. The results of the joint performance tests conducted by using the falling weight deflectometer were discussed at the end of this report. The following major conclusions can be drawn from this report.

- In Cell 139, 75% slabs cracked with ~80,000 ESALs.
- Contribution of the fibers (@8lb/cy fiber, 30% RSR) on Cell 139 is not clear but cracked pieces were hold together by fibers.
- Cell 239 (4-inch thick) is performing better than Cell 139 but a significant number of longitudinal cracks developed in the second spring though.
- Large-paneled thin unbonded overlays experienced more longitudinal cracks compared to the narrow-paneled ones- which experienced more transverse cracks Compared to the pavement-on-grade cells, they experienced significantly higher fatigue cracks (Cells 705 and 805 vs Cells 606 through 806)
- With respect to cracking, Cells 506 through 806 are performing better than all other cells, with only three (until Oct 2019) cracks in Cell 506 (no fiber).
- Cell 506 has experienced joint spalling in many locations; all other FRC cells did not experience any.

- The cells in the mainline (Cells 705, 805, 506-806) had approximately 2.4 million ESALs on them by Oct 2019, well beyond the typical traffic load for low volume road designs.
- As Cells 506 through 806 (fiber dosage varied) have not experienced enough cracks yet, it is hard to quantify the contribution of fibers in mitigating fatigue cracks. These cells have successfully carried 2.4 million ESALs until October 2019. This observation indicates that the critical distress for the small panel thin concrete pavements on the relatively stiff base layer may not be the fatigue cracking, but other distresses like faulting. Cells 139, 239, 705 and 805 have experienced low faulting (1 to 2 mm)
- Fibers' contribution was observed in Cells 506 through 806.
- Cell 606, 706 and 806 showed lower faulting than Cell 506 (no fiber).
- Cells 705 and 805 (overlay with nonwoven geotextile) experienced lower faulting than the concrete pavement cells (Cells 506 -806).
- Cell 806 (11 lb/cy fiber) showed higher LTE than Cell 506 (no fiber).
- LTE for Cell 239 (inner lane) was higher than the outer lane, which was loaded only by early construction traffic and FWD testing. Surprisingly, Cells 705 and 805 always showed low LTE even though these cells have not experienced significant faulting.
- Fibers helped in reducing the joint displacement (.e.g., Cell 506 vs Cell 806)
- The temperature gradient of all the cells was found to be linear to a great extent. As much as 60% of the time, slabs experienced a negative temperature gradient.
- The environmental strains measured showed that they possess a good relationship with the temperature.
- The dynamic strains were higher in general during the springtime when the base and subgrade support was weak.
- Joint opening sensor data provided mixed results. Some cells showed greater joint openings than the other cells, irrespective of the fiber dosages and cell designs.

6 REFERENCES

1. Barman, M., (2014). Joint Performance Characterization of Bonded Whitetopping Overlays. Ph. D Dissertation, Pittsburgh: University of Pittsburgh.Advisor: Vandenbossche, J.

2. Burnham and Tewfik (2007). Development of a Computer Program for Selecting Peak Dynamic Sensor Responses from Pavement Testing. Minnesota Department of Transportation. St. Paul, MN.

3. MnDOT (2018). Report on 2017 MnROAD Construction Activities, Report Number: MN/RC 2018-16, Minnesota Department of Transportation, St. Paul, Minnesota.

4. Selezneva, O., Jiang, J., Tayabji, S. D. (1998). Preliminary Evaluation and Analysis of LTPP Faulting Data – Final Report., Federal Highway Administration, Virgina.

APPENDIX A

Second Year Distress Maps

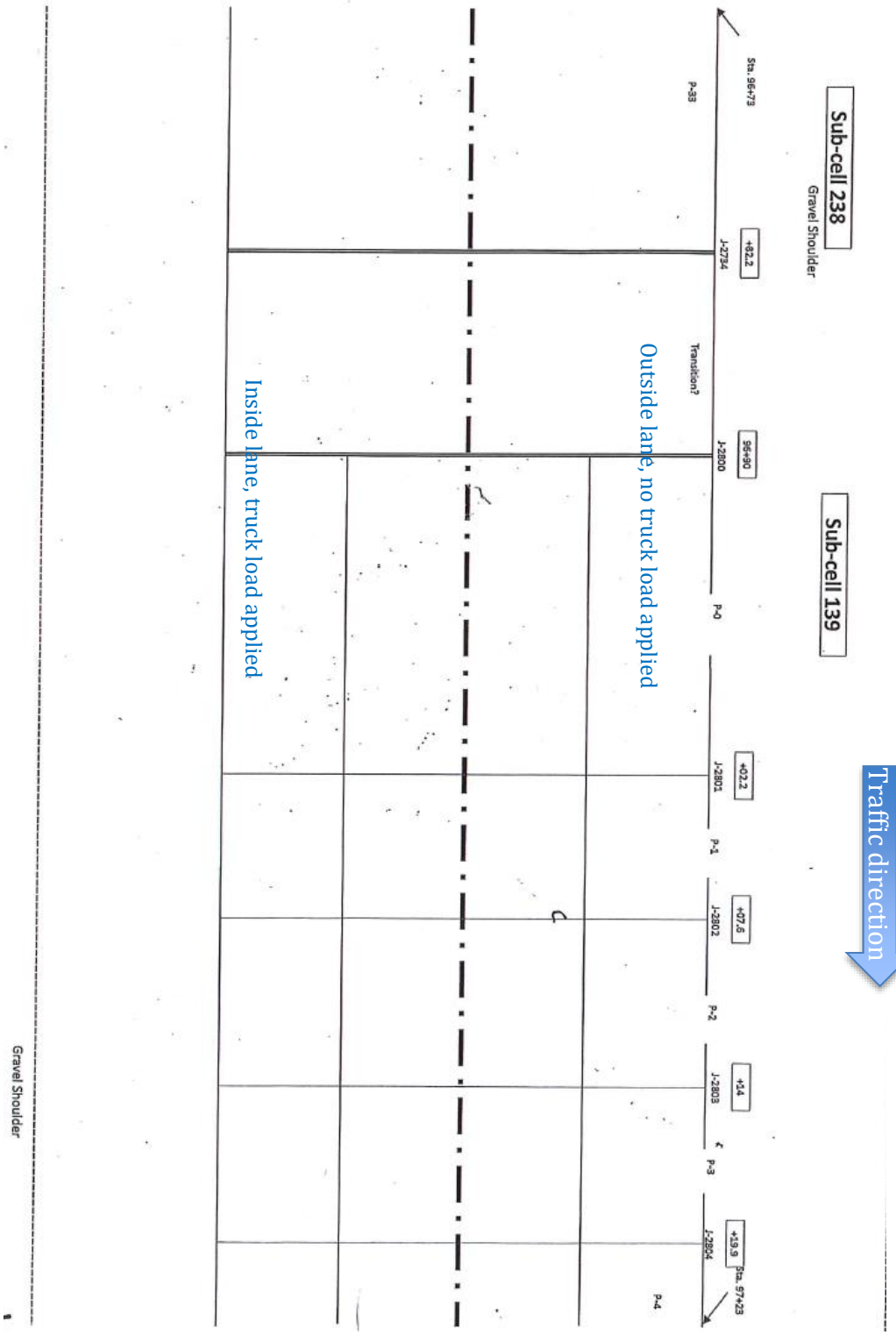

Figure A1: Distress map for Cell 139

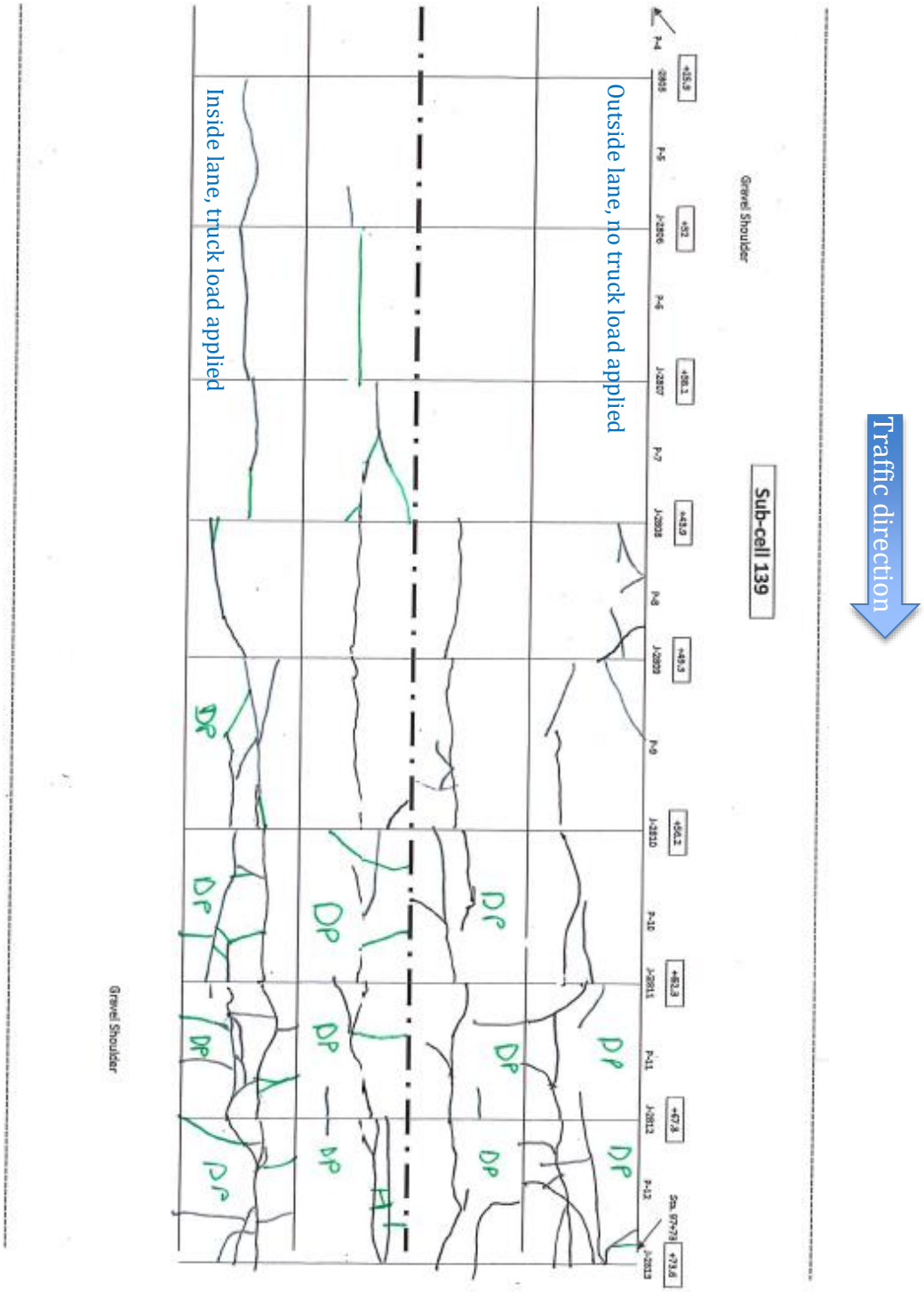

Cracks until December 2019; cracks colored green were documented on December 4, 2019.

Figure A2: Distress map for Cell 139.. contd.

Date of survey: May 1, 2018

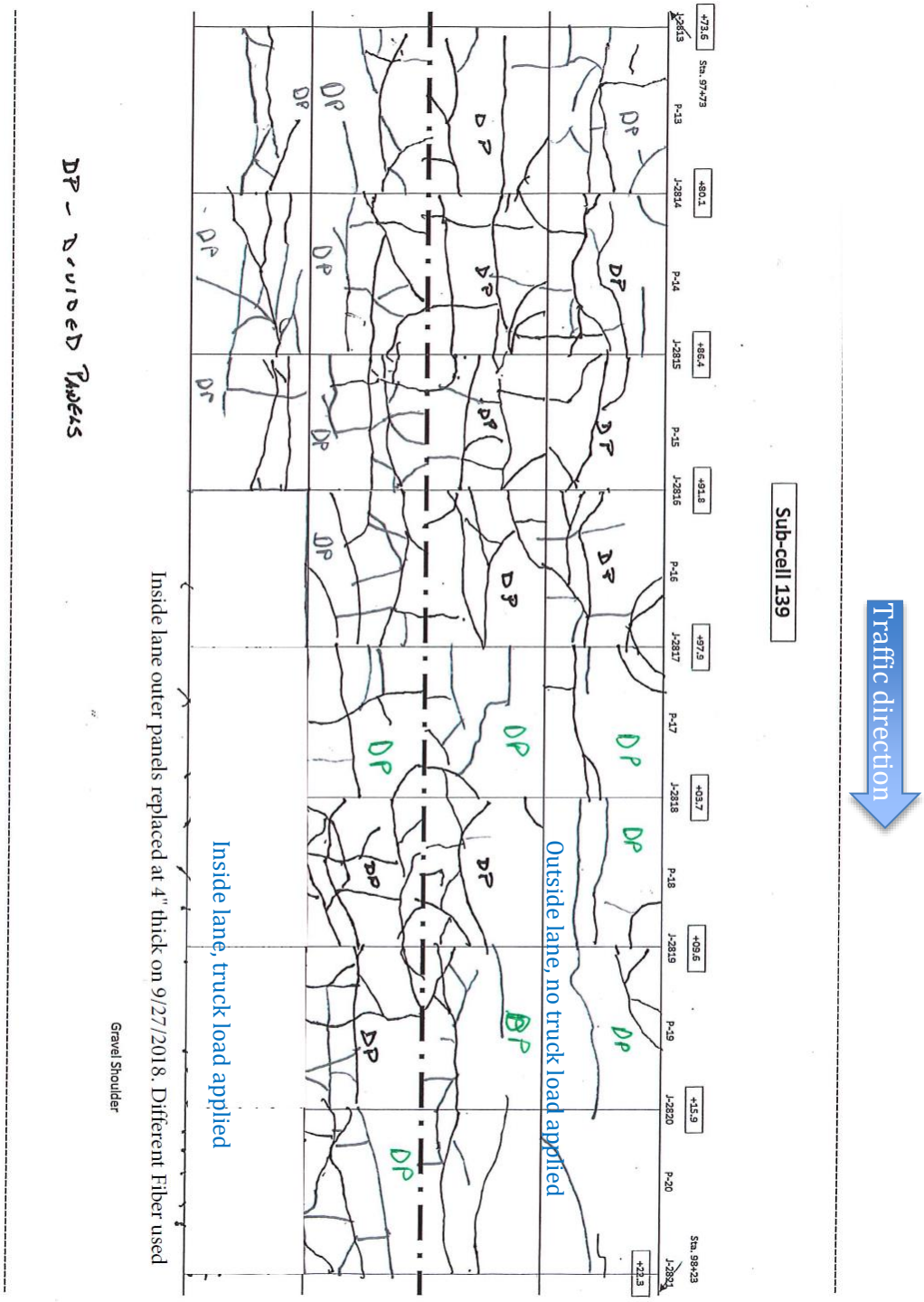

Cracks until December 2019; cracks colored green were documented on December 4, 2019.

Figure A3: Distress map for Cell 139.. contd.

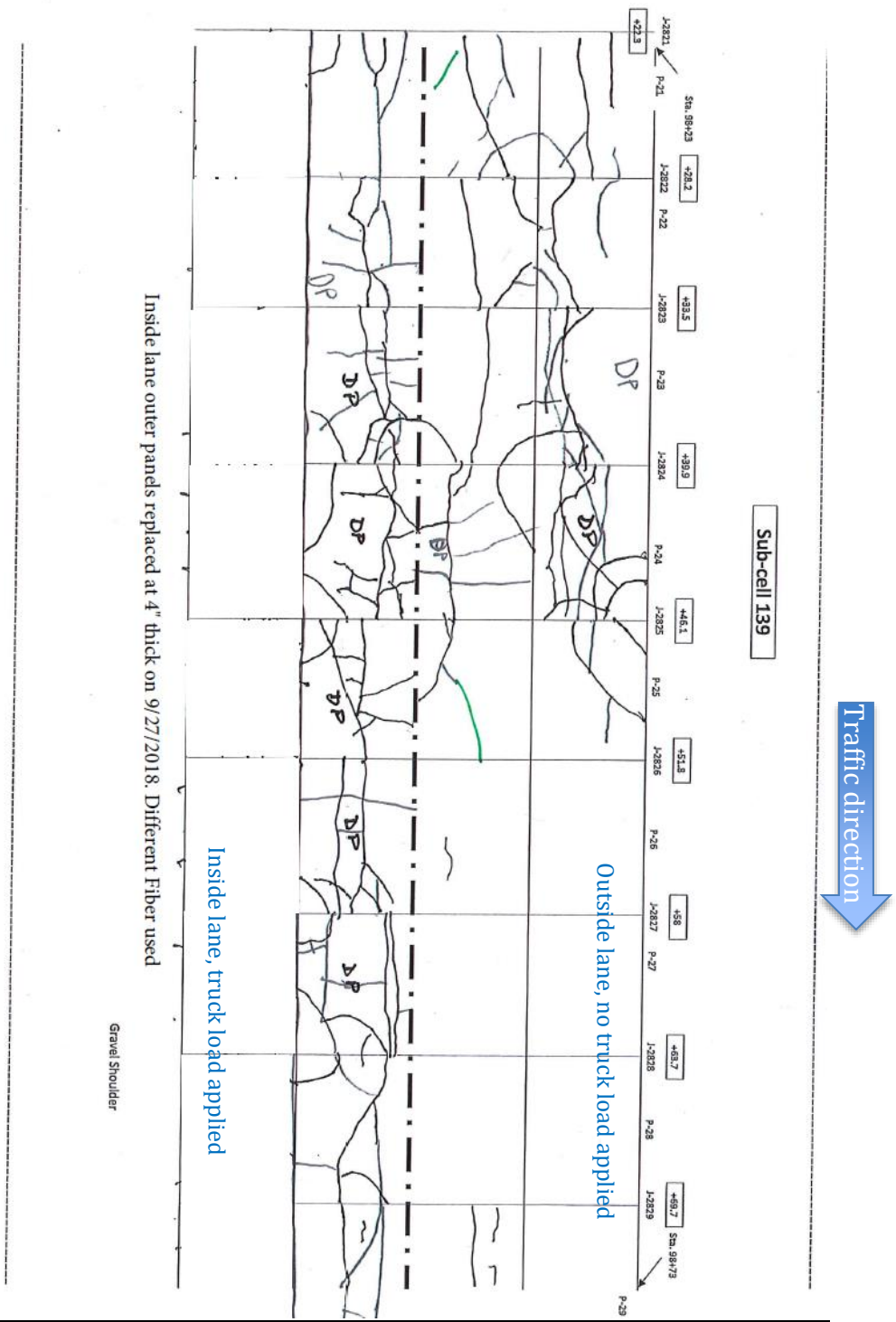

Cracks until December 2019; cracks colored green were documented on December 4, 2019.

Figure A4: Distress map for Cell 139.. contd.

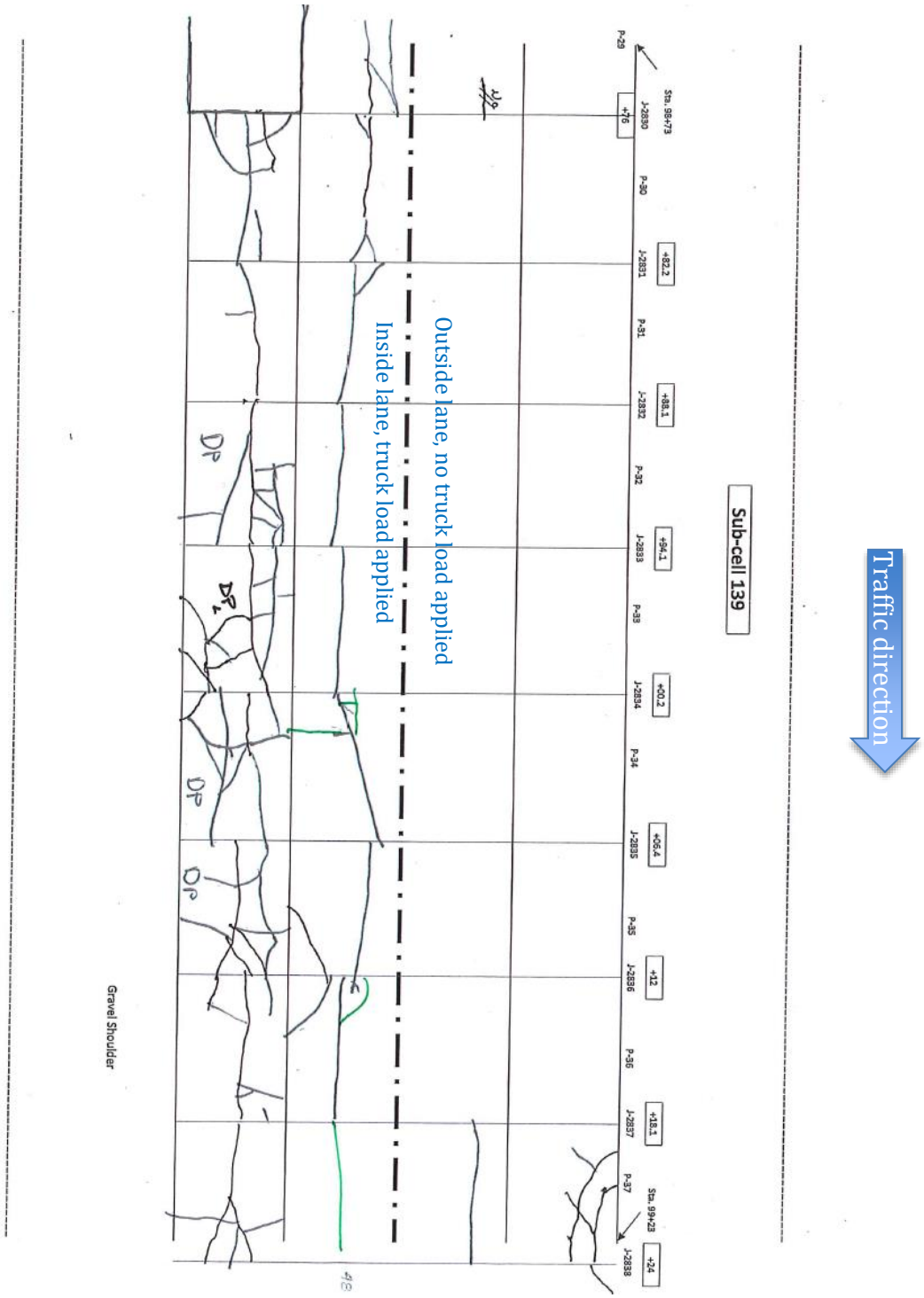

Cracks until December 2019; cracks colored green were documented on December 4, 2019.

Figure A5: Distress map for Cell 139.. contd.

Cracks until December 2019; cracks colored green were documented on December 4, 2019.

Figure A6: Distress map for Cell 139.. contd.

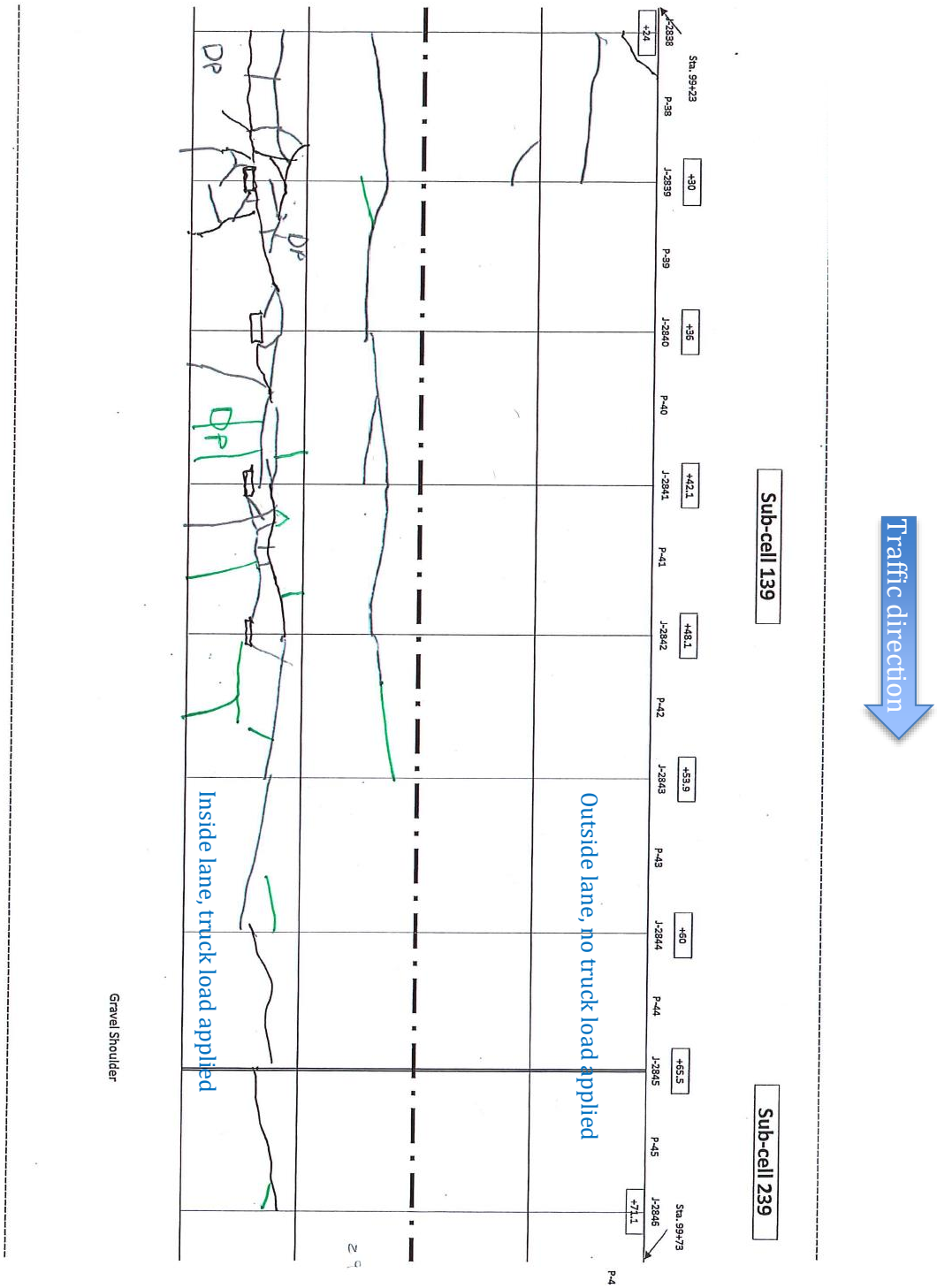

Cracks until December 2019; cracks colored green were documented on December 4, 2019.

Figure A7: Distress map for Cell 139.. contd.

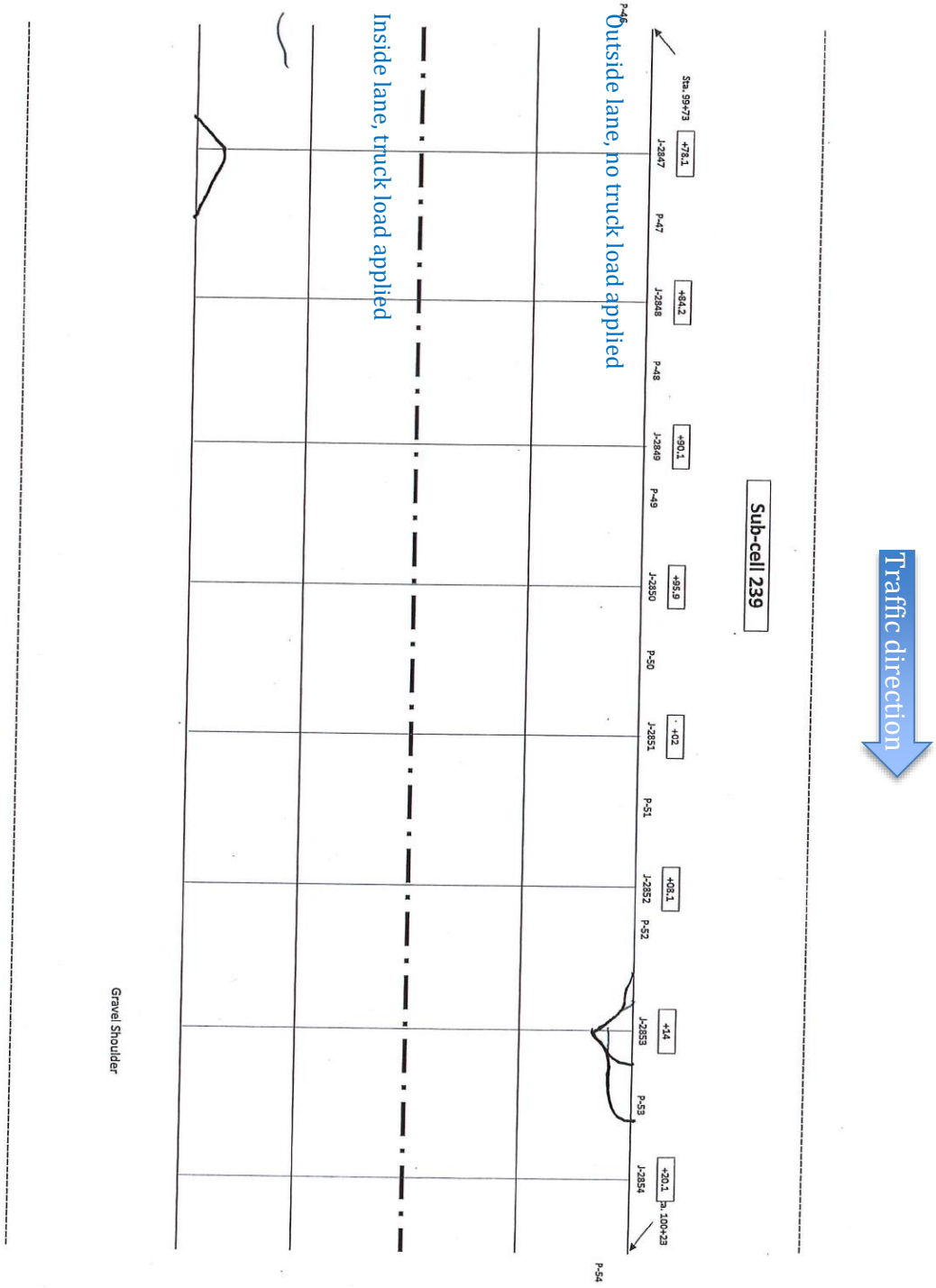

Cracks until December 2019; cracks colored green were documented on December 4, 2019.

Figure A8: Distress map for Cell 239.

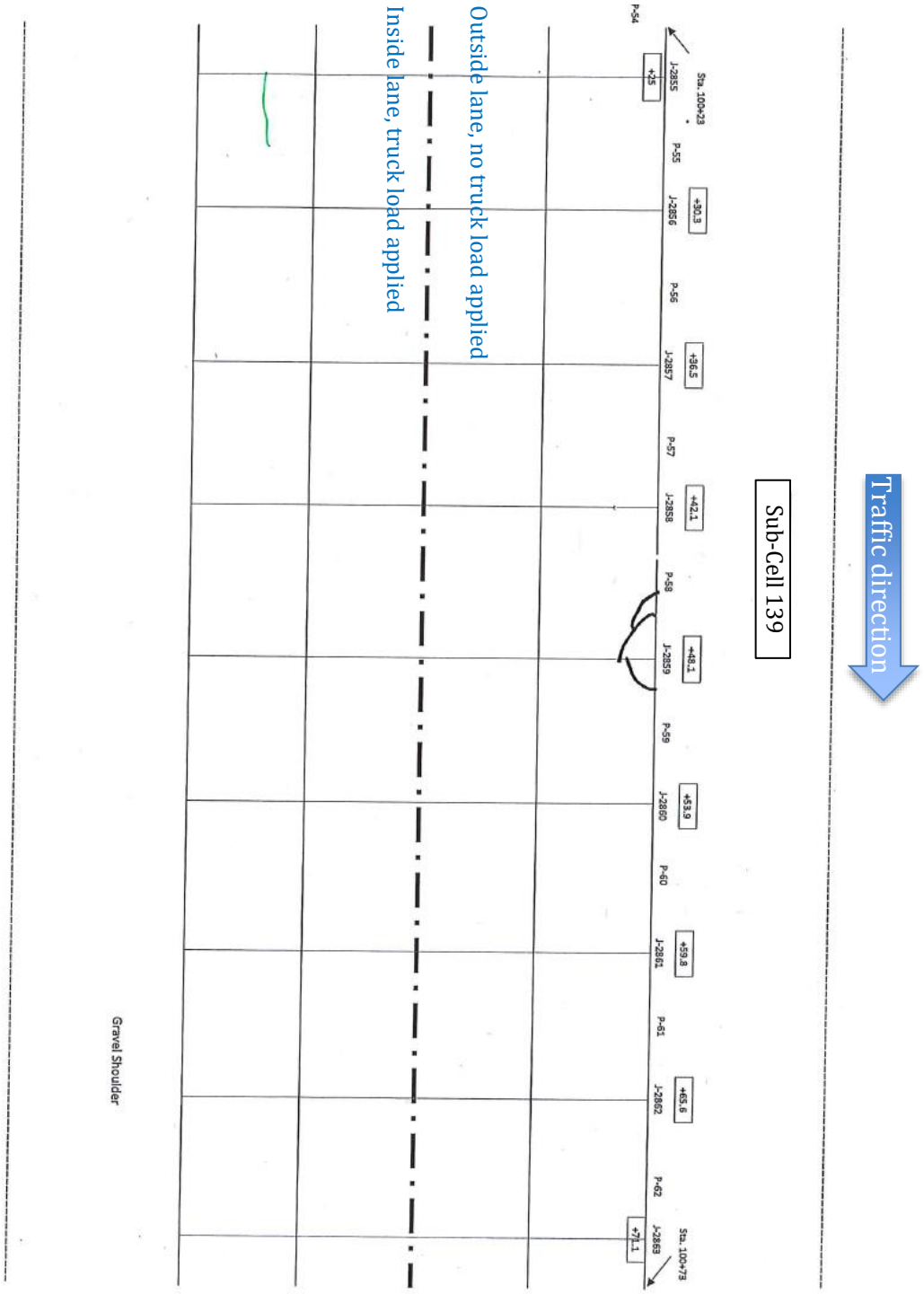

Cracks until December 2019; cracks colored green were documented on December 4, 2019.

Figure A9: Distress map for Cell 239.. contd.

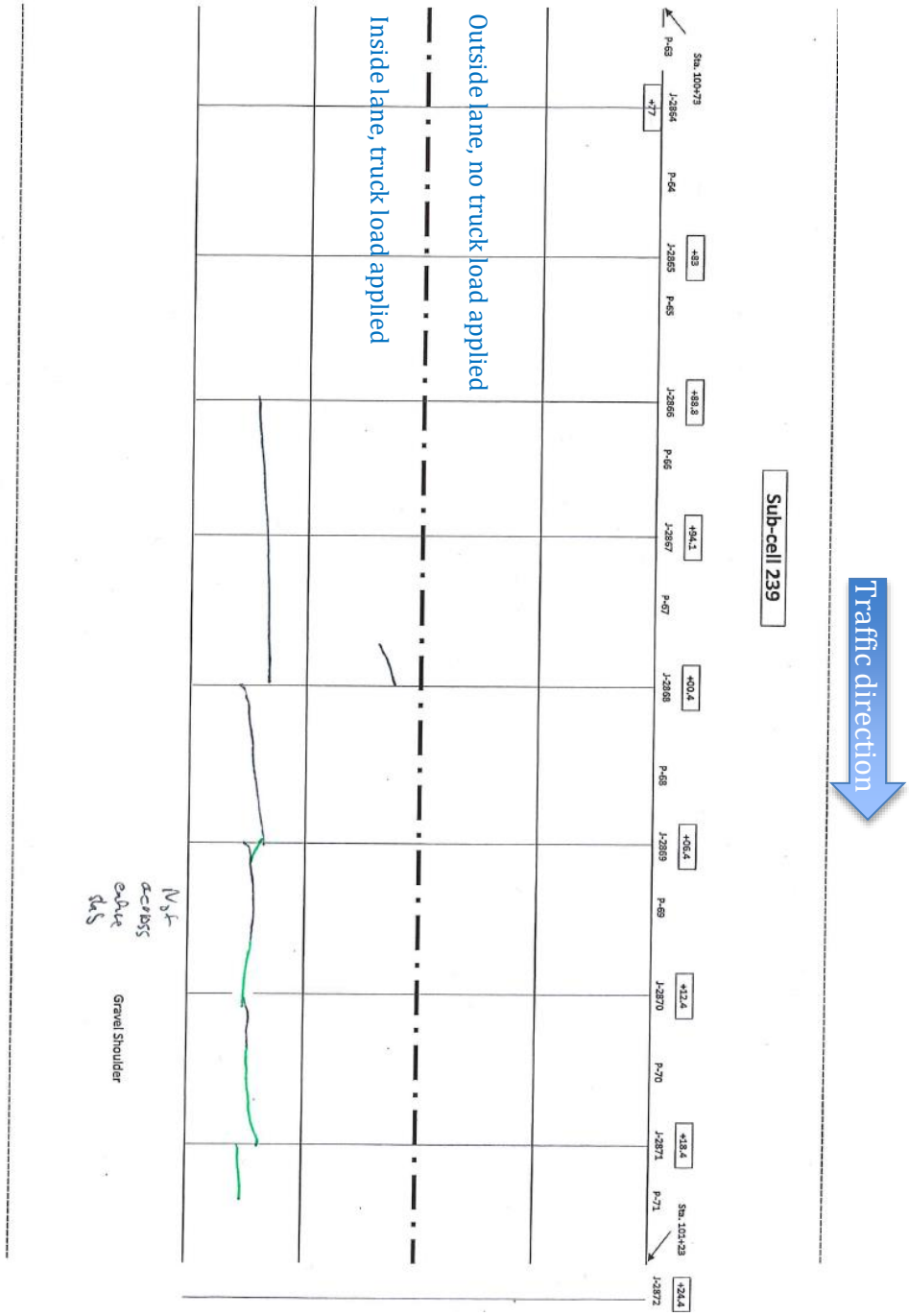

Cracks until December 2019; cracks colored green were documented on December 4, 2019.

Figure A10: Distress map for Cell 239.. contd.

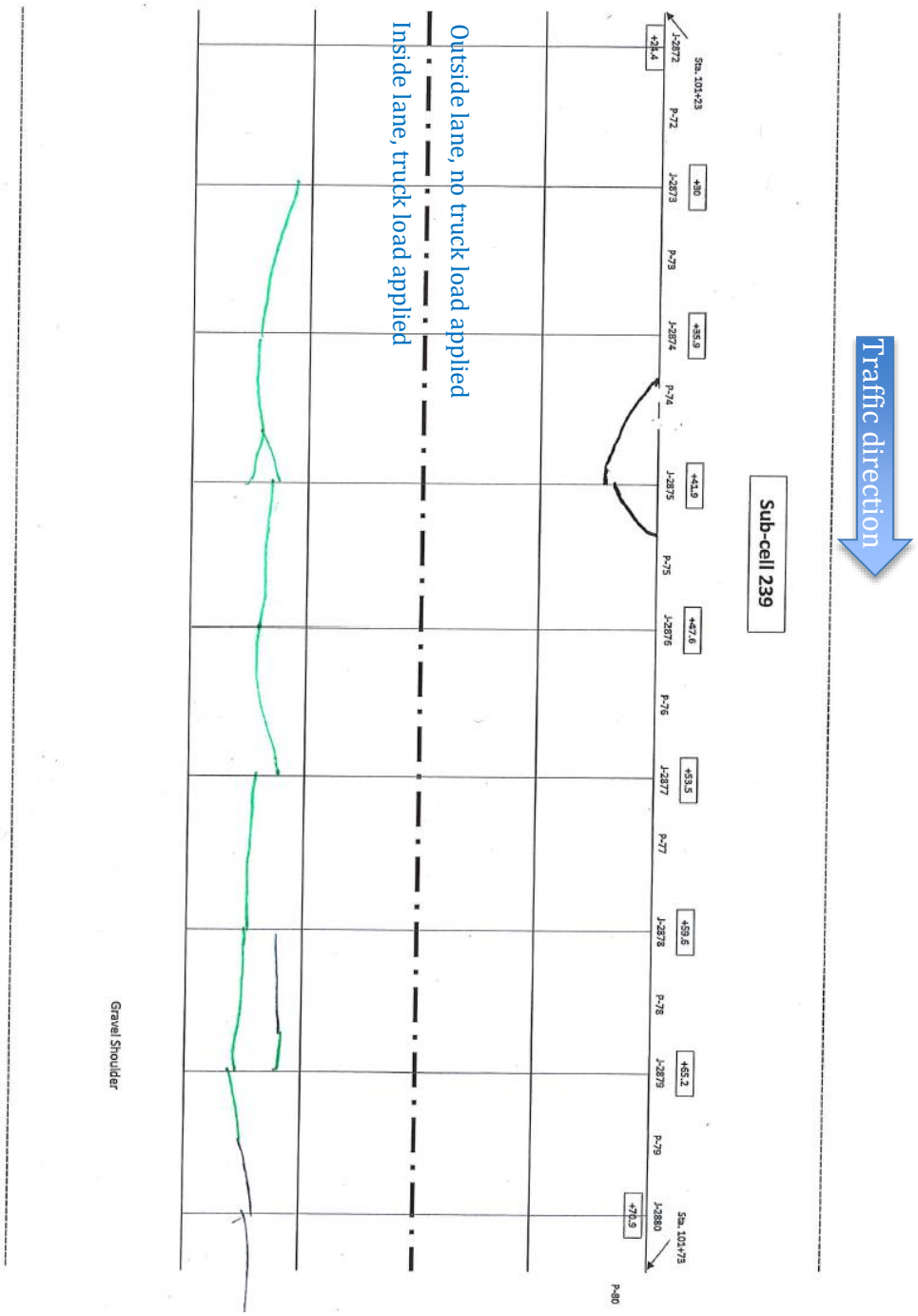

Cracks until December 2019; cracks colored green were documented on December 4, 2019.

Figure A11: Distress map for Cell 239.. contd.

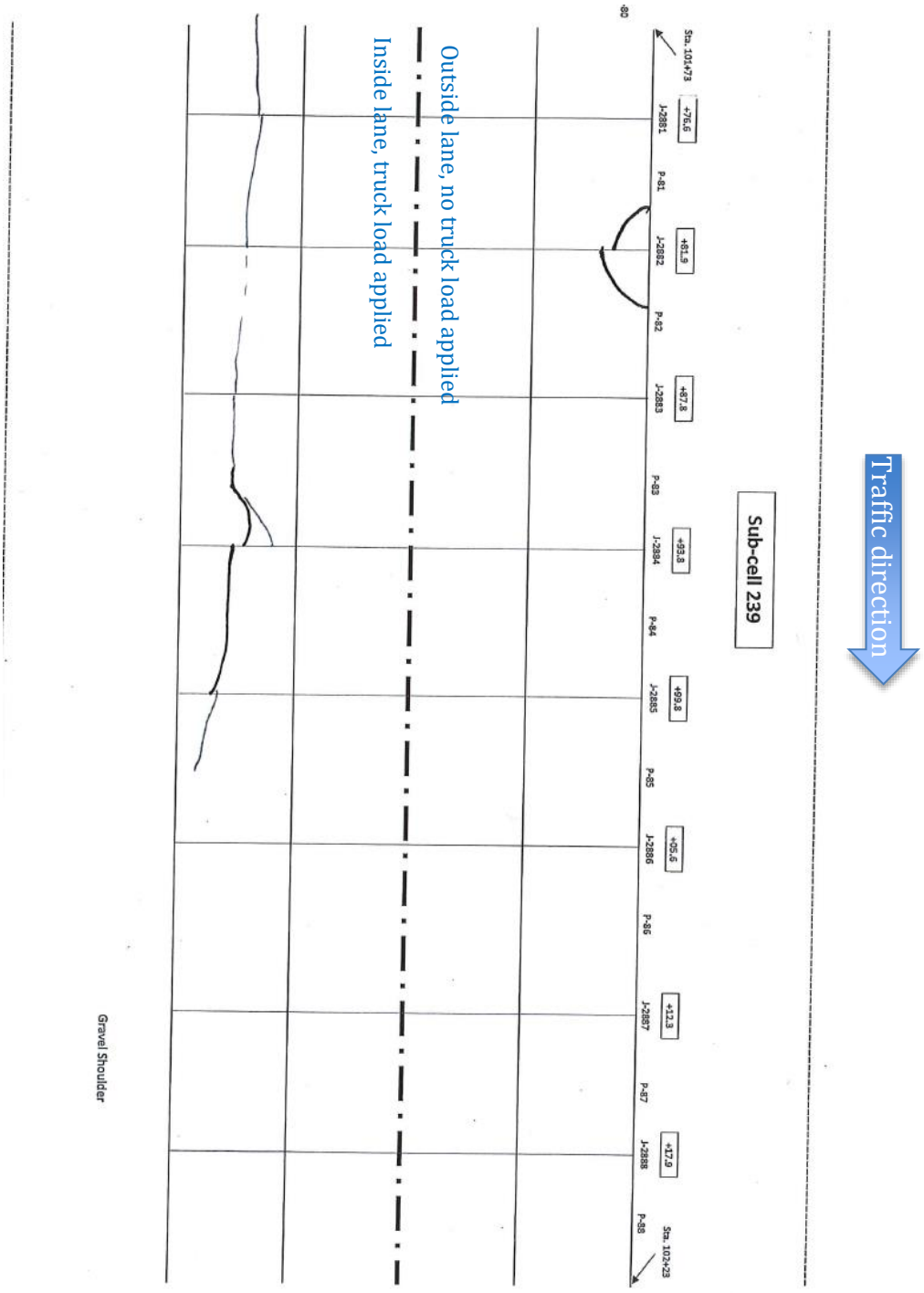

Cracks until December 2019; cracks colored green were documented on December 4, 2019.

Figure A12: Distress map for Cell 239.. contd.

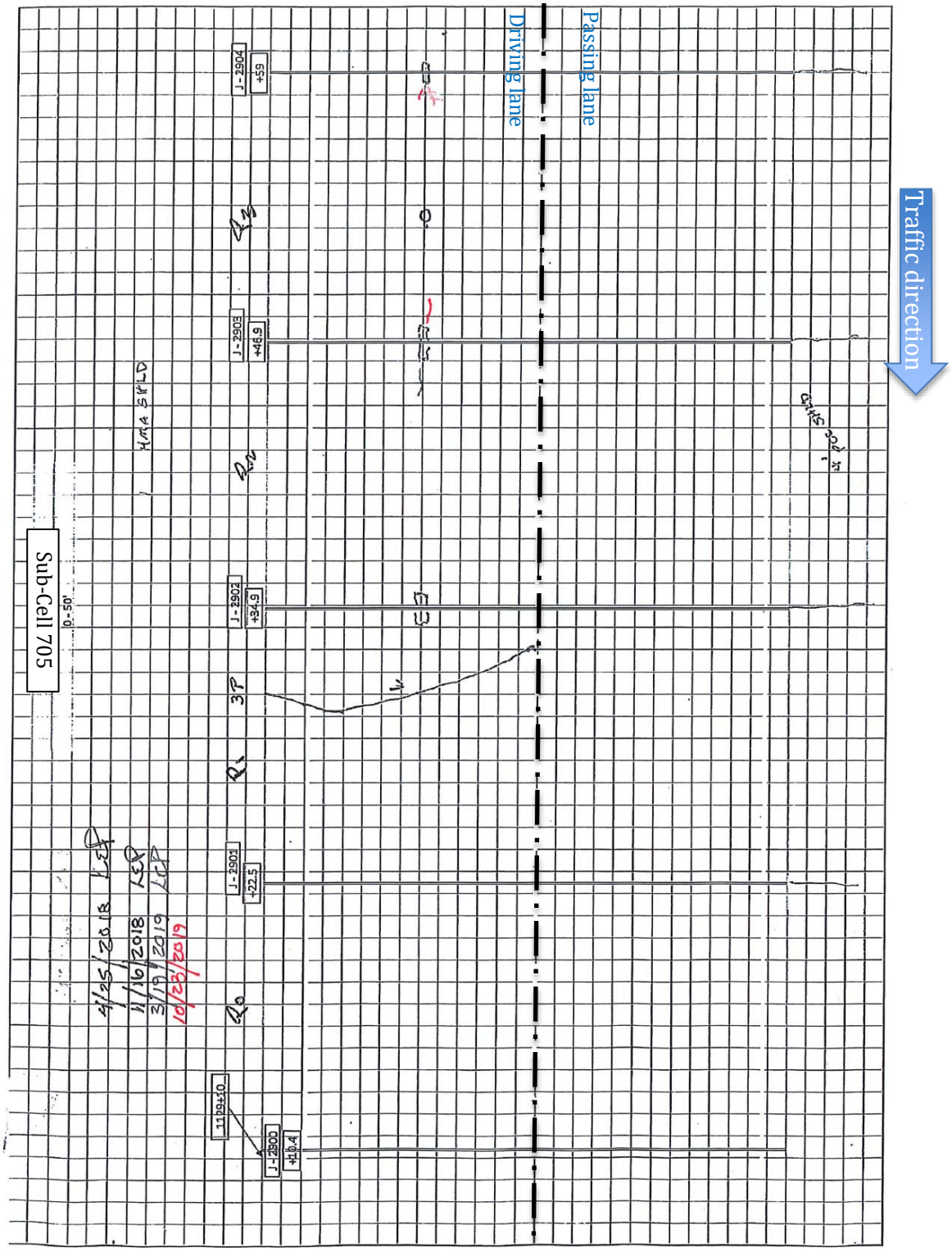

Cracks until October 2019; cracks colored red were documented on October 23, 2019.

Figure A13: Distress map for Cell 705.

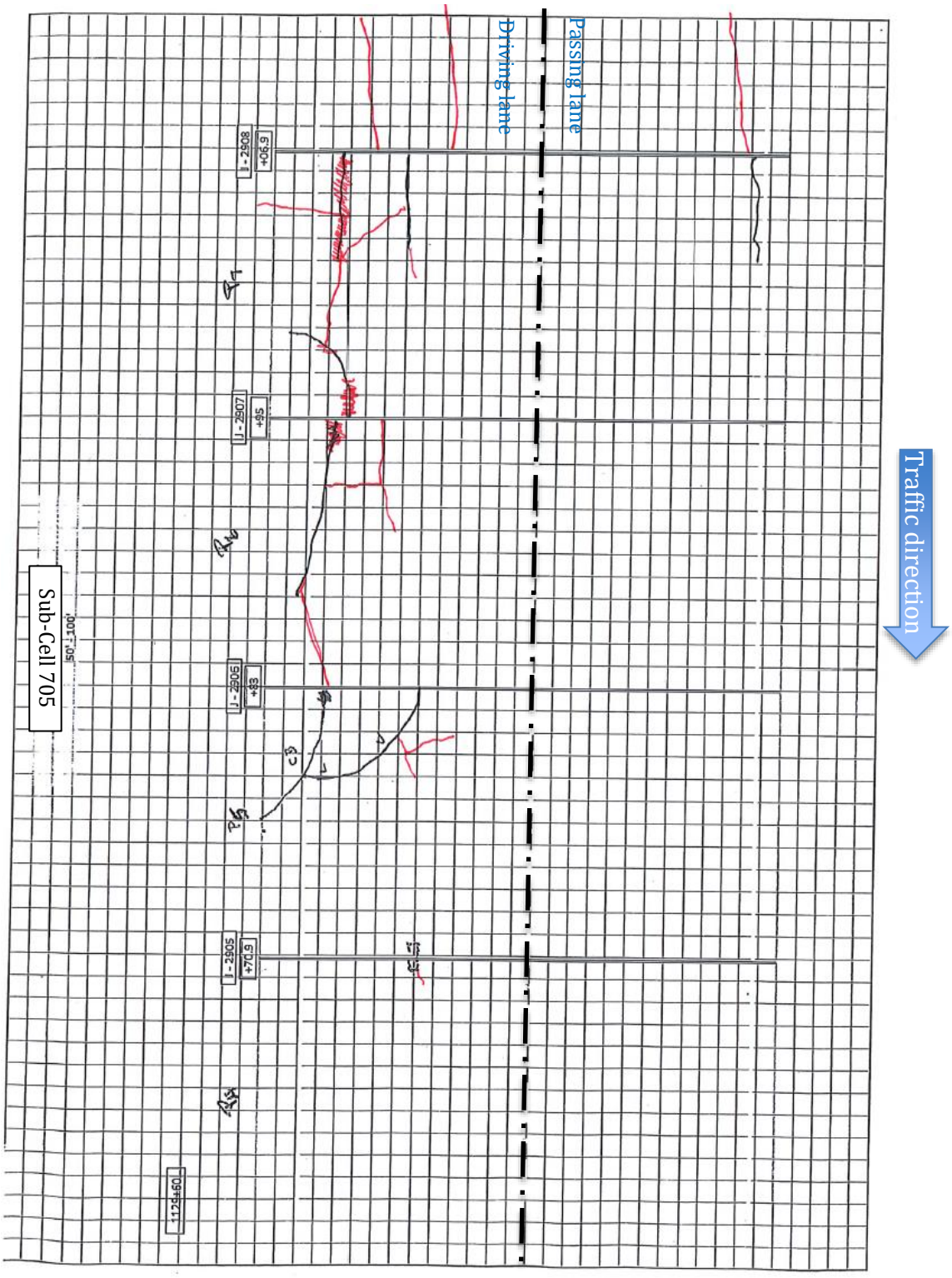

Cracks until October 2019; cracks colored red were documented on October 23, 2019.

Figure A14: Distress map for Cell 705.. contd.

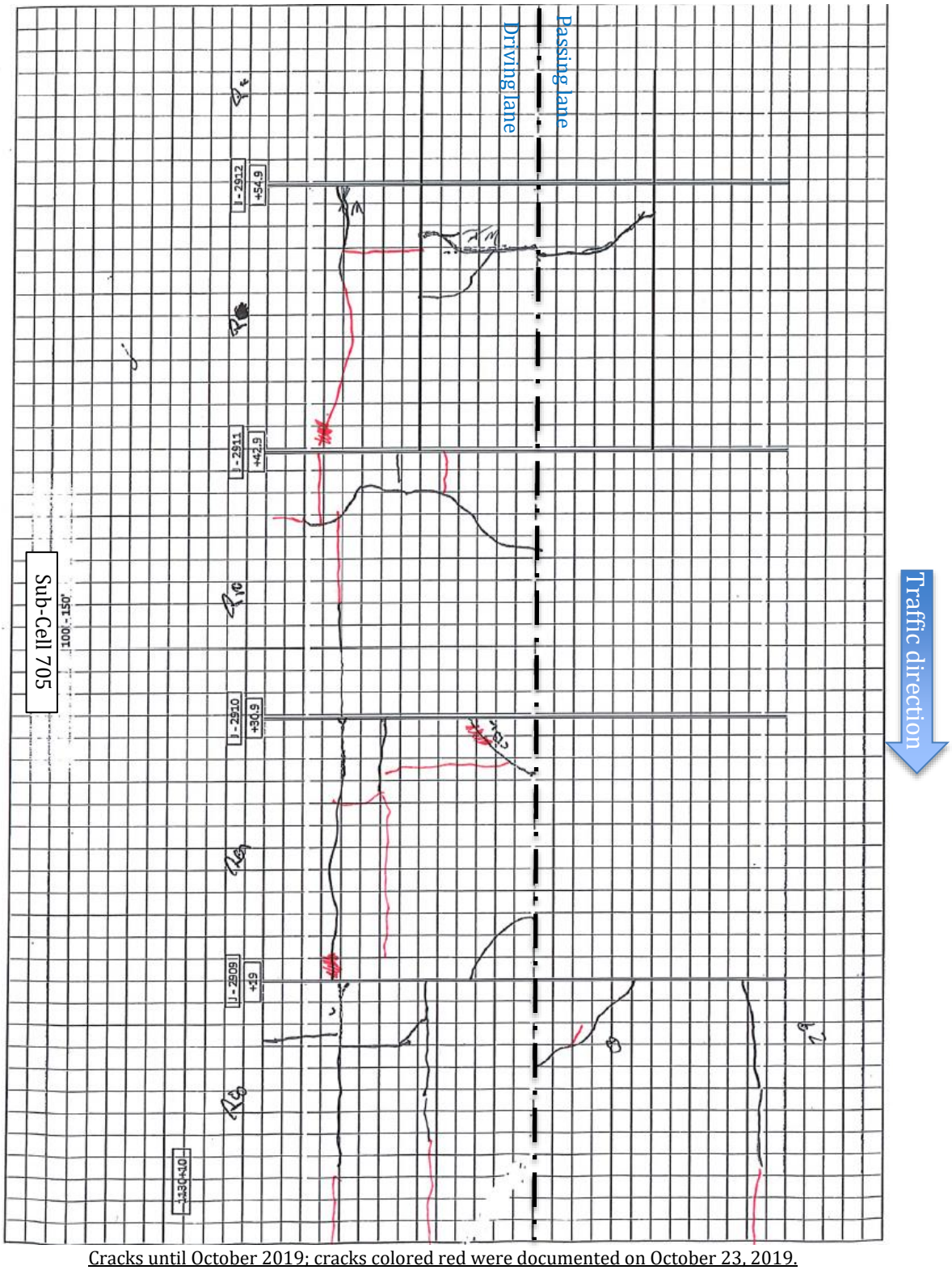

Cracks until October 2019; cracks colored red were documented on October 23, 2019.

Figure A15: Distress map for Cell 705 .. contd.

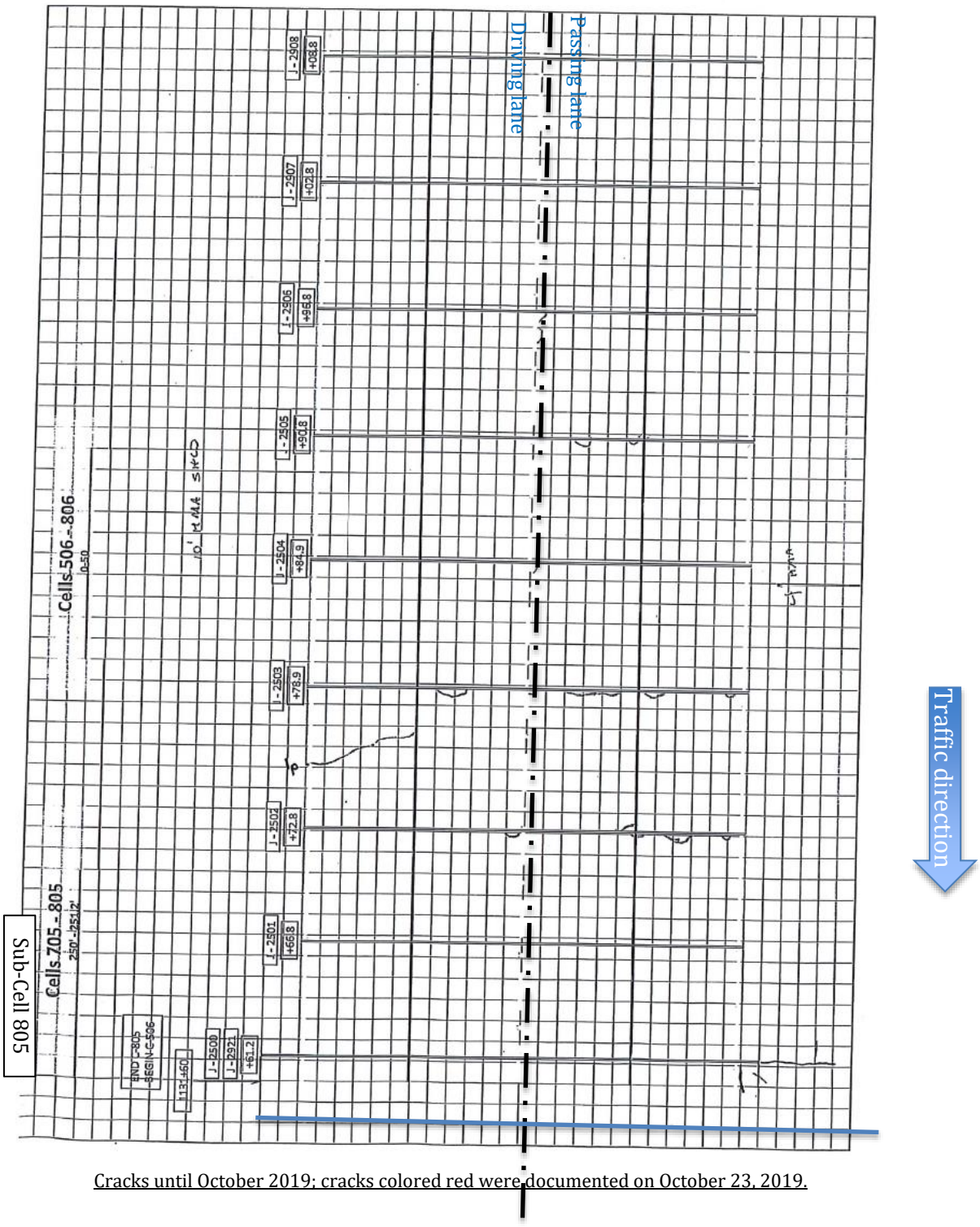

Cracks until October 2019; cracks colored red were documented on October 23, 2019.

Figure A16: Distress map for Cell 805.

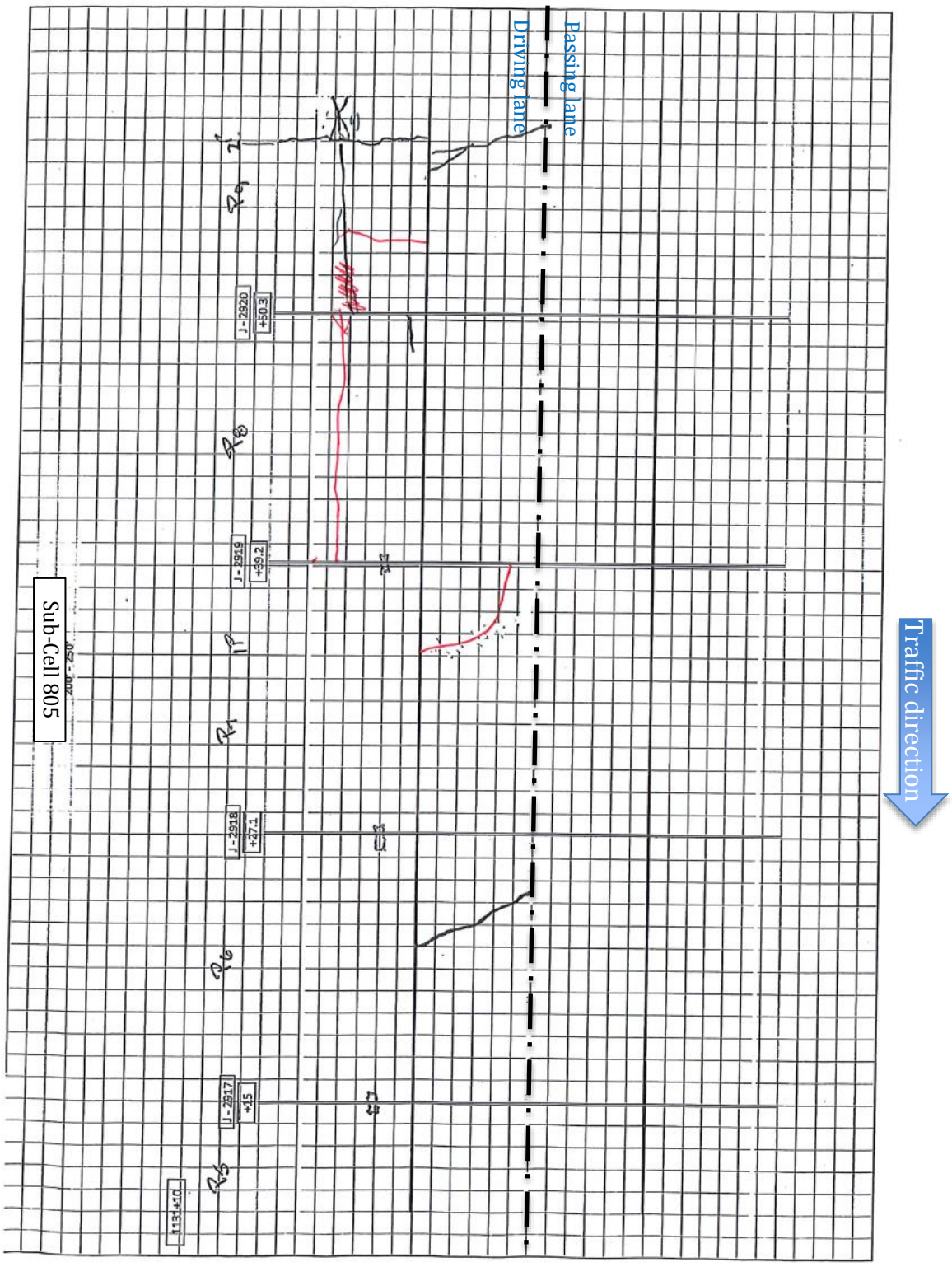

Cracks until October 2019; cracks colored red were documented on October 23, 2019.

Figure A17: Distress map for Cell 805.. contd.

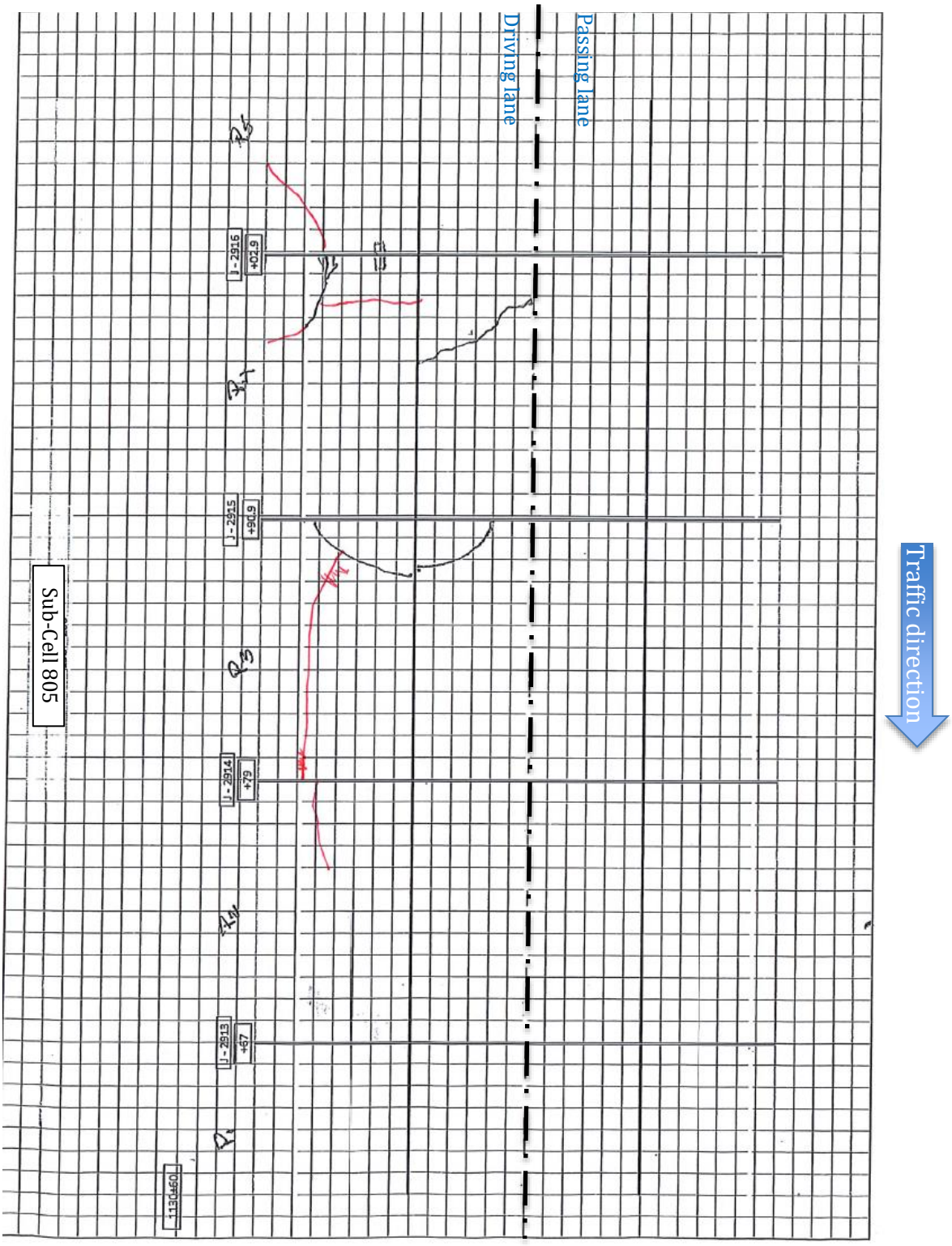

Cracks until October 2019; cracks colored red were documented on October 23, 2019.

Figure A18: Distress map for Cell 805.

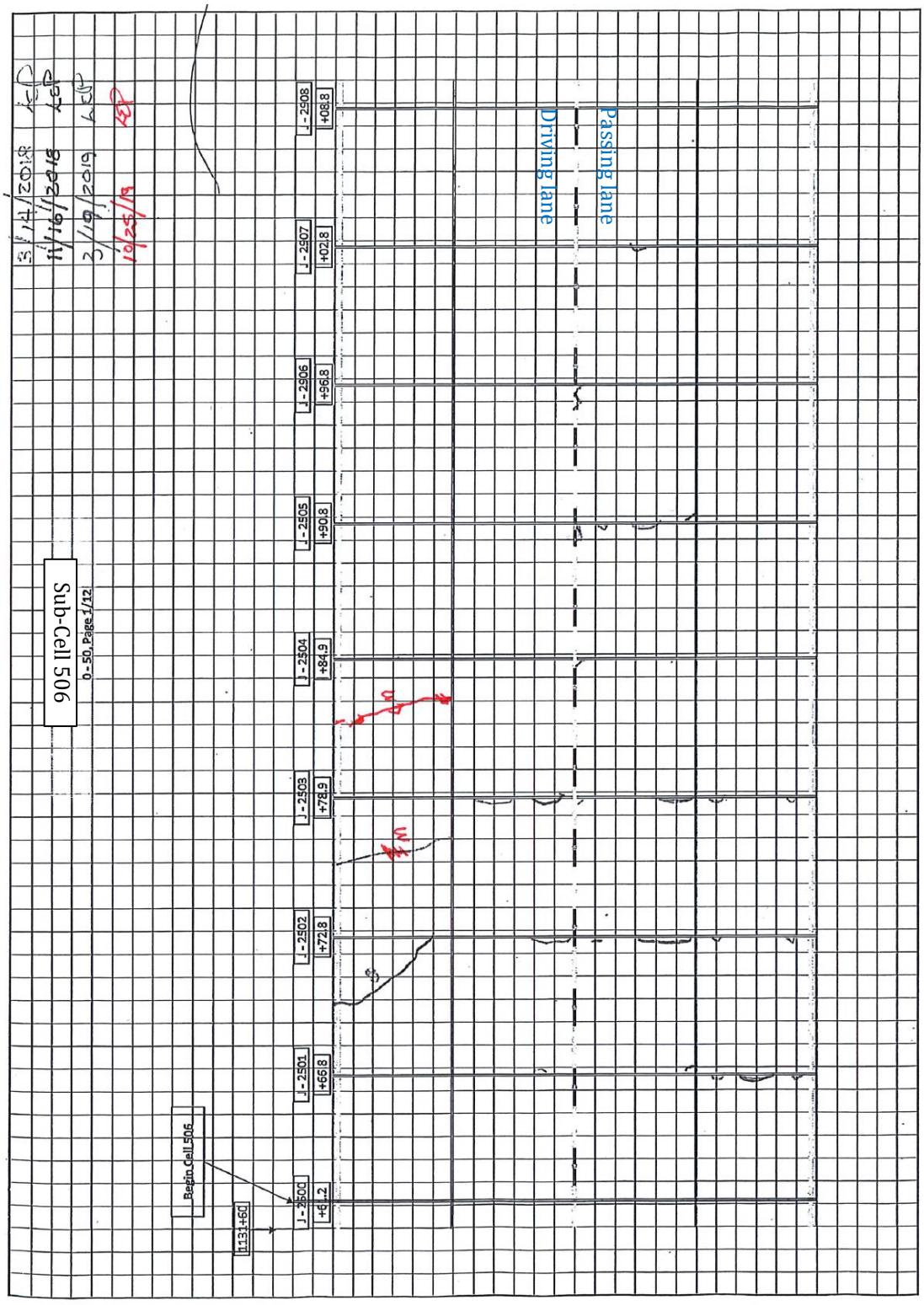

Cracks until October 2019; cracks colored in red were documented on October 25, 2019.

Figure A19: Distress map for Cell 506.

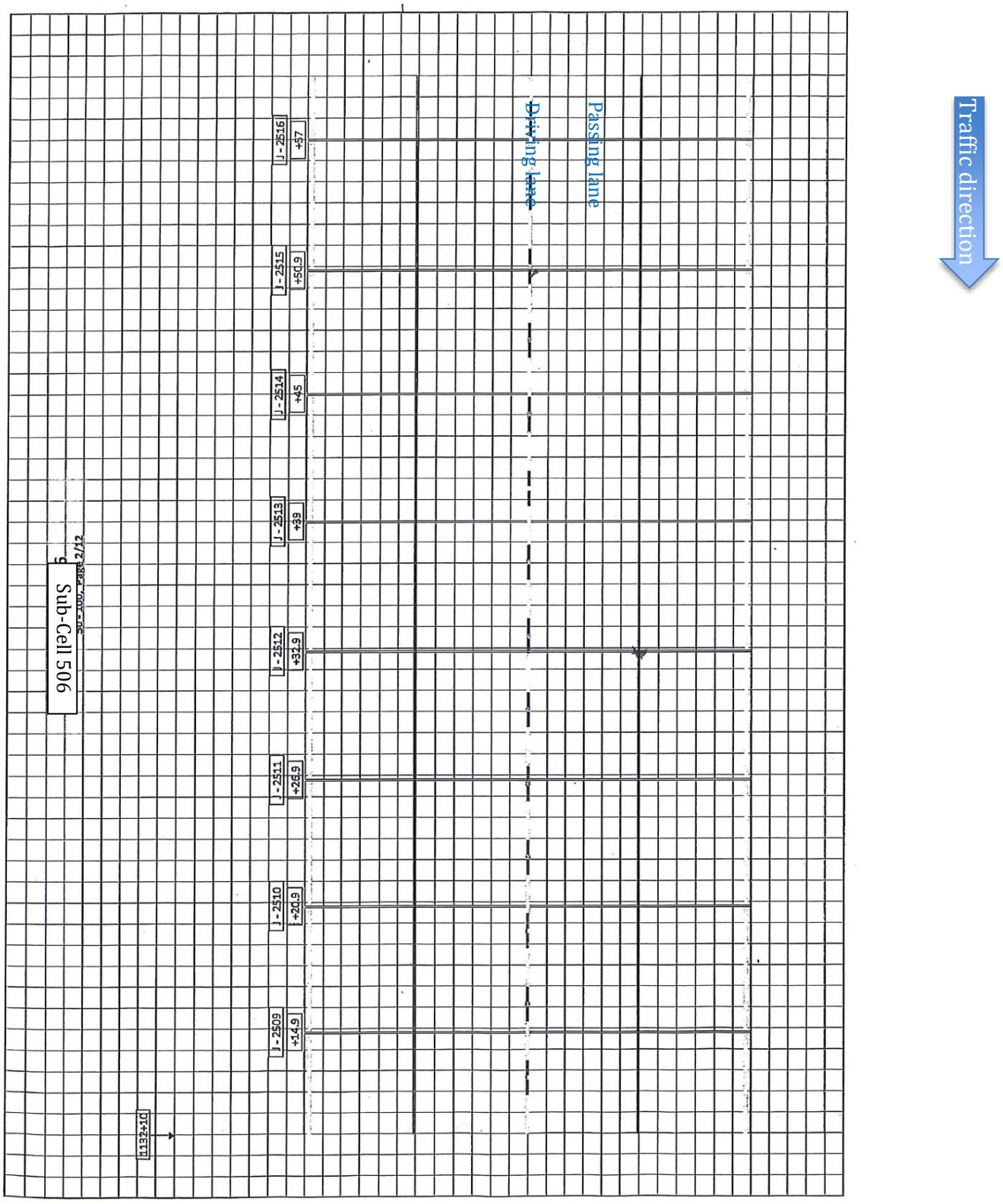

Cracks until October 2019; cracks colored in red were documented on October 25, 2019.

Figure A20: Distress map for Cell 506.. contd.

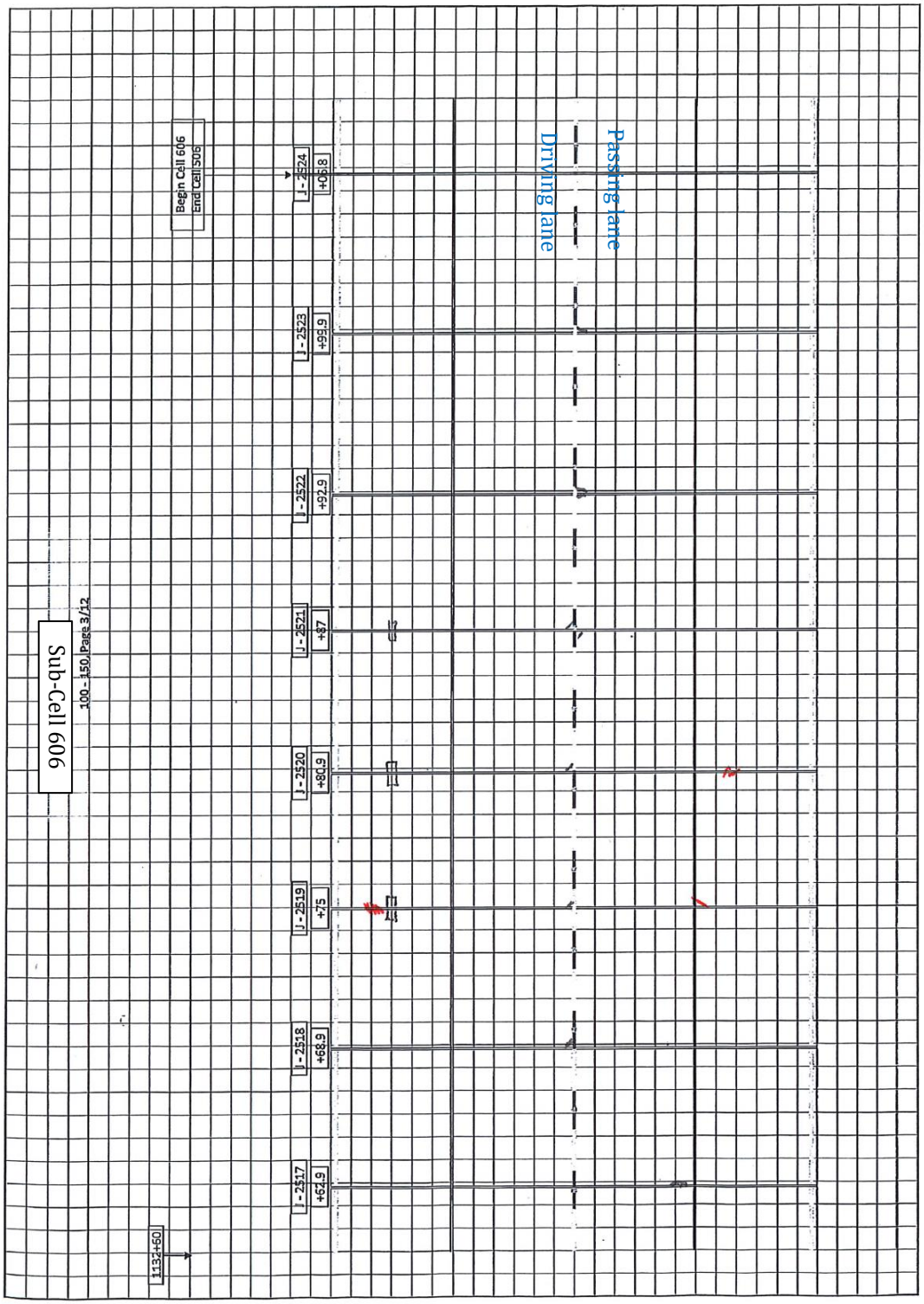

Cracks until October 2019; cracks colored in red were documented on October 25, 2019.

Figure A21: Distress map for Cell 606.

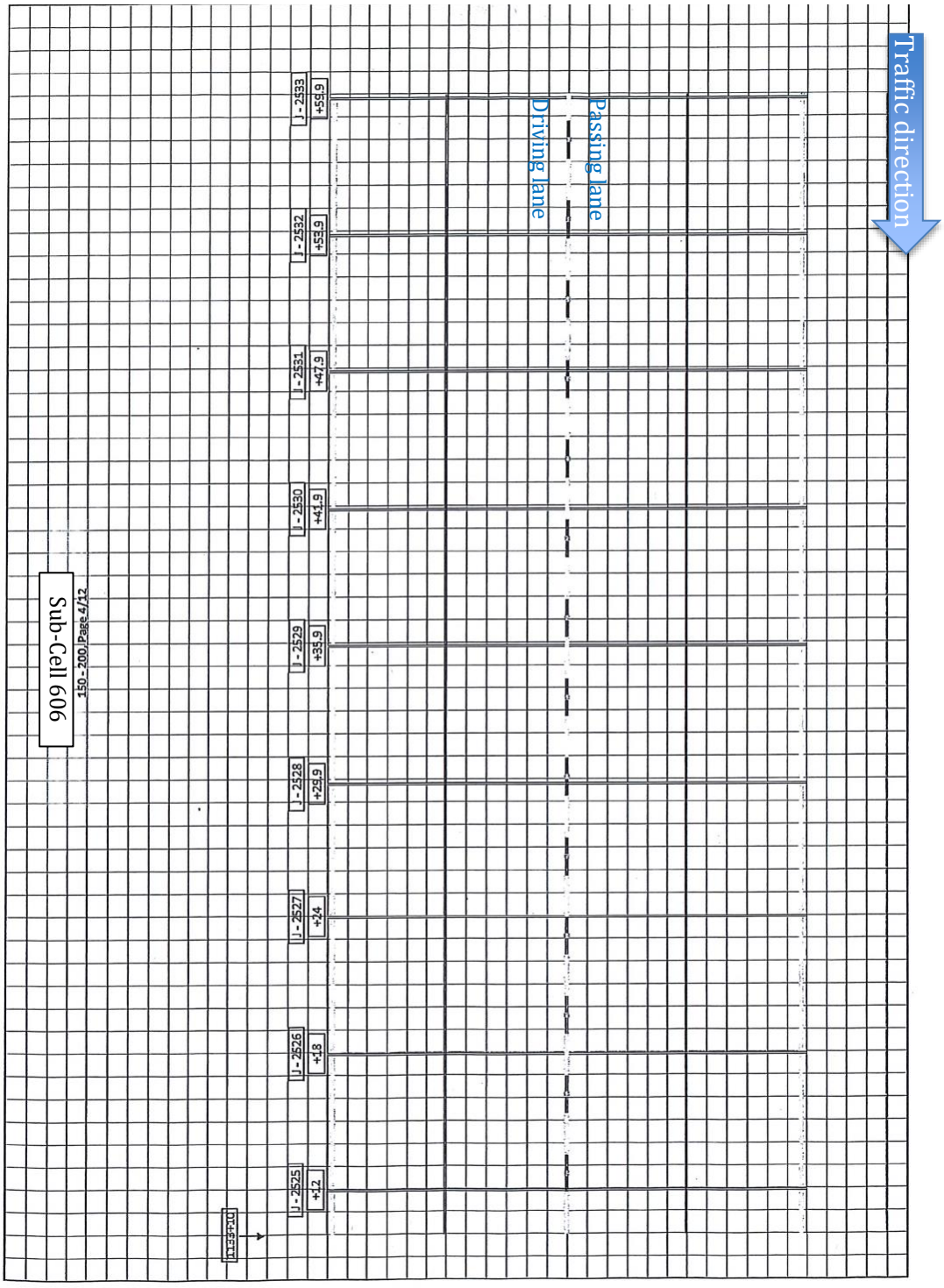

Cracks until October 2019; cracks colored in red were documented on October 25, 2019.

Figure A22: Distress map for Cell 606.. contd.

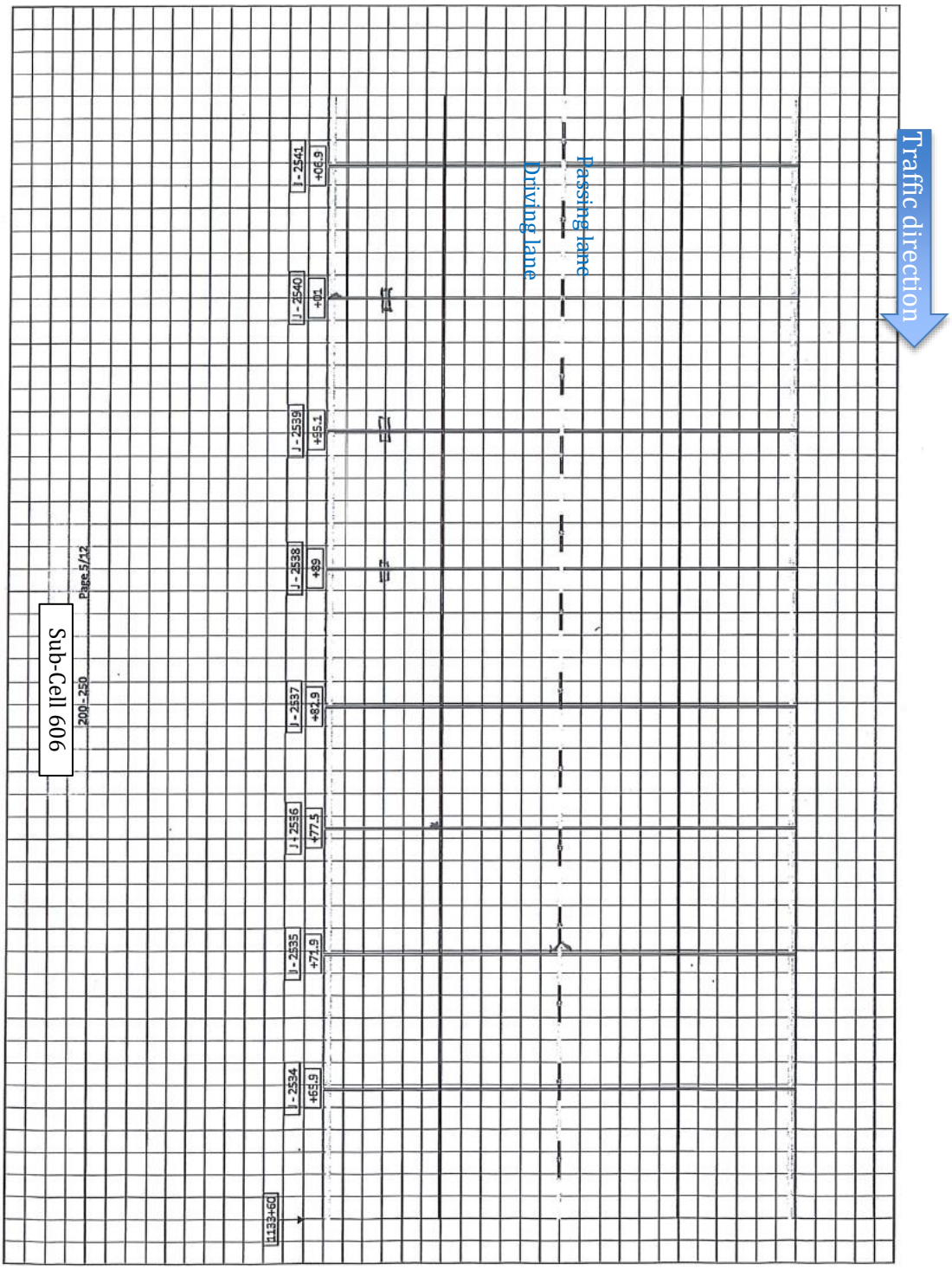

Cracks until October 2019; cracks colored in red were documented on October 25, 2019.

Figure A23: Distress map for Cell 606 .. contd.

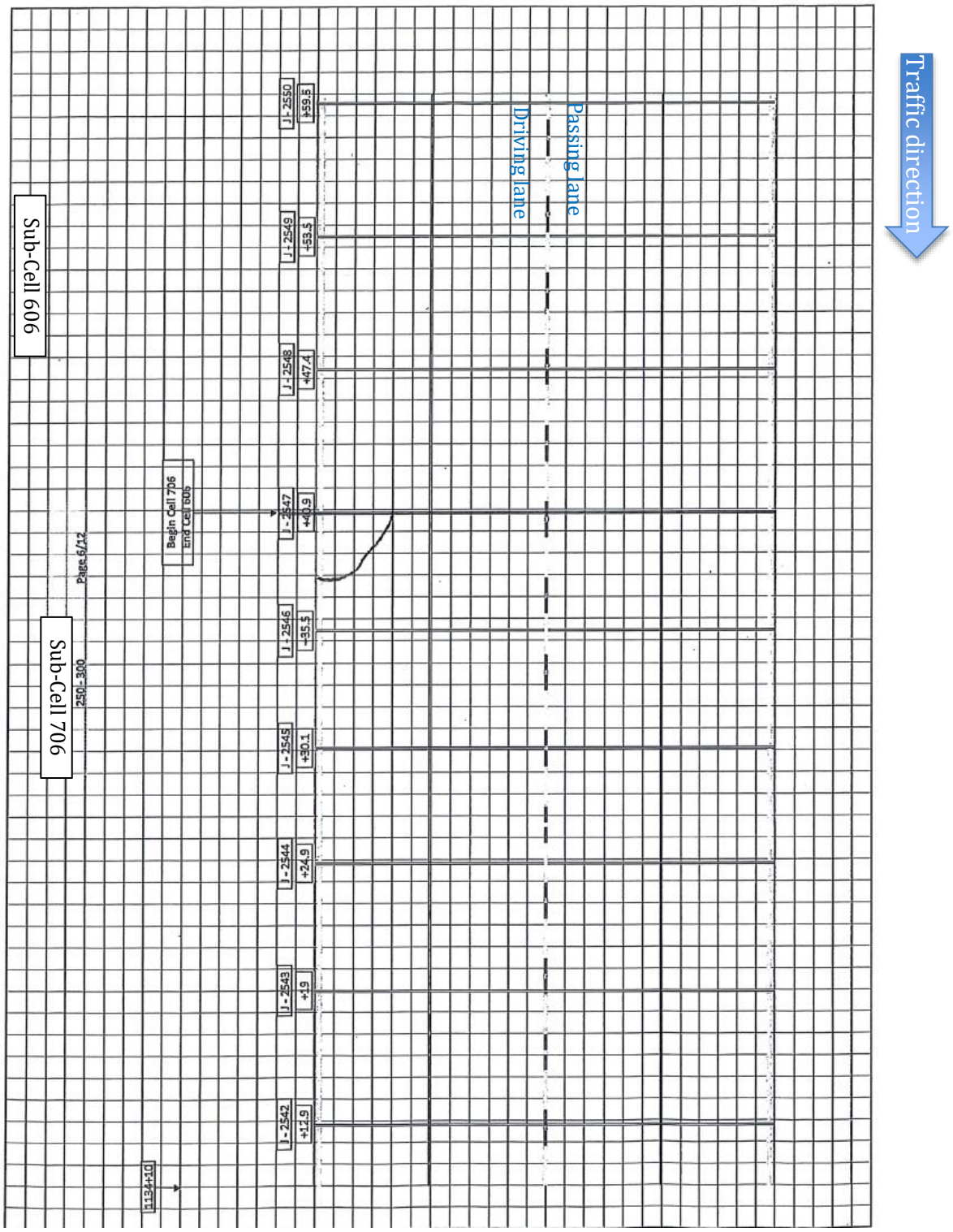

Cracks until October 2019; cracks colored in red were documented on October 25, 2019.

Figure A24: Distress map for Cells 606 through 706.

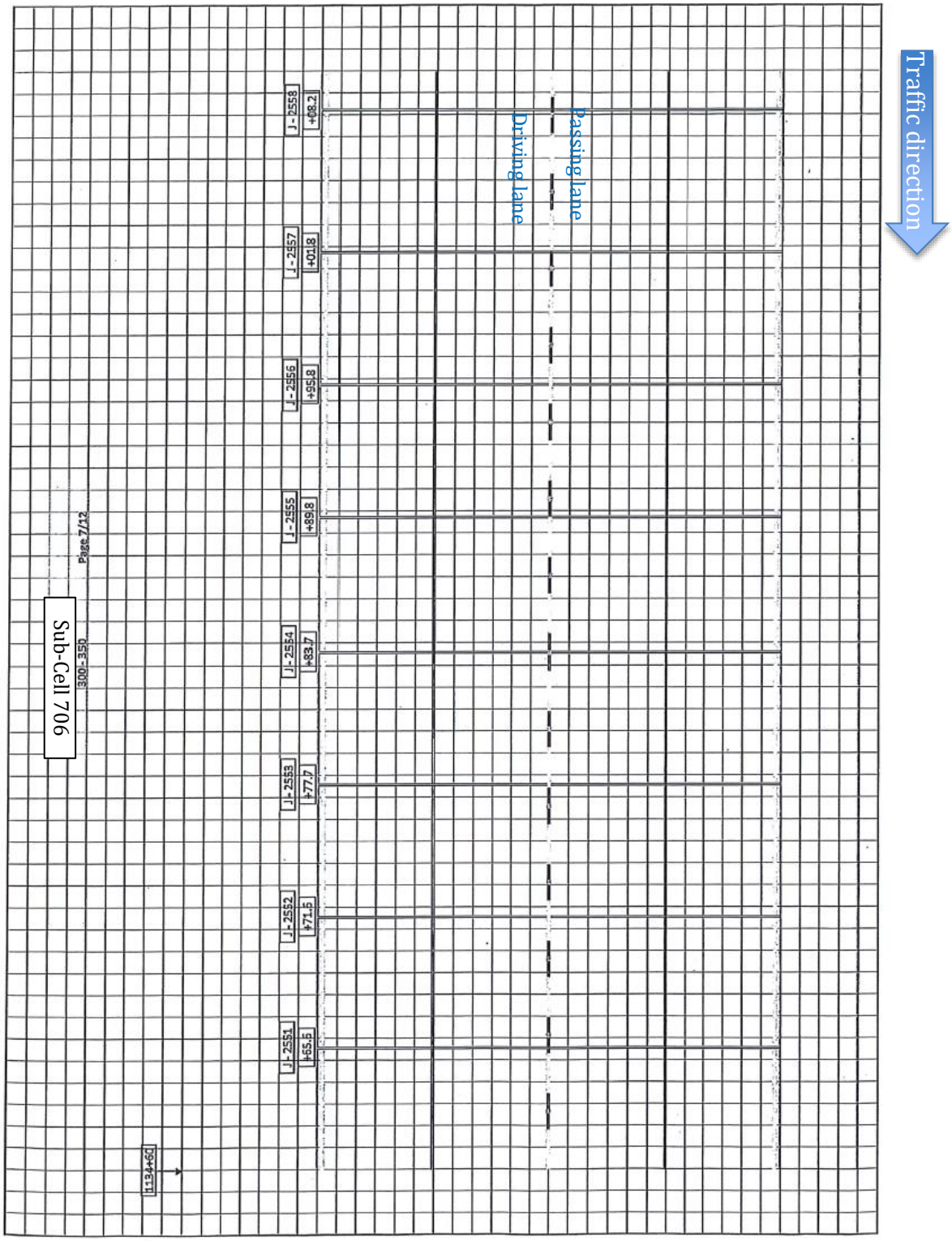

Cracks until October 2019; cracks colored in red were documented on October 25, 2019.

Figure A25: Distress map for Cells 706 .. contd.

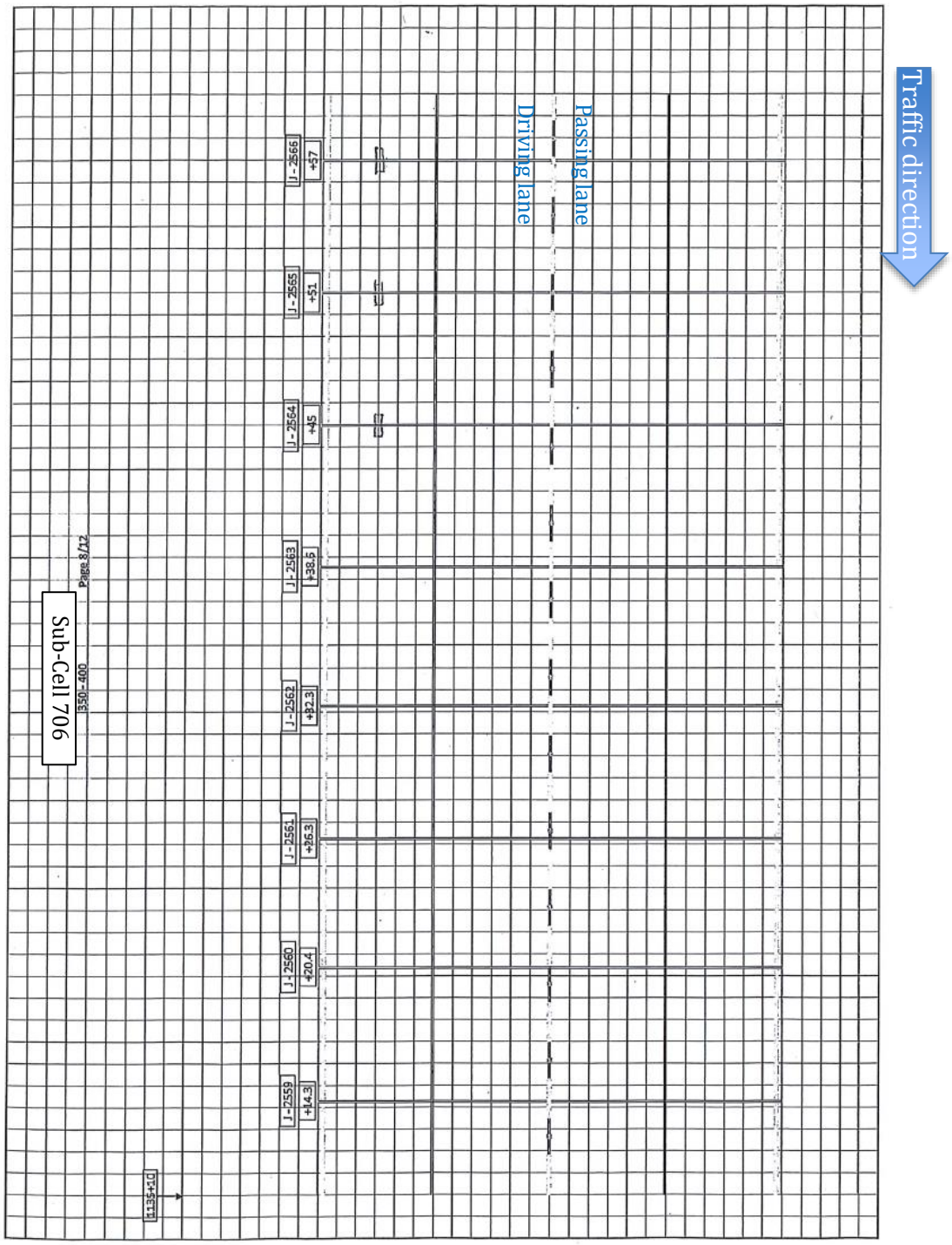

Cracks until October 2019; cracks colored in red were documented on October 25, 2019.

Figure A26: Distress map for Cell 706.. contd.

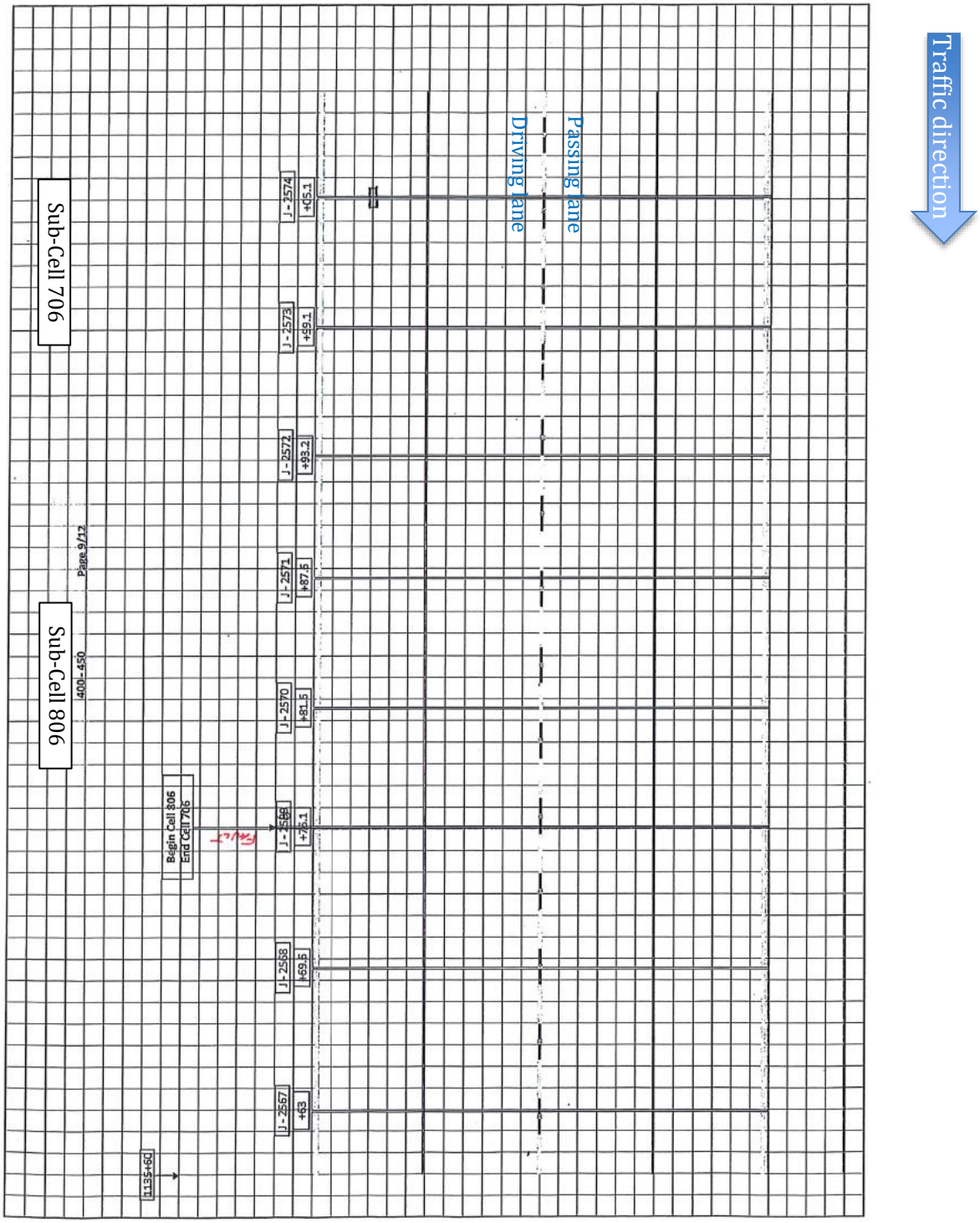

Cracks until October 2019; cracks colored in red were documented on October 25, 2019.

Figure A 27: Distress map for Cells 706 through 806.. contd.

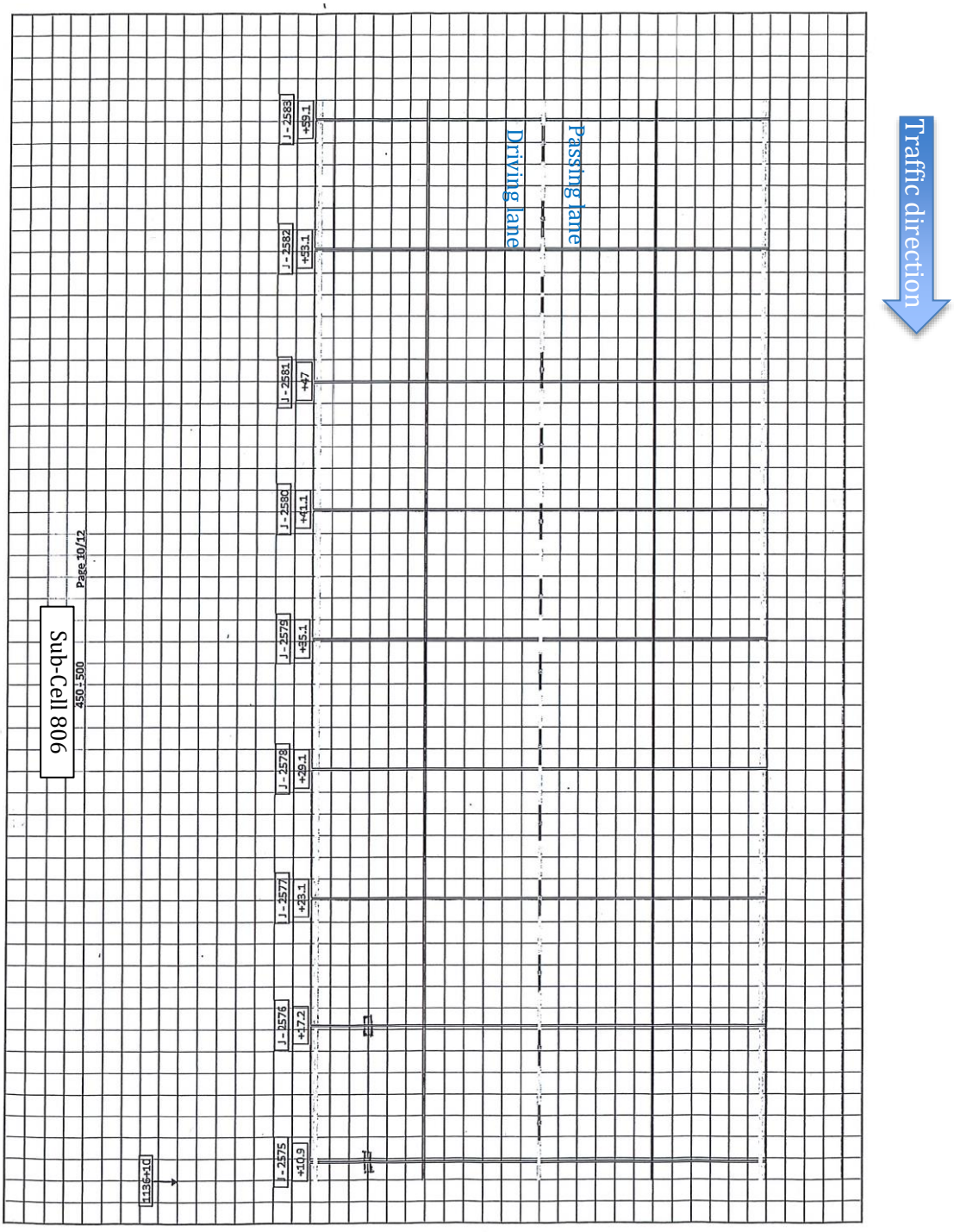

Cracks until October 2019; cracks colored in red were documented on October 25, 2019.

Figure A28: Distress map for Cell 806 .. contd.

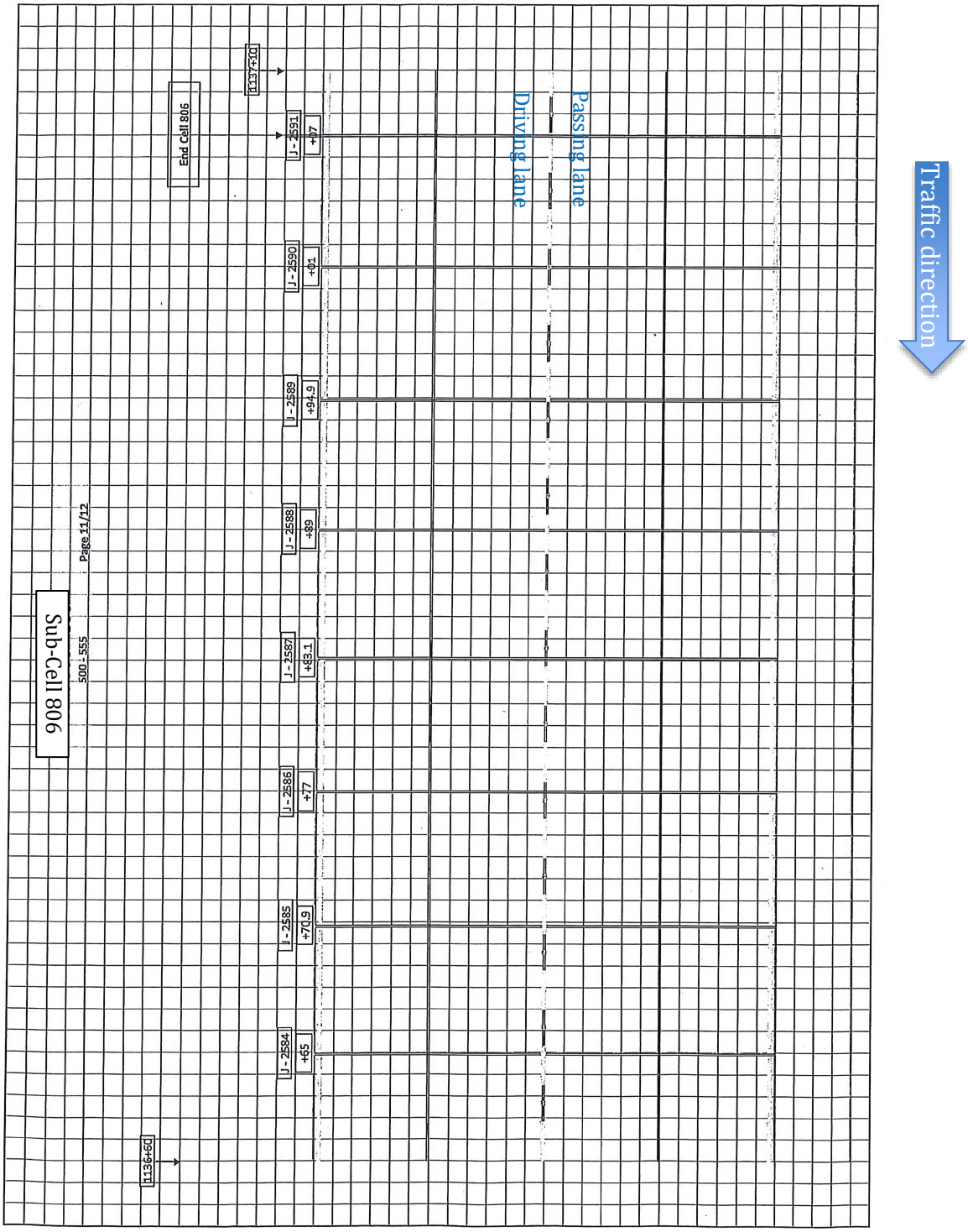

Cracks until October 2019; cracks colored in red were documented on October 25, 2019.

Figure A29: Distress map for Cell 806.. contd.

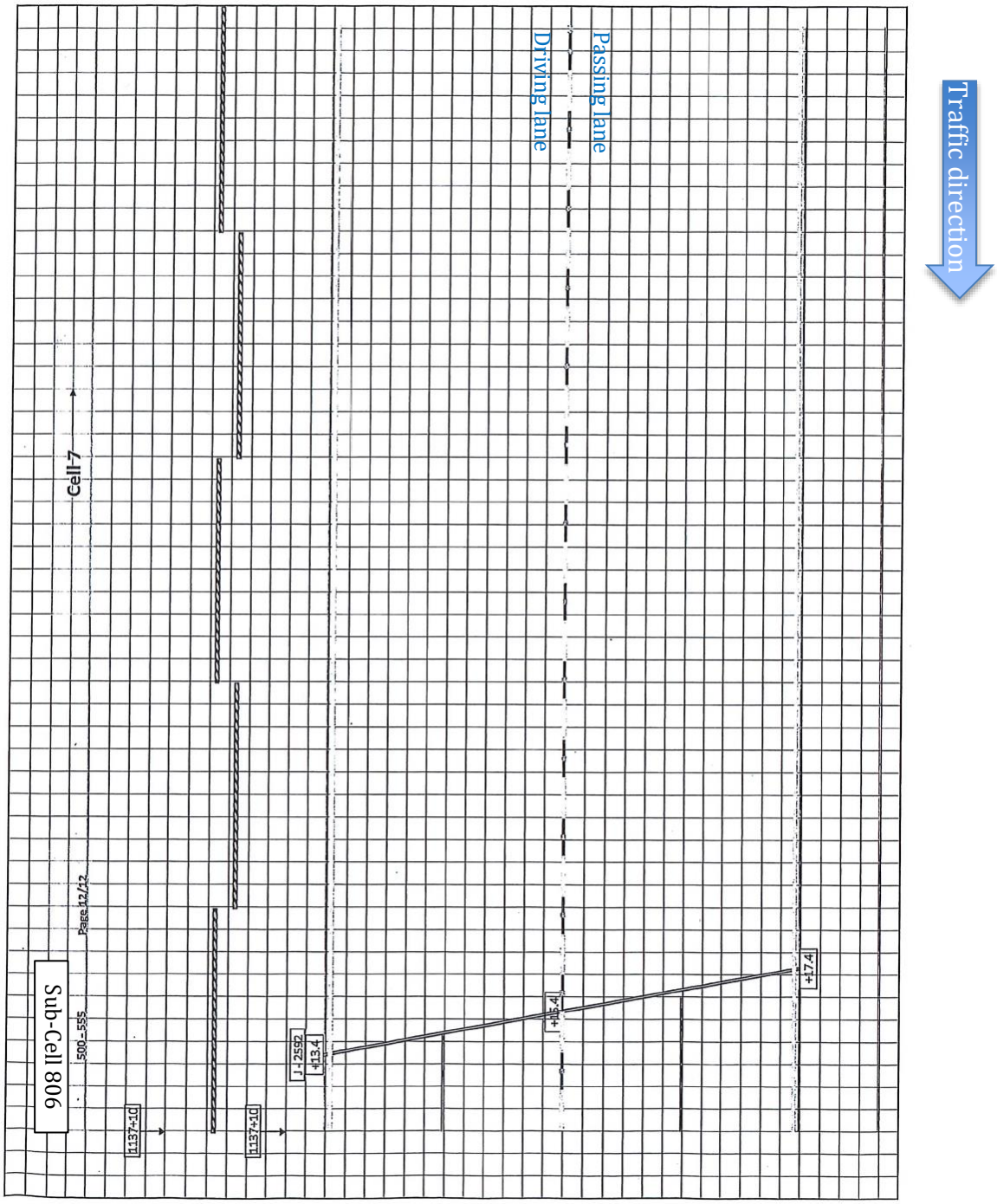

Cracks until October 2019; cracks colored in red were documented on October 25, 2019.

Figure A30: Distress map for Cells 806.. contd.

APPENDIX B

Joint Movement Data from Spring Loaded Potentiometer

Note: This Appendix presents the joint movement data recorded by the spring loaded potentiometers installed at different cells. Note that some of the data are appeared to be erroneous and not considered for any analysis.

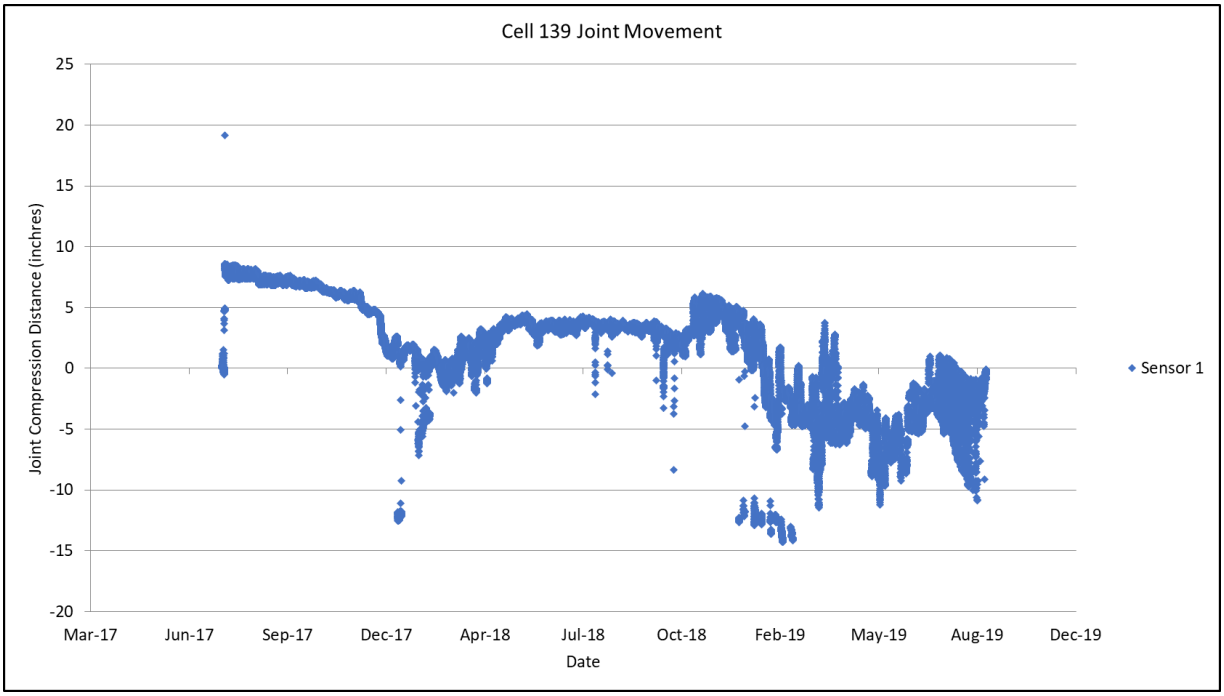

Figure B1. Joint movement data for Cell 139, Sensor 1.

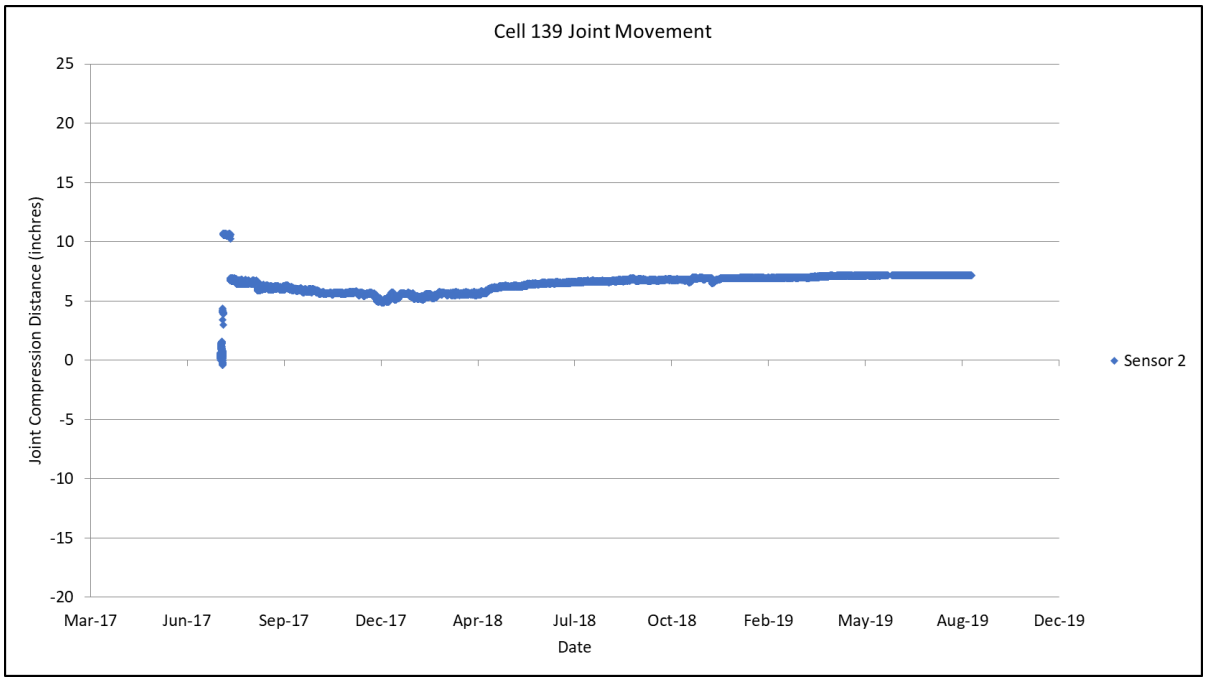

Figure B2. Joint movement data for Cell 139, Sensor 2.

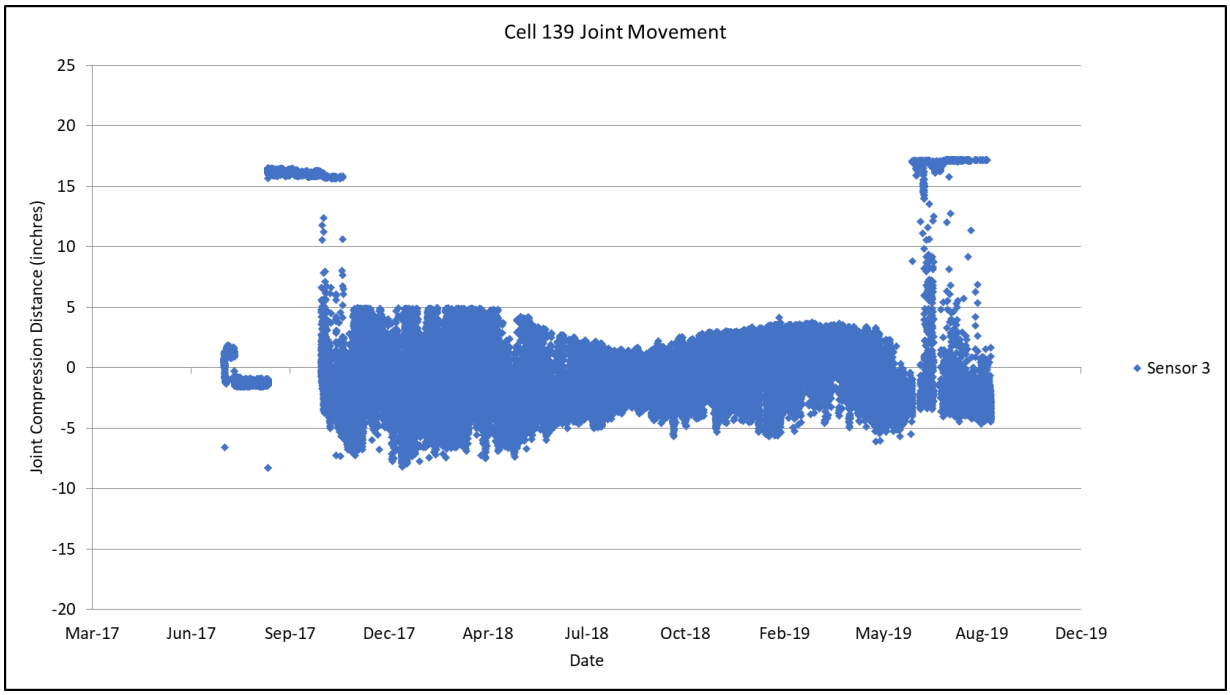

Figure B3. Joint movement data for Cell 139, Sensor 3 **(Bad sensor)**.

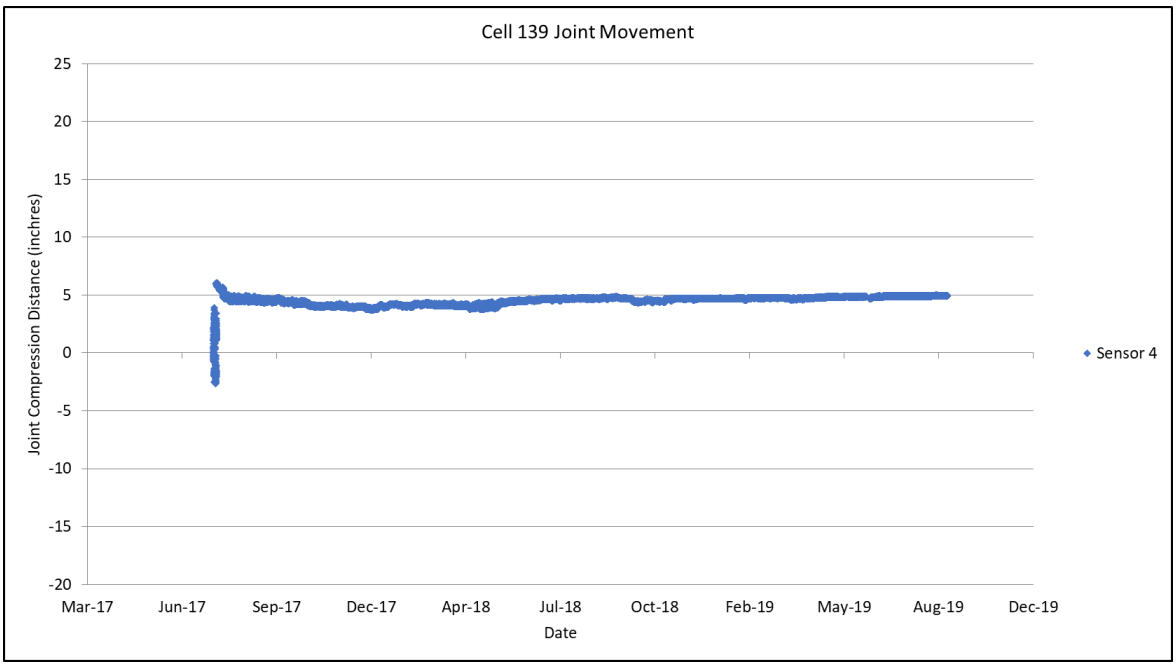

Figure B4. Joint movement data for Cell 139, Sensor 4.

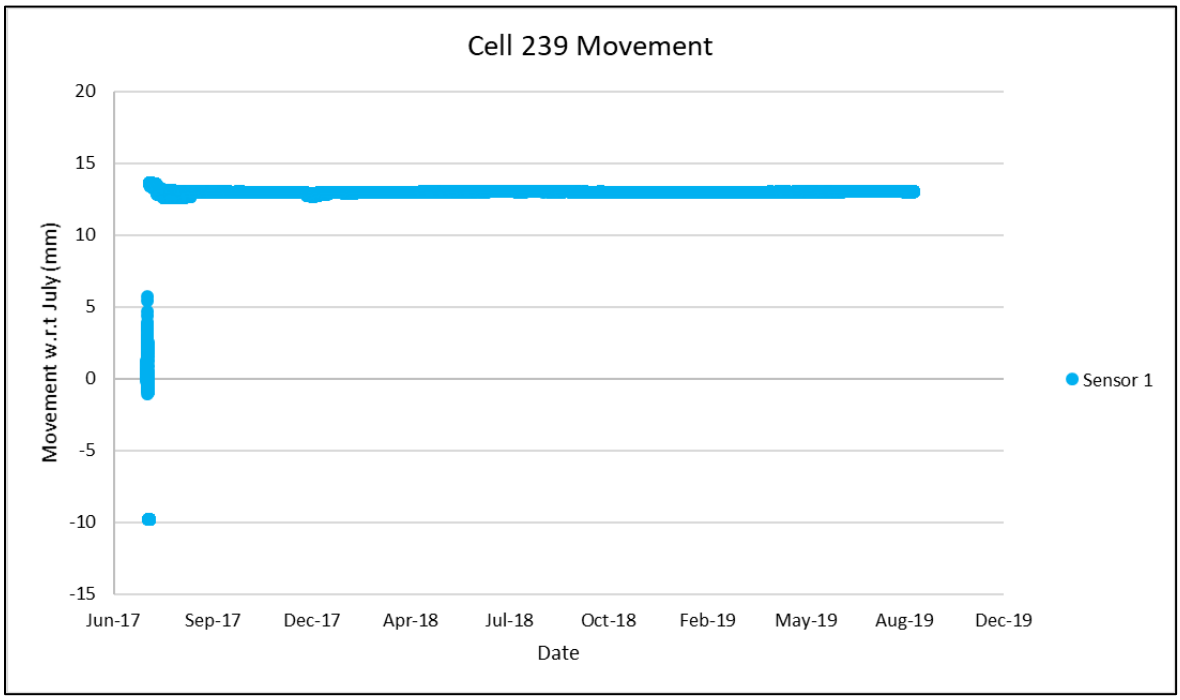

Figure B5. Joint movement data for Cell 239, Sensor 1.

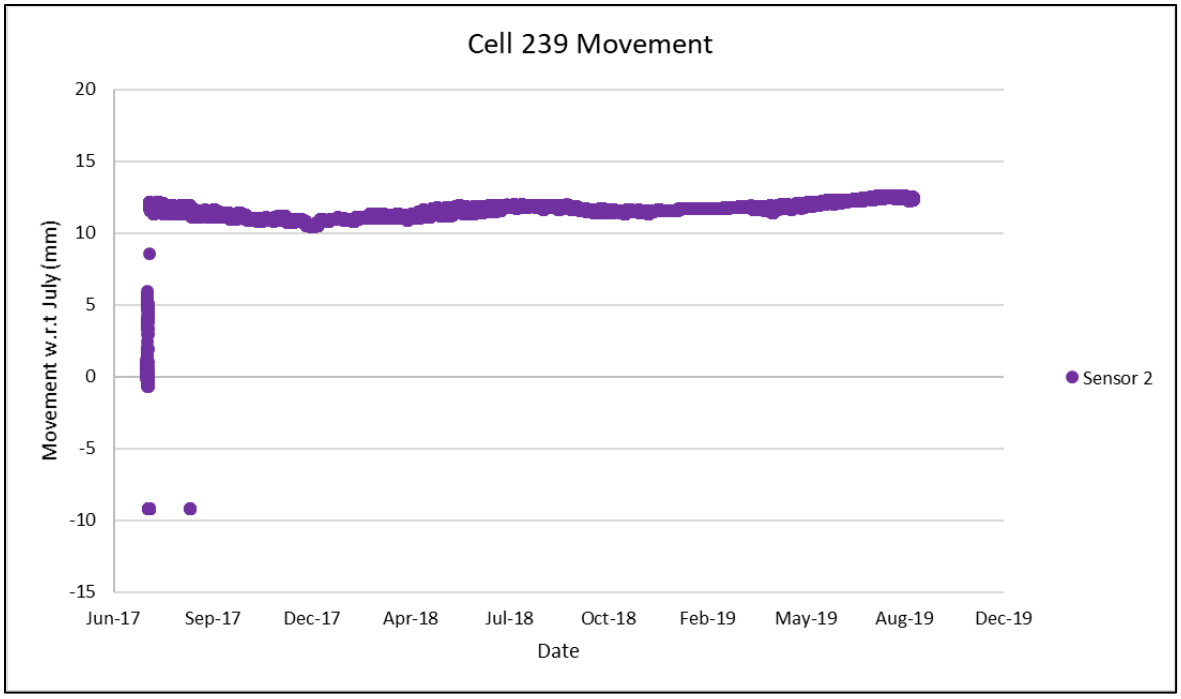

Figure B6. Joint movement data for Cell 239, Sensor 2.

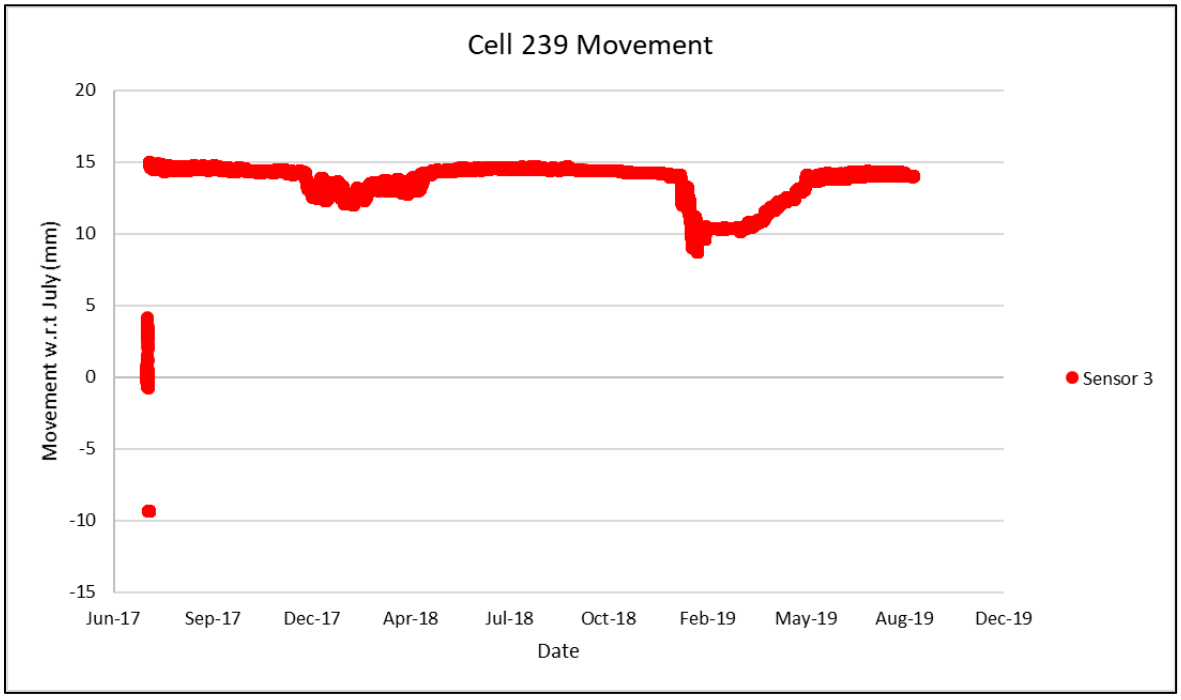

Figure B7. Joint movement data for Cell 239, Sensor 3.

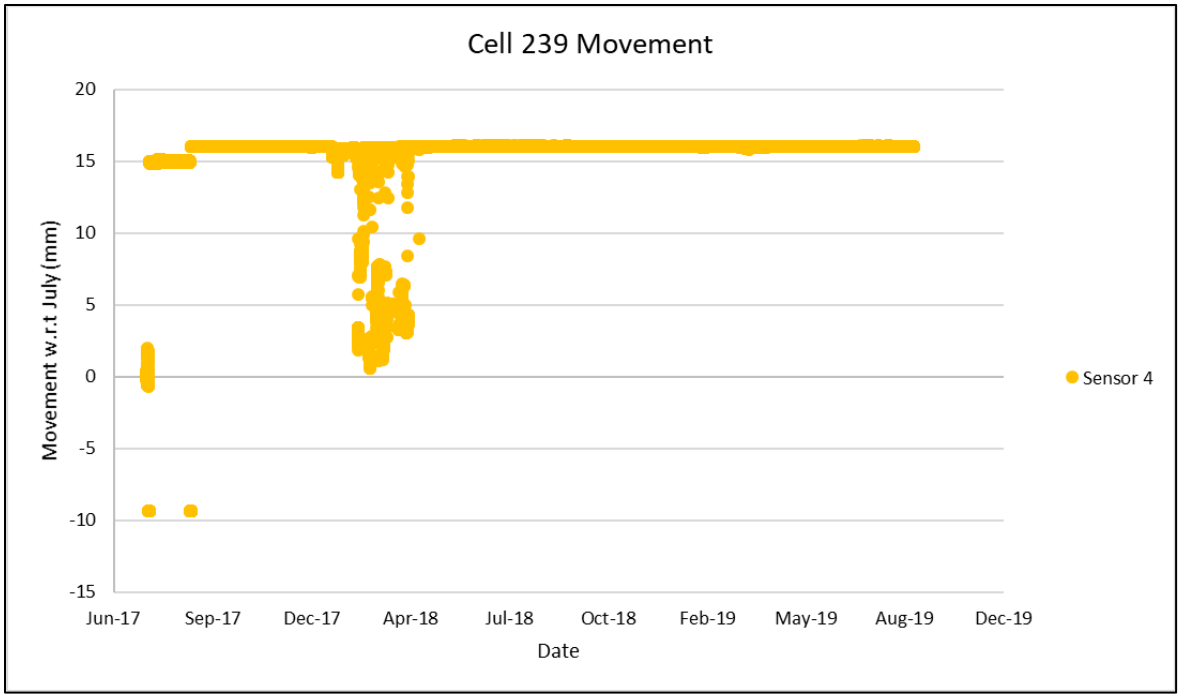

Figure B8. Joint movement data for Cell 239, Sensor 4.

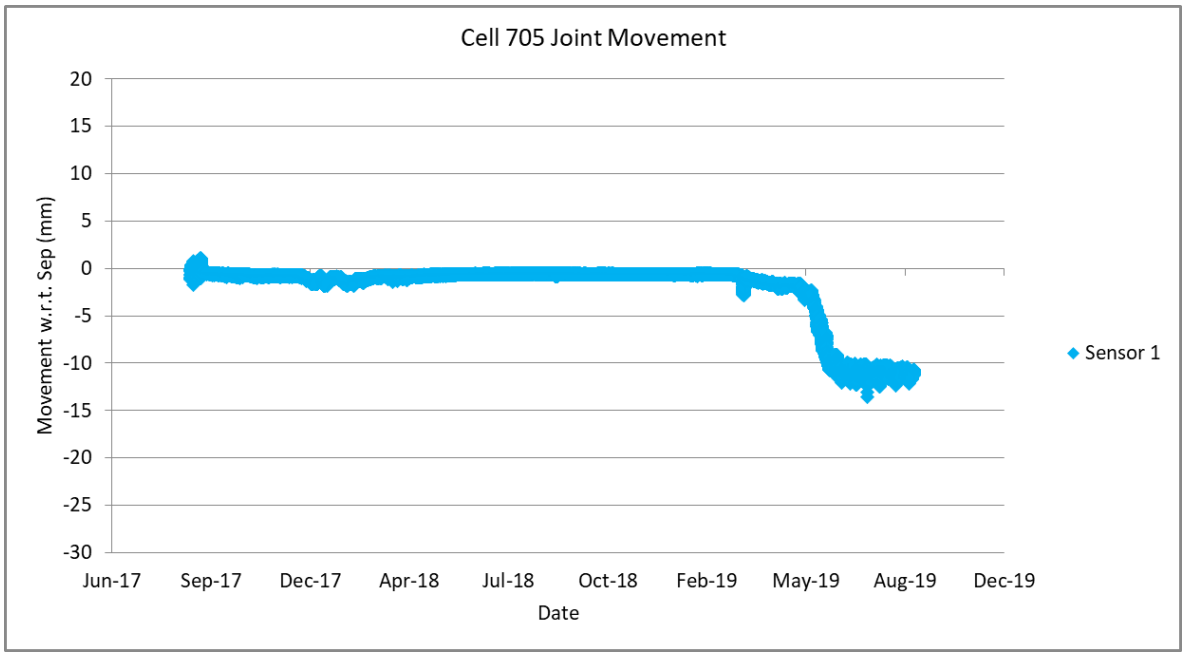

Figure B9. Joint movement data for Cell 705, Sensor 1.

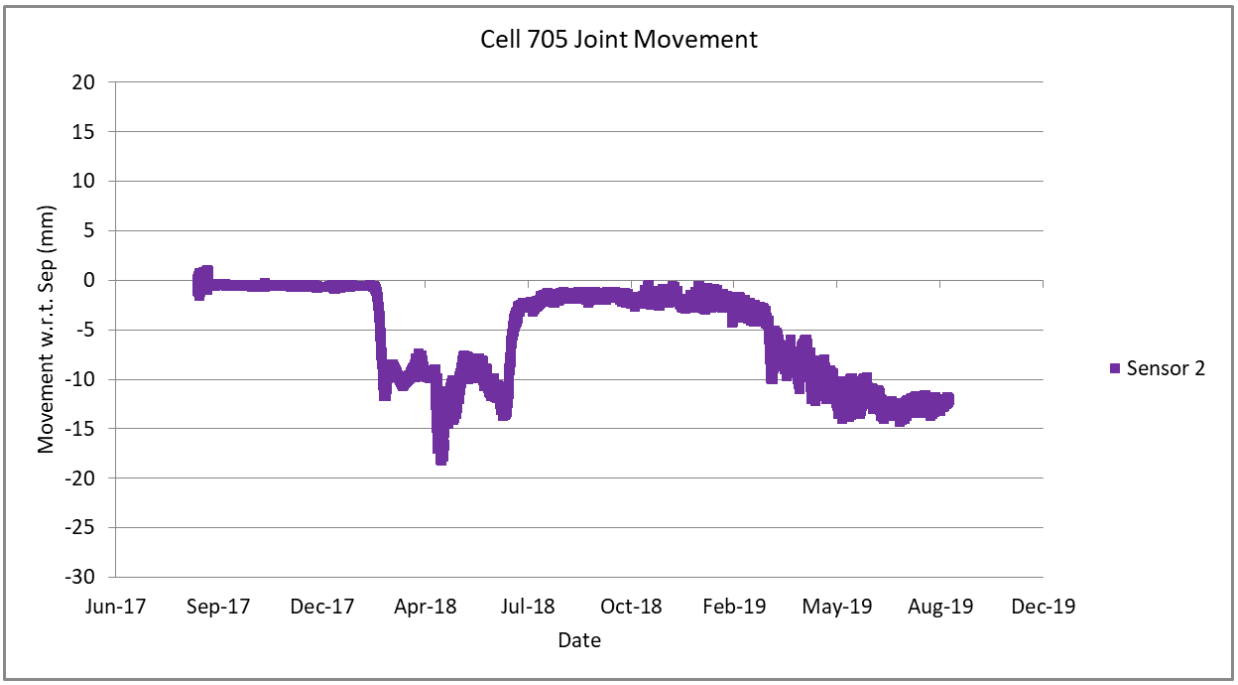

Figure B10. Joint movement data for Cell 705, Sensor 2.

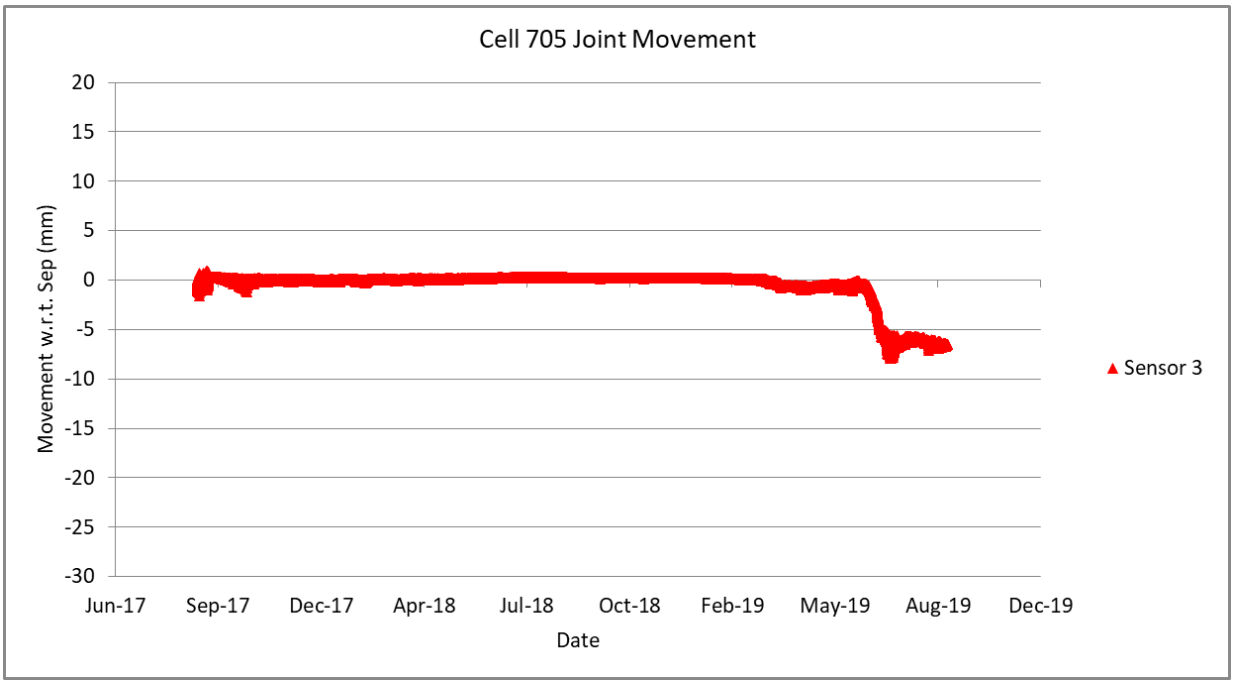

Figure B11. Joint movement data for Cell 705, Sensor 3.

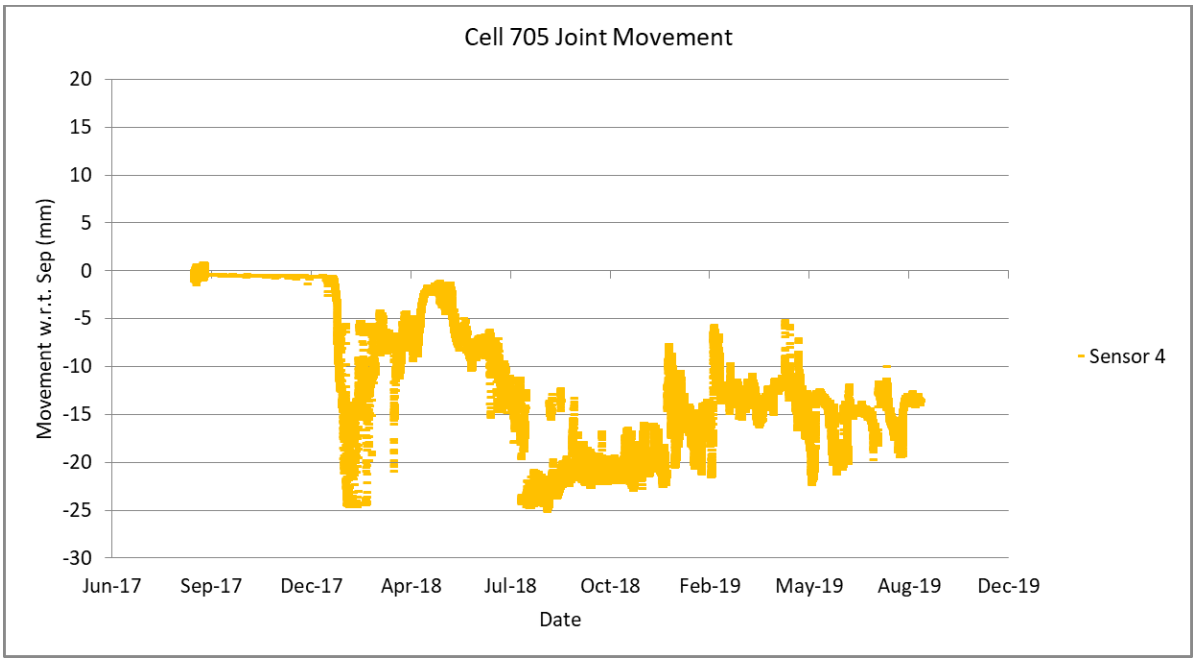

Figure B12. Joint movement data for Cell 705, Sensor 4.

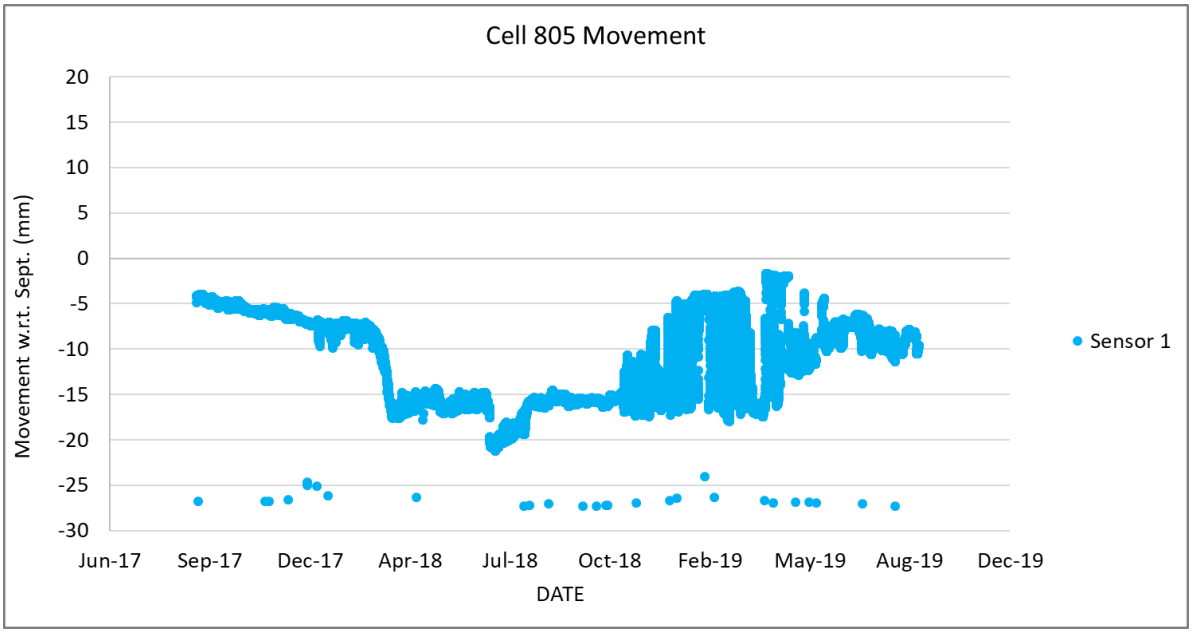

Figure B13. Joint movement data for Cell 805, Sensor 1.

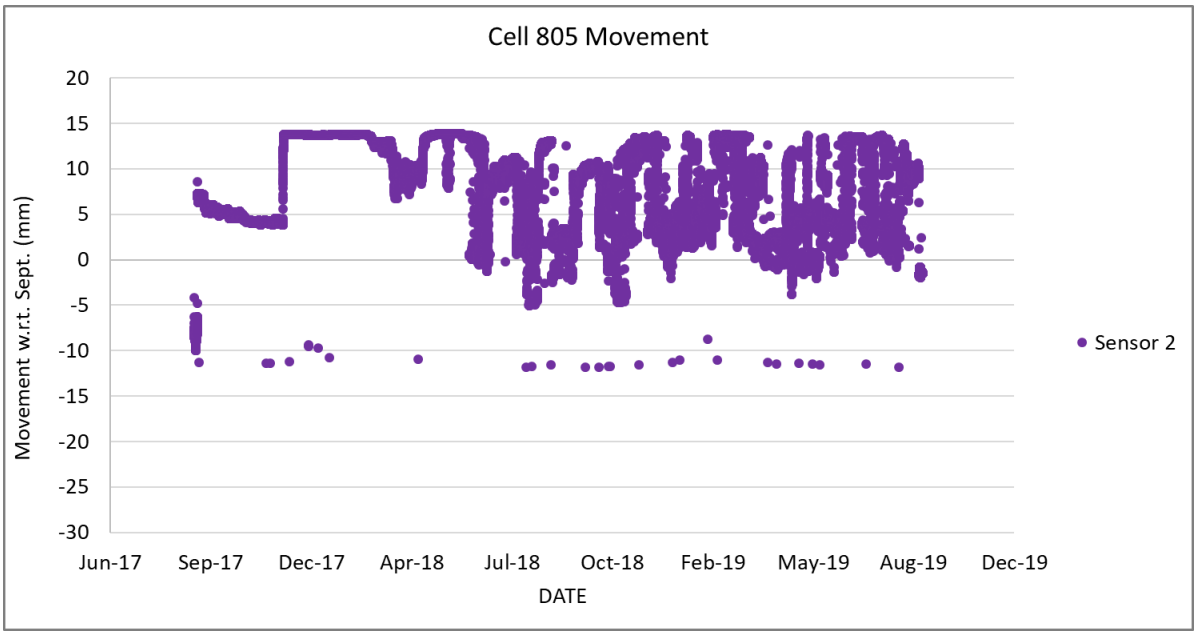

Figure B14. Joint movement data for Cell 805, Sensor 2.

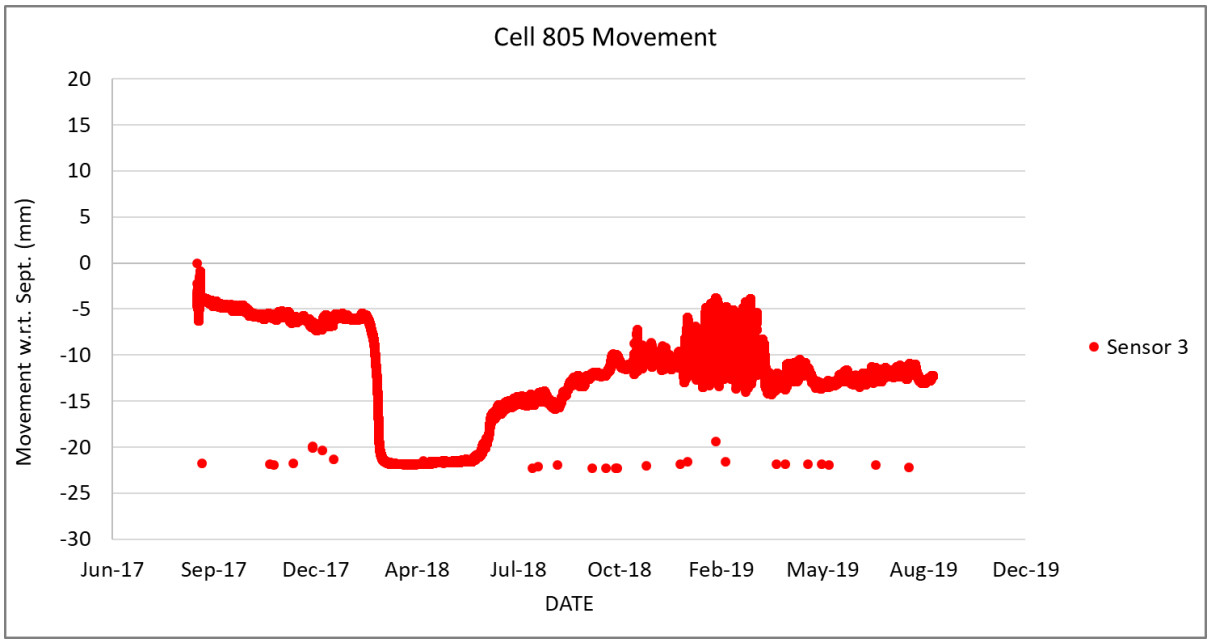

Figure B15. Joint movement data for Cell 805, Sensor 3.

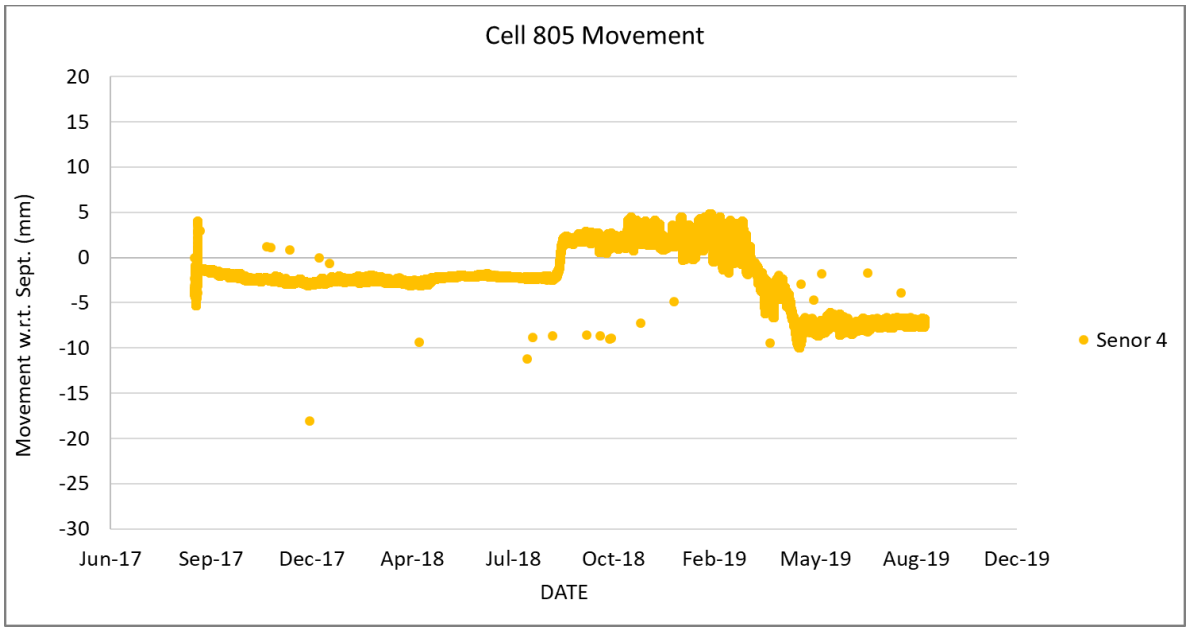

Figure B16. Joint movement data for Cell 805, Sensor 4.

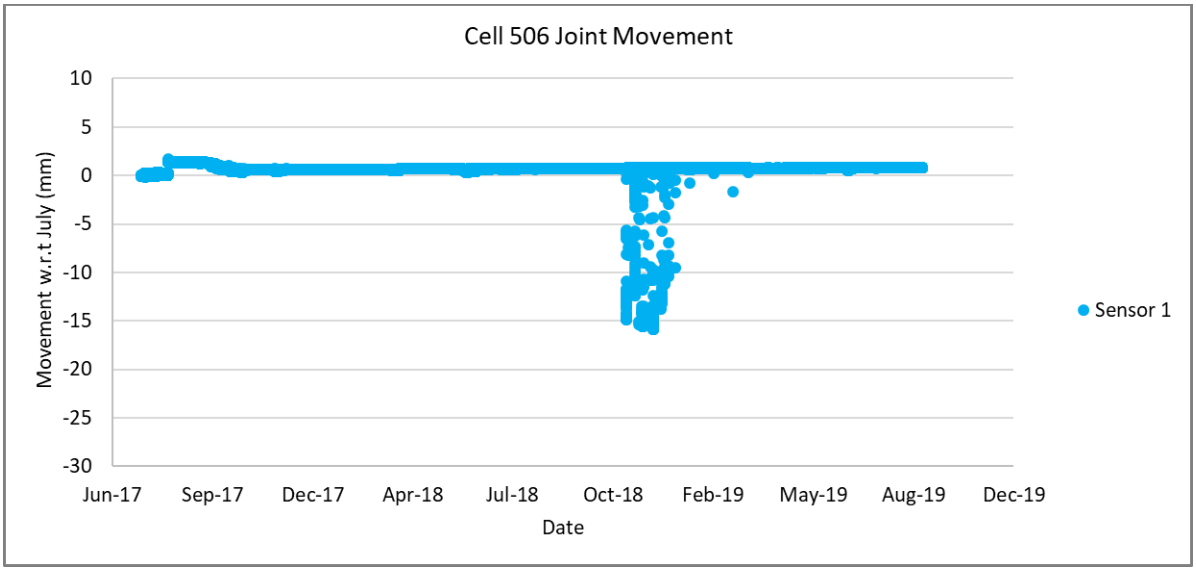

Figure B17. Joint movement data for Cell 506, Sensor 1.

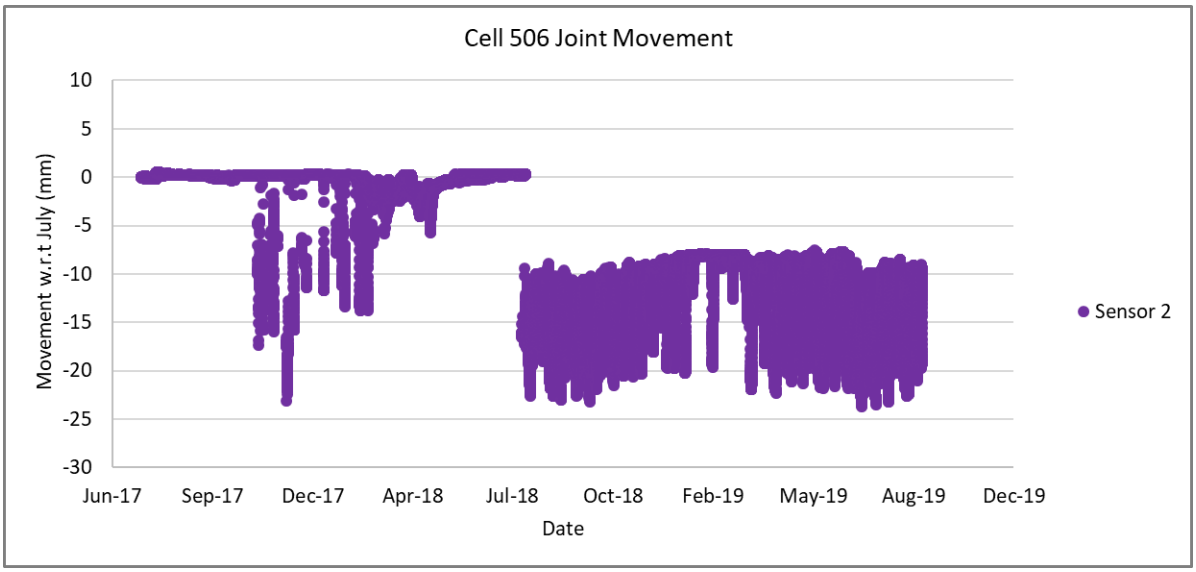

Figure B18. Joint movement data for Cell 506, Sensor 2.

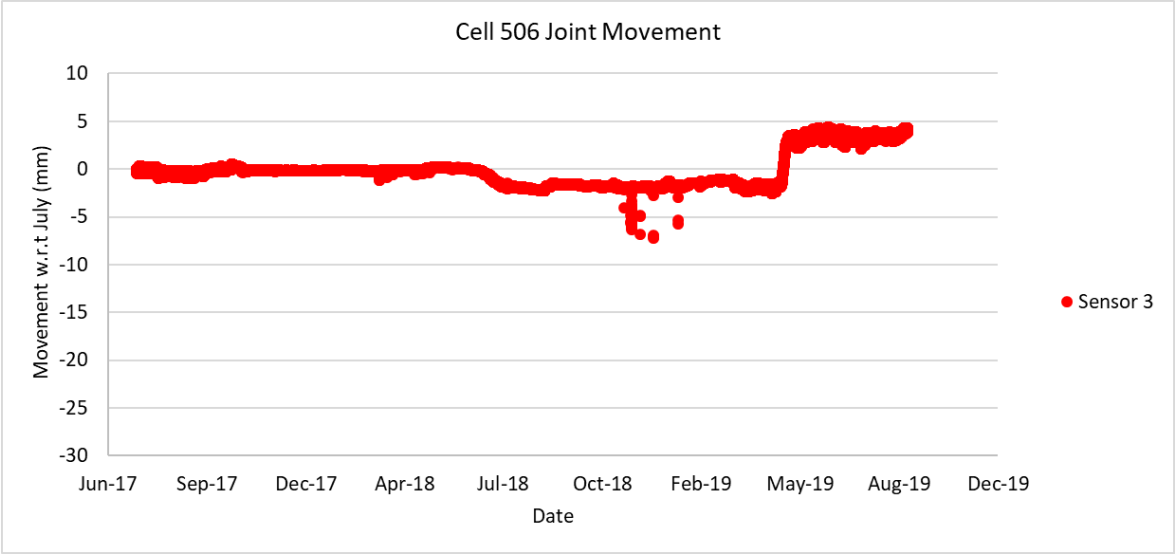

Figure B19. Joint movement data for Cell 506, Sensor 3.

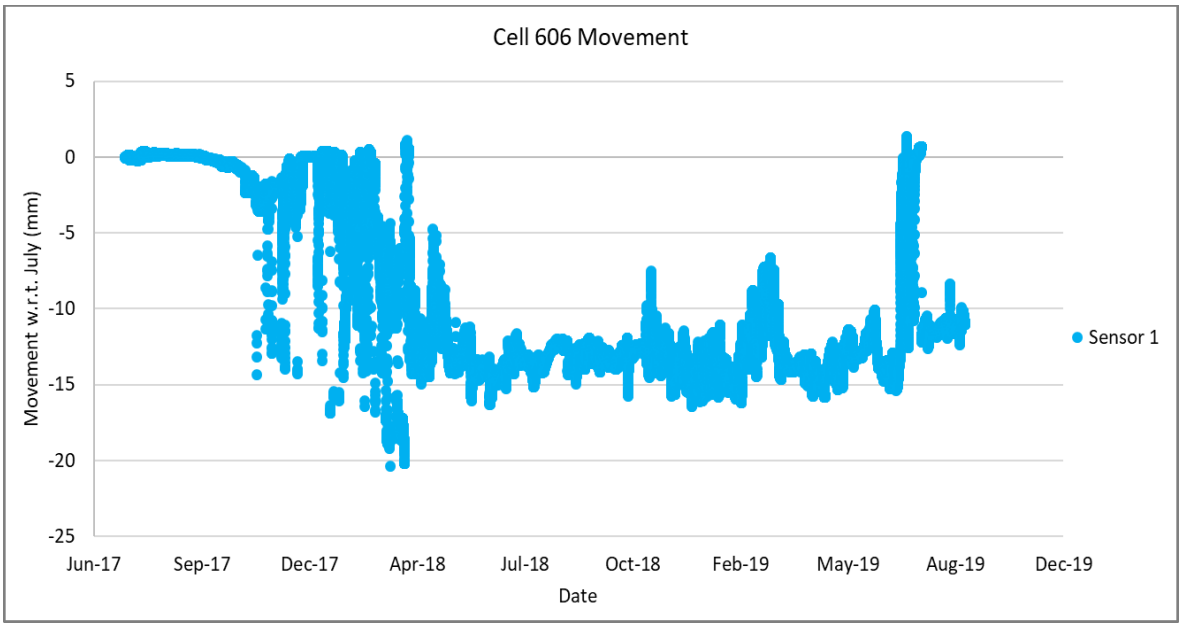

Figure B20. Joint movement data for Cell 606, Sensor 1.

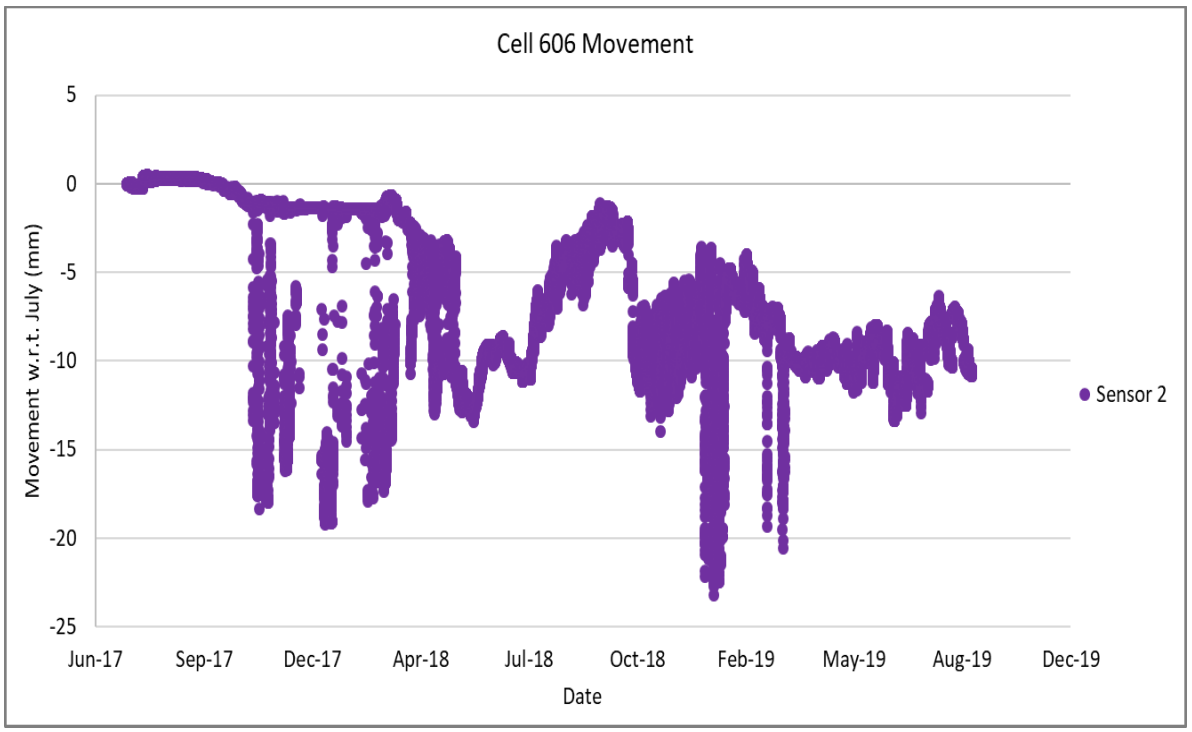

Figure B21. Joint movement data for Cell 606, Sensor 2.

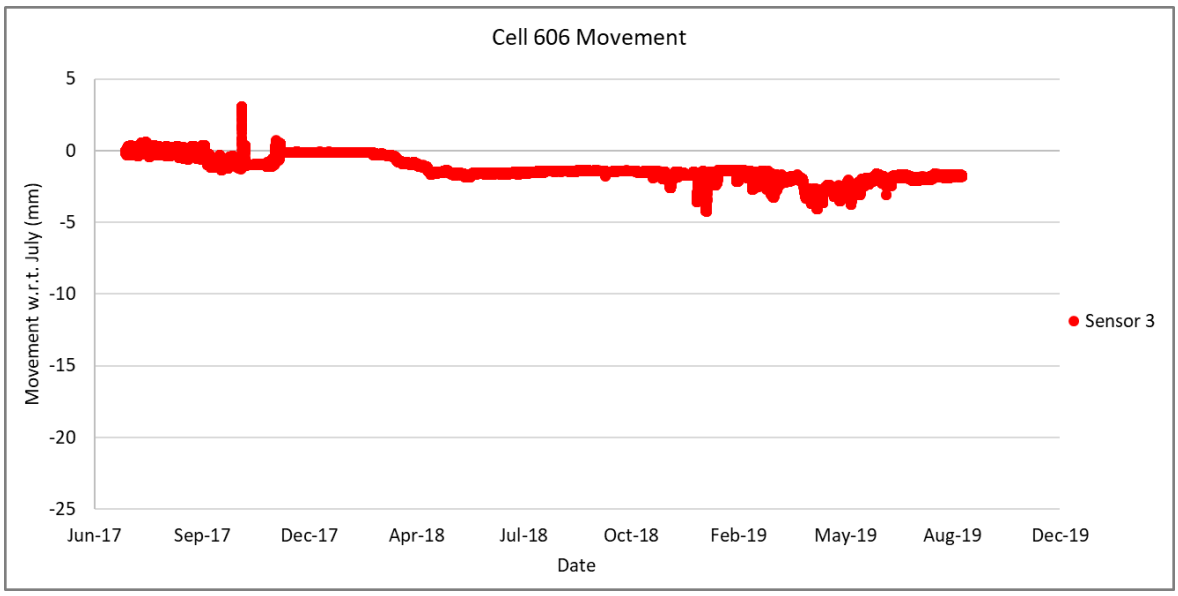

Figure B22. Joint movement data for Cell 606, Sensor 3.

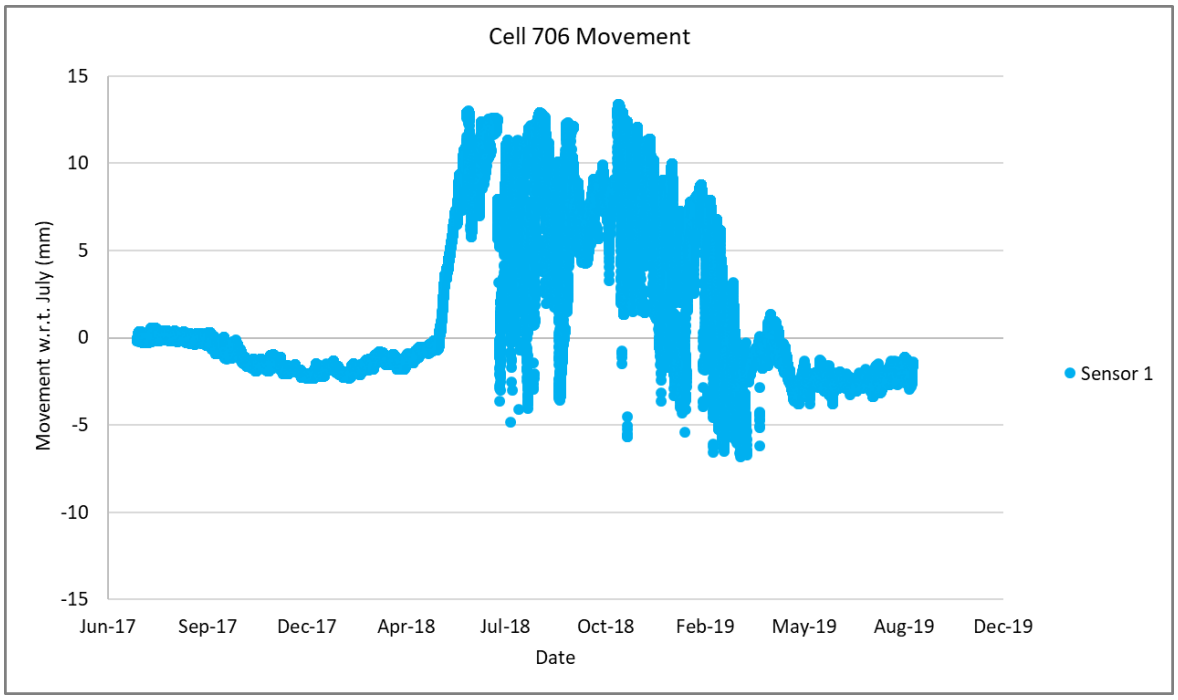

Figure B23. Joint movement data for Cell 706, Sensor 1.

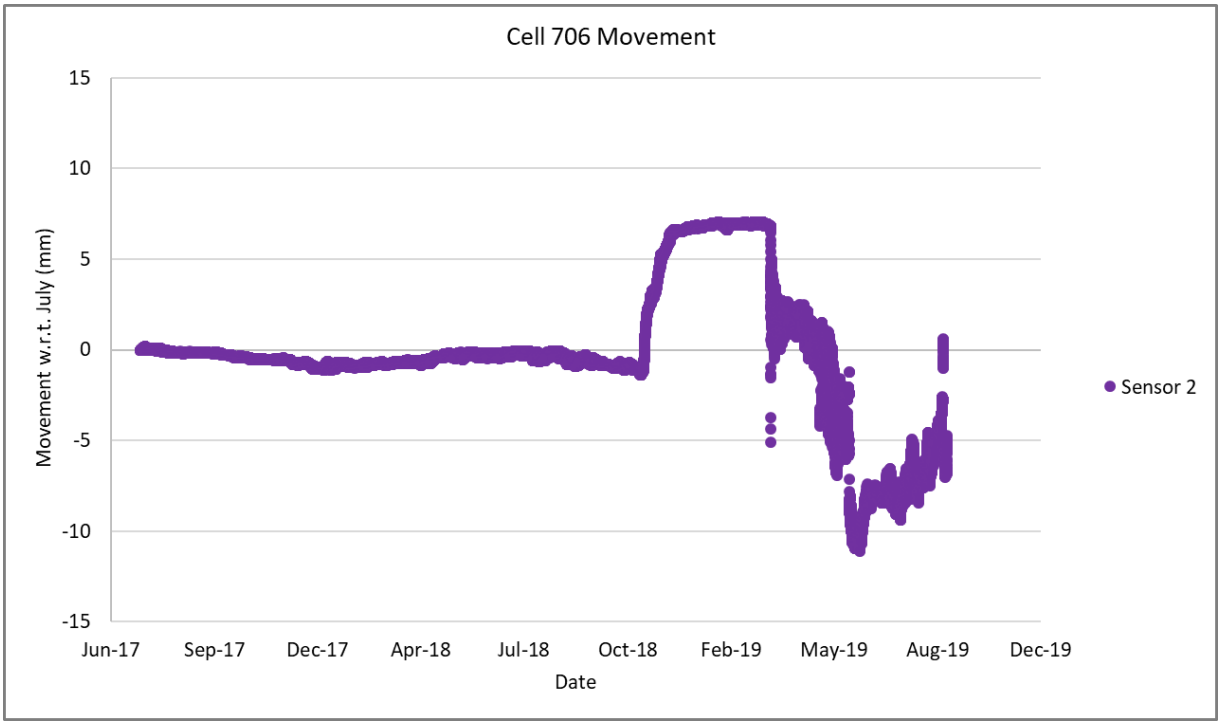

Figure B24. Joint movement data for Cell 706, Sensor 2.

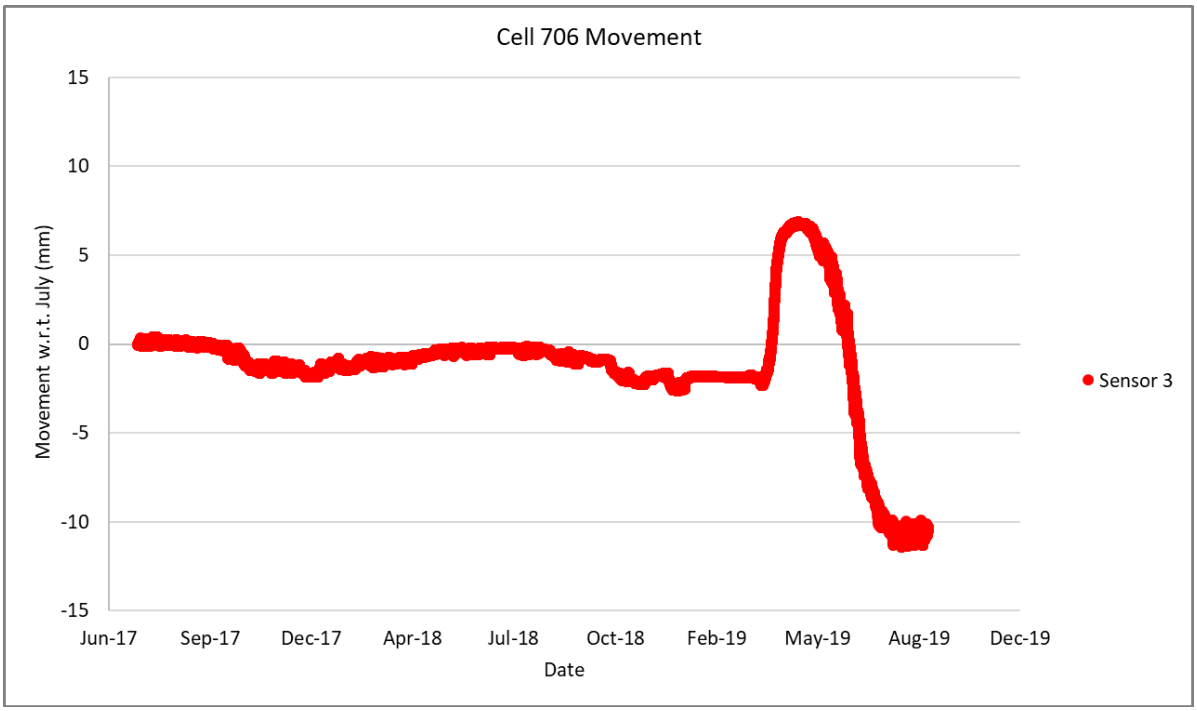

Figure B25. Joint movement data for Cell 706, Sensor 3.

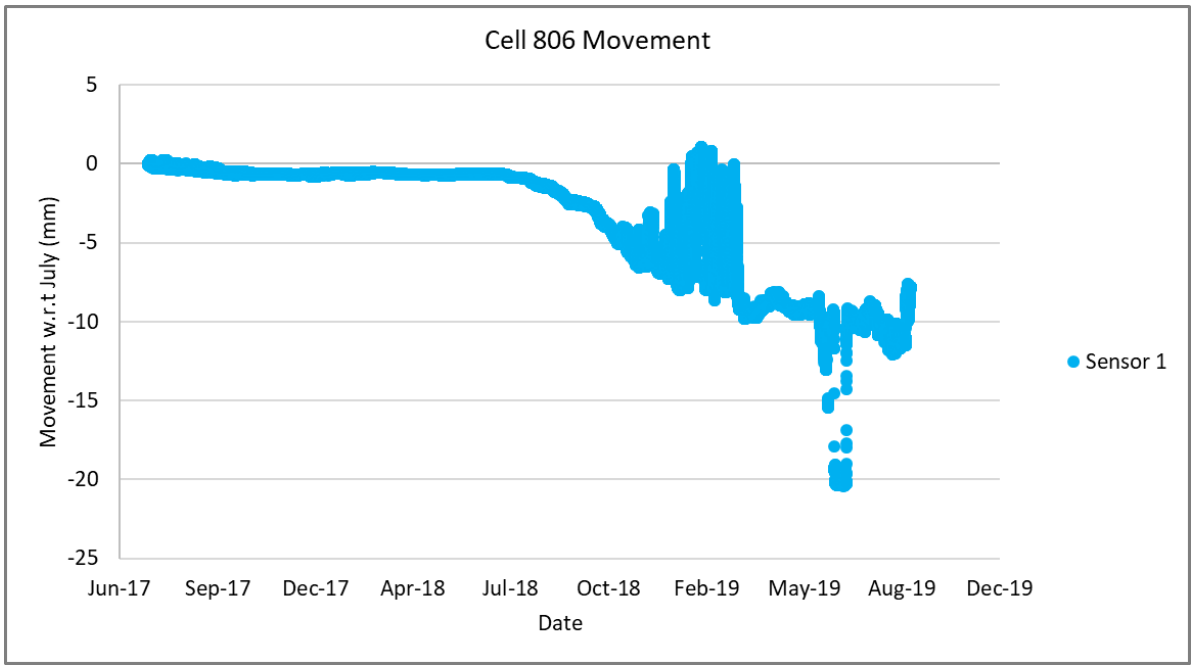

Figure B26. Joint movement data for Cell 806, Sensor 1.

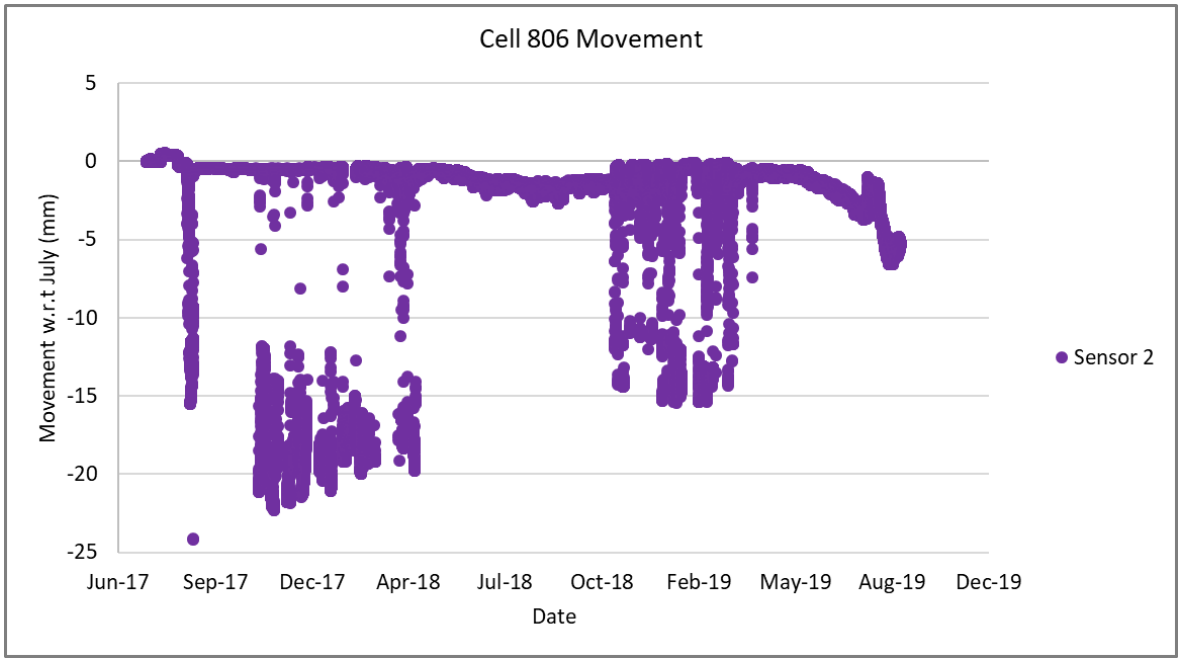

Figure B27. Joint movement data for Cell 806, Sensor 2 **(Bad sensor)**.

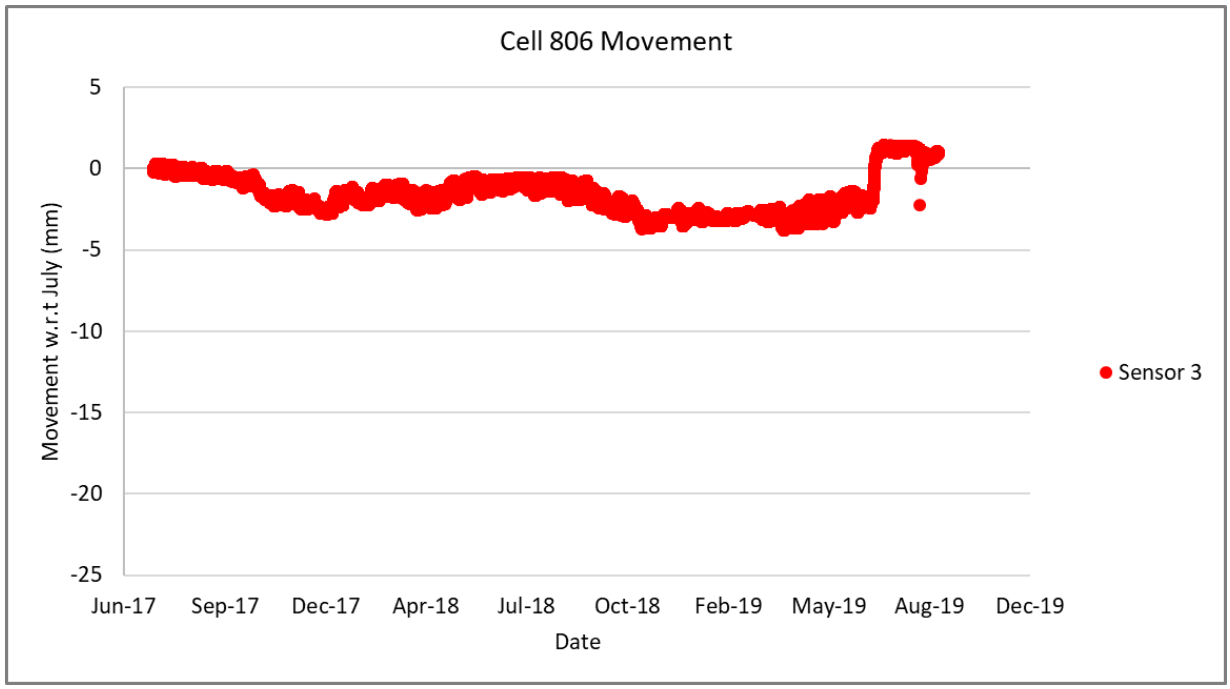

Figure B28. Joint movement data for Cell 806, Sensor 3.